

**INSTITUTE OF NATURAL AND APPLIED SCIENCES
UNIVERSITY OF ÇUKUROVA**

PhD. THESIS

Bayram TALİ

**TEST RESULTS OF THE HAMAMATSU R7378A PHOTOTUBES, ANALYSIS
OF THE TEST BEAM 08 AND PRELIMINARY AFTER-INSTALLATION DATA
OF THE CMS-CASTOR CALORIMETER**

DEPARTMENT OF PHYSICS

ADANA, 2009

**INSTITUTE OF NATURAL AND APPLIED SCIENCES
UNIVERSITY OF ÇUKUROVA**

**TEST RESULTS OF THE HAMAMATSU R7378A PHOTOTUBES, ANALYSIS
OF THE TEST BEAM 08 AND PRELIMINARY AFTER-INSTALLATION DATA
OF THE CMS-CASTOR CALORIMETER**

By Bayram TALİ

**A THESIS OF DOCTOR OF PHILOSOPHY
DEPARTMENT OF PHYSICS**

We certify that the thesis titled above was reviewed and approved for the award of degree of the Doctor of Philosophy by the board of jury on/...../ 2009

Signature:..... Signature:..... Signature:.....
Prof. Dr. Gülsen ÖNENGÜT Prof. Dr. Aysel KAYIŞ TOPAKSU Assoc. Prof. Dr. Ali HAVARE
SUPERVISOR MEMBER MEMBER

Signature:..... Signature:.....
Assoc. Prof. Dr. İsa DUMANOĞLU Assist. Prof. Dr. Salim ÇERÇİ
MEMBER MEMBER

This PhD Thesis is performed in Department of Physics of Institute of Natural and Applied Sciences of Cukurova University.

Registration Number:

Prof. Dr. İlhami YEĞİNGİL
Director
The Institute of Natural and Applied Sciences
Signature and Seal

This Study was supported by Çukurova University Scientific Research Fund.

Project Number: FEF2009D12

Not: The usage of the presented specific declarations, tables, figures and photographs either in this thesis or in any other reference without citation is subject to “The Law of Arts and Intellectual Products” numbered 5846 of Turkish Republic.

To my family and wife.

ABSTRACT

PhD THESIS

TEST RESULTS OF THE HAMAMATSU R7378A PHOTOTUBES, ANALYSIS OF THE TEST BEAM 08 AND PRELIMINARY AFTER- INSTALLATION DATA OF THE CMS-CASTOR CALORIMETER

Bayram TALİ

DEPARTMENT OF PHYSICS
INSTITUTE OF NATURAL AND APPLIED SCIENCES
UNIVERSITY OF ÇUKUROVA

Supervisor: Prof. Dr. Gülsen ÖNENGÜT
Year : 2009, **Pages:** 126
Jury : Prof .Dr. Gülsen ÖNENGÜT
Prof .Dr. Aysel KAYIŞ TOPAKSU
Assoc. Prof. Dr. Ali HAVARE
Assoc. Prof. Dr. İsa DUMANOĞLU
Assist. Prof. Dr. Salim ÇERÇİ

This thesis consists of four chapters: The first chapter is the introduction. In this chapter, LHC machine and CMS detector which were constructed with the purpose of proving SM and its predictions and discovering new physics beyond SM were explained shortly. CASTOR, which is a Cherenkov sampling calorimeter is positioned in the CMS Experiment in the very forward region as a sub-detector and is 14.38 m far from the interaction point. The design of the CASTOR calorimeter, the main components of the detector and physics with CASTOR were also explained in this chapter. The second chapter is about the measurements of the characteristics of the PMTs which are a part of CASTOR. In this chapter, general description of PMTs, the design of the PMTs and several characteristics of the PMTs were described. Furthermore, Çukurova University test station and setups in this test station were presented. At the end of the second chapter the measurements of Hamamatsu R7378A type PMTs performed in Çukurova University test station were explained and the results of the tests were analyzed and discussed. The third chapter is about the CASTOR test beam 2008 (TB08). Generally, CERN/SPS/H2 test beam area, several detectors in this area, results of the previous test beams performed for CASTOR were explained. Finally the analysis of the TB08 data which includes the response of the detector (the energy resolution, the energy linearity, the longitudinal and transversal development of the showers) for different particles such as pions, electrons, muons at different energies was given and discussed. The fourth chapter is about the CASTOR installation in the CMS. After installation, the magnetic field on the CASTOR area, very preliminary results of the gain of the PMTs, the movement of CASTOR, because of the effect of the magnetic field were given and discussed.

Key Words: LHC, CMS - CASTOR, ÇU test station - PMT - Gain, TB08, Installation

ÖZ
DOKTORA TEZİ

**HAMAMATSU R7378A FOTOTÜPLERİNİN TEST SONUÇLARI, CMS-
CASTOR KALORİMETRESİNİN 08 TEST HUZMESİNİN VE
KURULUMUNUNDAN SONRAKİ İLK VERİLERİNİN ANALİZLERİ**

Bayram TALİ

**ÇUKUROVA ÜNİVERSİTESİ
FEN BİLİMLERİ ENSTİTÜSÜ
FİZİK ANABİLİM DALI**

Danışman: Prof. Dr. Gülsen ÖNENGÜT
Yıl : 2009, **Sayfa:** 126
Jüri : Prof .Dr. Gülsen ÖNENGÜT
Prof .Dr. Aysel KAYIŞ TOPAKSU
Doç. Dr. Ali HAVARE
Doç. Dr. İsa DUMANOĞLU
Yard. Doç. Dr. Salim ÇERÇİ

Bu tez dört bölümden oluşmaktadır. Birinci bölüm giriştir. Bu bölümde kısaca SM ve onun öngörülerini kanıtlamak ve SM ötesi fiziği keşfetmek amacıyla kurulan LHC makinası ve CMS dedektörü anlatıldı. CMS dedektörünün ileri bölgesinde etkileşim noktasının 14.38 m uzağında bulunan ve bir Cherenkov örnekleme kalorimetresi olan CASTOR kalorimetresinin dizaynından, kendisini oluşturan bölümlerden ve CASTOR kalorimetresi ile çalışılacak fizik konularından bahsedildi. İkinci bölüm CASTOR'un parçalarından biri olan PMT'lerin karakteristik özelliklerinin ölçümüdür. Bu bölümde PMT'lerin genel tanıtımı yapıldı. Bunların dizaynı ve bazı karakteristik özellikleri, Çukurova Üniversitesi'ndeki test istasyonu ve içindeki düzenekler tanıtıldı. Bu bölümün sonunda ÇÜ test istasyonunda Hamamatsu firmasının R7378A modelindeki PMT'lerin ölçümleri anlatıldı ve ölçüm sonuçları analiz edilip tartışıldı. Üçüncü bölüm CASTOR kalorimetresinin 2008'de yapılan test hüzmesi (TB08) hakkındadır. Genel olarak CERN/SPS/H2 test hüzme alanı, bu alanda bulunan çeşitli dedektörler ile CASTOR'un daha önce yapılmış test hüzmelerinin sonuçları açıklandı ve son olarak da TB08'de değişik parçacıkların (pion, elektron ve muon), değişik enerjilerde alınan test verilerinin analizleri (enerji çözünürlüğü, enerji lineerliği, çağlayanların enine ve boyuna gelişimleri) yapıp sonuçları tartışıldı. Dördüncü bölüm, CASTOR'un CMS'deki kurulumu ile ilgilidir. Kurulumdan sonra, CASTOR bölgesindeki magnetik alan, oradaki alanın etkisinden dolayı CASTOR'daki hareketlenme, PMT sinyallerinin kazançları hakkındaki ilk sonuçlar verildi ve tartışıldı.

Anahtar Kelimeler: LHC, CMS - CASTOR, ÇU test laboratuvarı - PMT - Kazanç, TB08, Kurulum

ACKNOWLEDGEMENT

I would like to thank my dear supervisor Prof. Dr. Gülsen Önengüt for her precious guidance, encouragement and support during my MSc and PhD degrees. It was a pleasure for me to work with her. She has been not only a mentor to me but also a model scientist to imitate.

I would like to thank mainly Assoc. Prof. Dr. İsa Dumanoğlu for his friendship, guidance, encouragement and support and also ÇÜ High Energy Physics group students, Zahide Demir, Yalçın Güler, Alişah Nart, Mustafa Kurnaz, Sertaç Öztürk, Gül Önengüt Gökbulut, Dilber Uzun, İlknur Hoş, Enine Gürpınar, Kadri Özdemir and Semiray Girgis for their valuable contributions on the installation of ÇÜ PMTs Test Station equipments, getting and recording the data.

I would like to thank my friends and colleagues Dr. Kenan Söğüt, Assist. Prof. Dr. Salim Çerçi and Dr. Numan Bakırcı for their support during my Test Beam analysis. Also I would like to thank members of the CASTOR collaboration. The weekly meetings we had, gave me a chance to learn a lot from them, especially Apostolos Panagiotou, Kerstin Borrás, Igor Katkov, Panagiotis Katsas, Lev Khein and other participants.

I would like to thank Wim Beaumont and Ekaterina Kuznetsova for sharing their experience during the CASTOR installation and analysis.

I would like to thank to team members of the High Energy Physics group of Çukurova University, Prof. Dr. Ayşe Polatöz, Prof. Dr. Aysel Kayış Topaksu and Prof. Dr. Eda Eşkut for their contributions and help.

I also would like to thank Aristotle University High Energy Physics group members, Chara Petridou, Kostantinos Bachas, Christos Anastopoulos, Dimos Sampsonidis, Elektra-Athanasia Christidi and Dimitris Iliadis for their help during the time I spent in Thessaloniki.

Special thanks are due to my dear friend Dilek Gök for sharing her optimistic attitude and encouragement even at my hard times and valuable comments, suggestions and support during writing of this thesis.

Last, but not least, thanks to my beloved wife and best friend Gönül for sharing this journey with me and making it enjoyable.

My deepest gratitude is to my dear parents, my sister Yıldız and brothers Turabi, Hasan, Hüseyin and Murat.

Special thanks are to TAEK who sponsored me during the time I have spent at CERN.

CONTENTS	PAGE
ABSTRACT.....	I
ÖZ.....	II
ACKNOWLEDGMENTS.....	III
CONTENTS.....	IV
LIST OF TABLES.....	VII
LIST OF FIGURES.....	VIII
ABBREVIATIONS.....	XIV
1. INTRODUCTION.....	1
1.1. The Large Hadron Collider (LHC) Machine.....	3
1.2. The Compact Muon Solenoid (CMS) Detector	7
1.3. General Design and Description of the Centauro And SStrange Object Research (CASTOR) Detector.....	11
1.3.1. Design of the CASTOR Calorimeter.....	11
1.3.2. The Components of the CASTOR Calorimeter.....	15
1.3.2.1. The CASTOR Skeleton	15
1.3.2.2. The Tungsten Plates	15
1.3.2.3. The Quartz Plates.....	16
1.3.2.4. The Air-Core Light Guides.....	17
1.3.2.5. PMTs of CASTOR.....	17
1.3.3. Physics With CASTOR Detector.....	19
1.3.3.1. QCD Oriented Physics.....	19
1.3.3.1.(1). Multiple Parton Interactions and Underlying Event.....	19
1.3.3.1.(2). Low- x Physics; Parton Saturation.....	20
1.3.3.1.(3). Diffractive QCD	21
1.3.3.1.(4). Heavy Ion Physics, Quark-Gluon-Plasma (QGP).....	22
1.3.3.2. Discovery Physics.....	24
1.3.3.2.(1). Higgs Physics.....	24
1.3.3.2.(2). BSM Physics.....	25
1.3.3.3. Cosmic-ray Physics (Centauro's and Strangelets).....	25
2. MEASUREMENT OF THE PMTs CHARACTERISTICS.....	30
2.1. The Photomultiplier Tubes (PMTs).....	30

2.1.1. The Design of the PMTs.....	30
2.1.1.1. The Photocathode of the PMTs.....	32
2.1.1.1.(1). The Photocathode Materials of the PMTs.....	32
2.1.1.1.(2). The Spectral Response of the PMTs.....	32
2.1.1.1.(3).The Quantum Efficiency and Radiant Sensitivity for the PMTs	33
2.1.1.2. The Window Materials of the PMTs.....	34
2.1.1.3. The Dynodes (Electron Multiplier) of the PMTs.....	35
2.1.1.4. The Anode of the PMTs.....	37
2.1.1.4.(1). The Gain (Current Amplification).....	37
2.1.1.5. The Anode Dark Current of the PMTs.....	38
2.1.1.6. The Linearity of the PMTs.....	39
2.1.1.7. The Collection Efficiency of the PMTs.....	39
2.1.1.8. The Time Response of the PMTs.....	41
2.2. Çukurova University PMT Test Station.....	42
2.2.1. Basic Equipment in the Çukurova PMT Test Station.....	42
2.2.2. Installation of the Gain System.....	45
2.2.3. Installation of the Timing System.....	46
2.3. Measurement of the CASTOR PMTs at Çukurova University Test Station.....	47
2.3.1. The Measurements Done in the Gain Box.....	49
2.3.1.1. The Measurement of the Anode Dark Current and the Anode Current of the PMTs.....	49
2.3.1.2. The Measurement of the Cathode Current of the PMTs	51
2.3.1.3. The Gain Measurement	53
2.3.1.4. The Measurement of the Linearity of the PMTs.....	54
2.3.1.5. The Measurement of the Collection Efficiency of the PMTs	55
2.3.2. The Measurements Done in Timing Box	55
2.3.2.1. The Analysis of the PMTs Rise Time.....	57
2.3.2.2. The Analysis of the PMTs Pulse Width.....	59
2.3.2.3. The Analysis of the PMTs Transit Time.....	60
3. CASTOR TEST BEAM 2008.....	62
3.1. Environment of the Test Beam Area	62
3.1.1. The Super Proton Synchrotron (SPS)	62
3.1.2. North Experimental Area (NEA) at the SPS.....	62

3.1.3. The H2 Beam Line.....	65
3.1.3.1. Several Optic Modes of H2 beam line.....	66
3.1.3.2 .Using Several Detectors in the H2 Beam Line.....	67
3.2. CASTOR Test Beams.....	69
3.2.1. Previous Beam Tests of the CASTOR Prototypes (2003-2004-2007)	70
3.2.2. The CASTOR Test Beam 2008 Analysis.....	71
3.2.2.1. Front-End Detectors on the Prototype in H2 Beam Line.....	72
3.2.2.2. Preparation for the Analysis.....	76
3.3.3. Energy Resolution and Linearity.....	79
3.3.3.1. Energy Resolution and Linearity with Pions.....	80
3.3.3.2. Energy Resolution and Linearity with Electrons.....	83
3.3.4. Transversal and Longitudinal Distribution of the Shower.....	87
3.3.4.1. <i>X</i> -Shower Shape with Pions.....	87
3.3.4.2. <i>X</i> -Shower Shape with Electrons.....	90
3.3.4.3. <i>Y</i> -Shower Shape with Electrons.....	92
3.3.4.4. Longitudinal Distribution.....	94
4. INSTALLATION AND FIRST DATA FROM CASTOR IN CMS.....	96
4.1. Installation of CASTOR in CMS.....	96
4.2. Preliminary Data Analysis from CASTOR.....	100
5. CONCLUSION.....	104
REFERENCES.....	107
CURRICULUM VITAE	111

LIST OF TABLES**PAGE**

Table 1.1. The three generations of quarks, leptons and gauge bosons associated with the fundamental interactions according to SM.....	2
Table 1.2. Some of the LHC main parameters.....	6
Table 1.3. Some typical features of the PMTs which were considered for use in CASTOR.....	18
Table 2.1. Specifications of Hamamatsu R7378A PMTs.....	48
Table 3.1. Several features of the H2 beam line.....	65
Table 3.2. The inter calibration coefficients corresponding to the RUs.....	76
Table 3.3. Type of cuts used to clean beams.....	77
Table 3.4. Energy resolution parameters for different particle beams	87
Table 4.1. Different parts of the castor table and the CASTOR movement information.....	99
Table 5.1. Measurement results, average values at 1 kV	104

LIST OF FIGURES**PAGE**

Figure 1.1. Large Hadron Collider at CERN in Geneva, at border of Switzerland and France.....	4
Figure 1.2. The LHC layout is displayed.....	5
Figure 1.3. A different view of the CMS detector.....	9
Figure 1.4. A transverse slice through one segment of the CMS detector indicating the responses of the various detecting systems to different types of particles .	10
Figure 1.5. Positioning of CASTOR calorimeter in the CMS forward area.....	12
Figure 1.6. Pseudorapidity-azimuthal coverage of the full CMS experiment.....	13
Figure 1.7. Schematic design drawing of the full CASTOR detector.....	13
Figure 1.8. Longitudinal crosssectional view of half of CASTOR calorimeter design...	14
Figure 1.9. Front view of half of the CASTOR calorimeter design.....	14
Figure 1.10. The ½ CASTOR detector skeleton.....	15
Figure 1.11. The view of the tungsten plate.....	16
Figure 1.12. The view semi-octant quartz plate.....	16
Figure 1.13. a) Cross section of the EM light-guide with the PMT and base housing, b) Cross section of the HAD light-guide with the PMT and base housing, c) EM light-guide with the PMT base housing.....	17
Figure 1.14. Before and after irradiation of the Hamamatsu R5380Q of PMT's gain (L) and QE (R).....	18
Figure 1.15. The distribution of the number of particles (left) and energy (right) versus pseudorapidity for <i>Pb-Pb</i> at LHC.....	19
Figure 1.16. Schematic view of PYTHIA's model of the "underlying event" in a proton-antiproton collision with multiple parton interactions.....	20
Figure 1.17. $F_2(x, Q^2)$ structure function measured at HERA in proton DIS and fixed target experiments. A strong rise of F_2 as well as scaling violation is evident at small x	21
Figure 1.18. Rapidity gaps for diffractive scattering.....	22
Figure 1.19. The distribution of number of particles (right) and energy (left) distribution as a function of the pseudorapidity in <i>Pb-Pb</i> collisions.....	22
Figure 1.20. Left: Transverse energy deposited in CASTOR as a function of the impact parameter. Right: Impact parameter resolution using the total energy	

deposited in CASTOR.....	23
Figure 1.21. Feynman diagram of the VBF production mode.....	24
Figure 1.22. CASTOR contribution to a 15% increase of jet tagging efficiency when combined with the HF calorimeter.....	24
Figure 1.23. Illustration of Centauro I in Chacaltaya experiment.....	26
Figure 1.24. Schematic drawing of time evolution of Centauro fireball.....	27
Figure 1.25. Probability of Centauro and strangelet detection versus the pseudorapidity. A large fraction of the Centauro fireball decay products and strangelets are within CASTOR's acceptance.....	28
Figure 1.26. Longitudinal profile of the signal produced by strangelets of various energies, $E=6$ TeV (green), $E=8$ TeV (blue) and $E=12$ TeV (red), compared to the background estimated with the HIJING generator.....	29
Figure 2.1. The Cross-Section of the PMT.....	31
Figure 2.2. The schematic view of working principle of the PMT.....	31
Figure 2.3. Typical spectral response and emission.....	33
Figure 2.4. Typical spectral sensitivity features of standard photocathodes associated with window materials.....	35
Figure 2.5. The schematic view of the dynode (electron multipliers): (1) circular cage, (2) box-and-grid (3) linear focusing, (4) venetian blind, (5) foil and (6) MCP.....	36
Figure 2.6. Sample of gain vs. supply voltage.....	38
Figure 2.7. Collection efficiency as a function of photocathode-to-first dynode voltage.....	40
Figure 2.8. Definition of rise time and transit time for PMTs.....	41
Figure 2.9. Definition of TTS of the PMTs.....	41
Figure 2.10. Dark boxes; a) dark, anode, linearity and collection efficiency measurements done in gain box, b) timing measurements done in timing box.....	43
Figure 2.11. Voltage supplies a) Direct current (DC) supply, b) High voltage (HV) supply.....	43
Figure 2.12. Light sources a) laser, b) tungsten lamp.....	43
Figure 2.13. Neutral Density Filters (NDF) a) glass, b) quartz, c – d) colored filters....	43
Figure 2.14. Views of the front and the behind of the bases a) anode base, b) cathode base.....	44

Figure 2.15. Analog-digital and digital-analog converter.....	44
Figure 2.16. Keithley brand picoammeter.....	44
Figure 2.17. LeCroy brand oscilloscope.....	45
Figure 2.18. PIN Diode.....	45
Figure 2.19. Schematic view of the gain installation.....	46
Figure 2.20. Schematic view of the time setup.....	47
Figure 2.21. A view of the Hamamatsu R7378A PMT.....	47
Figure 2.22. Average anode dark current values of all PMTs as a function of each HV	49
Figure 2.23. Anode dark current values of all the PMTs at 1 kV.....	50
Figure 2.24. Average anode current values of all the PMTs as a function of each HV...	51
Figure 2.25. Anode current values of all the PMTs at 1 kV.....	51
Figure 2.26. Cathode current values of all the PMTs as a function of HV.....	52
Figure 2.27. Cathode current values of all the PMTs at 232 V.....	52
Figure 2.28. The average gain measurements of all the PMTs as a function of HV.....	53
Figure 2.29. Gain current values of all the PMTs at 1 kV.....	54
Figure 2.30. Anode signals of the candidate PMTs as a function of NDF.....	55
Figure 2.31. Cathode signals of the applied PMTs as a function of HV.....	56
Figure 2.32. Screenshot of the oscilloscope.....	57
Figure 2.33. Average rise time values of all the PMTs as a function of each HV	58
Figure 2.34. Rise time values of all the PMTs at 1 kV.....	58
Figure 2.35. Average pulse width values of all the PMTs as a function of each HV	59
Figure 2.36. Pulse width values of all the PMTs at 1 kV.....	59
Figure 2.37. Average transit times of all the PMTs as a function of each HV	60
Figure 2.38. Transit time values of all the PMTs at 1 kV.....	61
Figure 3.1. Layout of the North Area	63
Figure 3.2. 'PAGE-1' TV screen in the experimental huts.....	64
Figure 3.3. Upstream of the H2 beam line.....	64
Figure 3.4. CESAR software system showing beam files.....	66
Figure 3.5. Layout of the H2 detectors in NEA.....	67
Figure 3.6. A view of WCs (C and D).....	68
Figure 3.7. A view of SCINT (S1, S2 and S4).....	69
Figure 3.8. A view of MVB.....	69
Figure 3.9. Schematic view of the CASTOR prototype IV.....	71

Figure 3.10. Behavior of the scintillators (S1, S2, S3 and S4).....	72
Figure 3.11. To select single hits, first peak was used around 3σ (S1 & S2 & S4).....	73
Figure 3.12. WCs (A, B, C, D and E) information in two dimensions.....	74
Figure 3.13. The MVB signals with pedestal trigger	75
Figure 3.14. The EM signal sum vs the HAD signal sum for (a) pion beams without cuts and (b) pion beams with cuts (banana). (c) electron beams without cuts and (d) electron beams with cuts.....	78
Figure 3.15. a) the effect of cuts (one over another respectively) for electron beams and b) the effect of cuts (one over another respectively) for pion beams.....	78
Figure 3.16. Uniformity study with different particles a) for EM section (with electrons) b) for HAD section (with pions) and c) show both EM and HAD.....	79
Figure 3.17. Three mm radius cut was applied around the run center, WCC information was used, the left plot doesn't have radius cuts and the right one has radius cut for pion run.....	80
Figure 3.18. For pion runs (20, 30, 50, 80, 100, 120, 150, 300 GeV), full length (14 RUs) Saleve+Jura side response was used.....	81
Figure 3.19. The relative energy resolution of the prototype, σ / E , with respect to the incident beam pion energy E	82
Figure 3.20. a) The signals as a function of incident beam energy b) normalized signal as a function of incident beam energy.....	83
Figure 3.21. Three mm radius cut was applied around the run center, WCE information was used, the left plot doesn't have the radius cuts and the right one has the radius cuts for electron runs.....	84
Figure 3.22. For electron runs (10, 20, 50, 120, 150, 180 and 200 GeV), three RUs Saleve side responses were used	85
Figure 3.23. The relative energy resolution of the prototype, σ / E , with respect to the incident electron beam energy E	86
Figure 3.24. The signals (mean)/beam energy as a function of the incident electron beam energy.....	86
Figure 3.25. a) The pion beams (80 GeV) were focused on the prototype face from end to end in x position b) Applied rectangle (cell) cut where stable constant $\Delta y = 15$ mm (between 57-72 mm) is used and x is changed from -45 mm to $+45$ mm with 1.75 mm steps.....	88

Figure 3.26. These two histograms belongs to the cell number 18, the left one is signal (response) and the right one position histogram	89
Figure 3.27. The signal mean values as a function of the x -position mean values (for all cells), the points were fitted by sigmoid curve function. The core of the shower is 5.395 mm, and the cloud of the shower is 29.11 mm, for Saleve side semi octant with pions.....	89
Figure 3.28. a) The electron beams (100 GeV) were focused on the prototype face from one end to the other along x direction b) Applied rectangle (cell) cut where stable constant $\Delta y = 15$ mm (between 57-72 mm) is used and x is changed from -45 mm to $+45$ mm with 1.75 mm steps.....	90
Figure 3.29. The three RUs response of the cell number 18, for both Saleve and Jura side for the electron beams.....	91
Figure 3.30. Signals mean values as a function of the x -position mean values for Saleve and Jura side semi octant with electron beams.....	91
Figure 3.31. The derivative results as a function of the x -position mean values the points were fitted by gauss fit function. The core of the shower is 1.288 mm for Saleve side semi octant with electron beams.....	92
Figure 3.32. a) The electron beams (80 GeV) were focused on the prototype face from beginning of the bottom side to the top side along y direction b) Applied rectangle (cell) cut where stable constant $\Delta x = 6$ mm and y is change from ~ 12 mm to 132 mm with 2.45 mm steps.....	93
Figure 3.33. The three RUs response of the cell number 18 for Saleve side were used with electron beams.....	93
Figure 3.34. Signal mean values as a function of the y -position mean values for Saleve side semi octant with electron beams.....	94
Figure 3.35. Longitudinal distribution of the response, along the depth of the CASTOR prototype.....	95
Figure 4.1. a) two halves of the CASTOR calorimeter, b) CASTOR table, HF platform and the beam pipe in $-z$ direction of the CMS.....	97
Figure 4.2. The CASTOR calorimeter was moved to the beam line level and it was covered by a special sheath.....	97
Figure 4.3. a) collar and rotating shielding, b) collar and rotating shielding without shims, and cheese wedges.....	98

Figure 4.4. Hall sensors on the middle and the front of the CASTOR ribs and the magnetic field at the CASTOR area.....	99
Figure 4.5. Distance sensor measurements before and during magnet ramping up....	100
Figure 4.6. Schematic view of sectors and modules of the CASTO.....	101
Figure 4.7. a) at 0 T all channels are powered up but several of them have no signals, b) at 3.8 T only far side is powered up in several channels, signals are faint and in various channels, which is in gap, there are no signals.....	101
Figure 4.8. Two signals, one used as reference and the other one used as a gain signal.....	102
Figure 4.9. The triangle points show the gain of the PMTs which was measured in laboratory, the full points show the gain for the same PMT from the installation.....	103

ABBREVIATIONS

ADC	: Analog to Digital Converter
ALICE	: A Large Ion Collider Experiment
APD	: Avalanche Photo Diode
ATLAS	: A Toroidal LHC ApparatuS
BFKL	: Balitski-Fadin-Kuraev-Lipatov
BT08	: Beam Test 2008
BSM	: Beyond Standard Model
CASTOR	: Centauro And STRange Object Research
CERN	: Conceil Europeenne pour la Recherche Nucleaire
CMS	:Compact Muon Solenoid
DC	: Direct Current
DGLAP	: Dokshitzer-Gribov-Lipatov-Altarelli-Parisi
EWK	: Electroweak
EM	: Electro Magnetic
G	: Gain
HAD	: Hadronic
HF	: Hadronic Forward
HV	: High Voltage
IP	: Interaction Point
LEP	: Large Electron Positron Collider
LHC	: Large Hadron Collider
LHC-b	: Large Hadron Collider Beauty Experiment
LINAC	: Linear Accelerator
MET	: Missing Transverse Energy
MVB	: Muon Veto Back
NDF	: Neutral Density Filters
NEA	: North Experimental Area
PS	: Proton Synchrotron
Q	: Quartz
QCD	: Quantum Chromo Dynamics

QE	: Quantum Efficiency
QED	: Quantum ElectroDynamics
QGP	: Quark-Gluon-Plasma
QIE	: Charge Integrator
PDF	: Parton Distribution Functions
PMT	: Photo Multiplier Tube
RHIC	: Relativistic Heavy Ion Collider
RU	: Reading Unit
SCINT	: Scintillation
SPS	: Super Proton Synchrotron
SM	: Standard Model
SQM	: Strange Quark Matter
SU	: Sampling Unit
SUSY	: Super SYmmetry
TTC	: Timing, Triggering and Control
TS	: Time Slice
UV	: Ultraviolet
VBF	: Vector Boson Fusion
W	: Tungsten
WC	: Wire Chambers
ZDC	: Zero Degree Calorimeter

1. INTRODUCTION

The theory called the **Standard Model (SM)** has been developed by particle physicists to describe what the Universe is made of and what holds it all in one. It is an elemental and comprehensive theory that explains all the building blocks of matter and their complex interactions: There are **6 quarks** and **6 leptons** and also there are **6 anti quarks** and **6 anti leptons**. The interactions are mediated by **force carrier particles**, like the photon, W^+ , W^- and the Z^0 bosons and gluons. The matter particles which are grouped into three generations according to their masses and the basic force carrier particles (bosons) are shown in table 1.1.

The interactions include attractive and repulsive forces, decay, and annihilation. There are three fundamental interactions between particles, and all forces in the universe can be attributed to these three interactions plus gravitational interaction (Perkins, 1987).

Strong interaction; the strong force keeps quarks together to form hadrons, and its carrier particles are called **gluons**. The typical time scale for this process is from 10^{-22} to 10^{-24} s (Griffiths, 1987).

Electromagnetic interaction; the electromagnetic force causes like-charged particles to repulse and oppositely-charged particles to pull. The **photon** (γ) is the carrier particle of the electromagnetic force. The typical time scale for electromagnetic interaction is from 10^{-16} to 10^{-21} s (Halzen, 1984).

Weak interaction; the weak force is responsible for the decay of massive quarks and leptons into lighter quarks and leptons. The carrier particles of the weak interactions are the W^+ , W^- , and Z^0 particles. The typical time scale for weak interaction is from 10^{-7} to 10^{-13} s. The matter around us that is stable is made up of the quarks and leptons of the first generation which cannot decay anymore because they are the lightest.

Electroweak interaction; physicists deduced that, in fact, the weak and electromagnetic forces have fundamentally equal strengths, above approximately 100 GeV. This is due to the fact that the strength of the interaction depends strongly on both the mass of the force carrier particle and the energy of the interaction. The difference between their observed strengths is because of the huge disagreement in mass between the W and Z particles, very massive, and the photon, with no mass as far as we know.

Table 1.1. The three generations of quarks, leptons and gauge bosons associated with the fundamental interactions according to SM (Elementary particle, http://en.wikipedia.org/wiki/Elementary_particle).

Three Generations of Matter

	I	II	III	
Quarks	2.4 MeV $\frac{2}{3}$ $\frac{1}{2}$ u up	1.27 GeV $\frac{2}{3}$ $\frac{1}{2}$ c charm	171.2 GeV $\frac{2}{3}$ $\frac{1}{2}$ t top	0 0 1 γ photon
	4.8 MeV $-\frac{1}{3}$ $\frac{1}{2}$ d down	104 MeV $-\frac{1}{3}$ $\frac{1}{2}$ s strange	4.2 GeV $-\frac{1}{3}$ $\frac{1}{2}$ b bottom	0 0 1 g gluon
Leptons	<2.2 eV 0 $\frac{1}{2}$ ν_e electron neutrino	<0.17 MeV 0 $\frac{1}{2}$ ν_μ muon neutrino	<15.5 MeV 0 $\frac{1}{2}$ ν_τ tau neutrino	91.2 GeV 0 1 Z⁰ weak force
	0.511 MeV -1 $\frac{1}{2}$ e electron	105.7 MeV -1 $\frac{1}{2}$ μ muon	1.777 GeV -1 $\frac{1}{2}$ τ tau	80.4 GeV ± 1 1 W[±] weak force
				Bosons (Forces)

key

mass →	2.4 MeV	
charge →	$\frac{2}{3}$	
spin →	$\frac{1}{2}$	
name →	u up	← symbol

The SM is a good theory. Experiments have verified its predictions to incredible precision, and all the particles predicted by this theory have been found except the Higgs boson which is included in the theory to explain the different masses of the particles. However, it does not explain everything. For example, gravity is not included in the SM. For each kind of matter particle there is a corresponding antimatter particle or antiparticle. If antimatter and matter are exactly equal but of opposite charge, then why is there so much more matter in the universe than antimatter? Electroweak

symmetry is not an exact symmetry because the masses of force carrying particles are different. There is a proposed mechanism for symmetry breaking, called Higgs mechanism, in the theory which predicts a new particle, the Higgs boson, which is not observed yet. The Large Hadron Collider (LHC) project at the European Organization for Nuclear Research (CERN), near Geneva, Switzerland is designed to find answers to these questions.

The Compact Muon Solenoid (CMS) is one of the two general purpose detectors on LHC which aims to answer these questions. CASTOR is a calorimeter in the forward region of the CMS (CMS TDR, 2007).

This thesis is based on the tests of photomultiplier tubes (PMTs) of CASTOR which was performed in the Physics Department of Çukurova University, the beam test 2008 (BT08) analysis of CASTOR and also installation CASTOR in CMS.

1.1. The Large Hadron Collider (LHC) Machine

The LHC is being installed in a circular tunnel with 27 km in perimeter, constructed 50-175 m below ground. It is located between the Jura mountains situated in France and Lake Geneva in Switzerland (Figure 1.1), the tunnel was built in the 1980s for the prior big accelerator, the Large Electron Positron collider (LEP).

The LHC is designed to collide head-on two opposed rotating beams of protons or heavy ions. Proton-proton collisions are planned at a centre-of-mass energy of $\sqrt{s} = 14$ TeV which is 7 times higher than the $p-\bar{p}$ collisions of Fermilab. Moreover, the LHC will supply heavy ion (lead) collisions with a centre-of-mass energy per nucleon pair of 5.5 TeV. This energy level is around 28 times higher than the Relativistic Heavy Ion Collider (RHIC) at the Brookhaven Laboratory (CMS TDR, 2007).

There are several accelerators which pre-accelerate the beams before being injected into the LHC. They are shown in figure 1.2. The beams, start in a linear accelerator (LINAC) with 50 MeV energy and are accelerated up to 1.4 GeV by a booster, till 25 GeV by the Proton Synchrotron (PS), and until 450 GeV by the Super Proton Synchrotron (SPS). Finally the beams are injected into the LHC ring where beams are accelerated up to 7 TeV per beam. Superconducting magnets are used in LHC to control the beams at such high energies. These electromagnets are made up of superconducting materials.



Figure 1.1. Large Hadron Collider at CERN in Geneva, at border of Switzerland and France.

Superconducting magnets, create a magnetic field of about 8.33 T, operating at extremely low temperatures (only 1.9 °K (-271°C)) make it possible for the protons to go around the ring. There are two beam pipes which carry the beams in opposite directions at LHC beam line. If LHC operated with ordinary magnets which can achieve a maximum field of about 2 T instead of superconducting magnets, the LHC ring would have to be at least 120 km in circumference to achieve the same collision energy.

Each beam will contain 2808 bunches of particles and each bunch will consist of as many as 1.15×10^{11} particles. The particles are so tiny that the chance of any two

colliding is very low. When the bunches pass through each other, there will be only about 20 collisions amongst 200 billion particles. However, the particle beams will cross about 40×10^6 times per second (25 ns between crossing), so the LHC will create about 800×10^6 collisions per second.

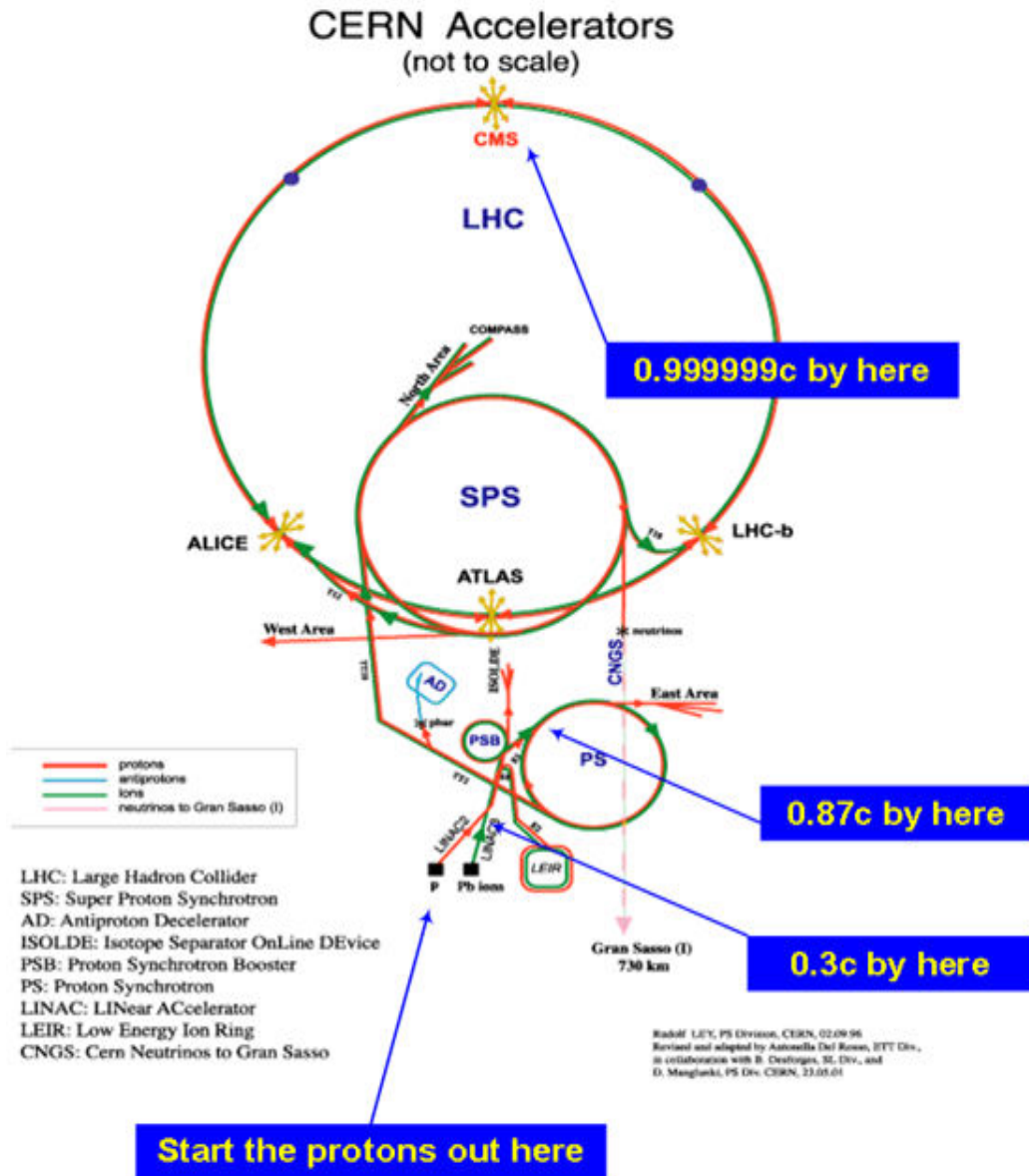


Figure 1.2. The LHC layout is displayed.

The luminosity of the collider L is proportional to the number of bunches (protons) n_1 and n_2 and the circulation frequency f , and inversely proportional to the rms of beam radii σ_x and σ_y at the collision point:

$$L = f \frac{n_1 n_2}{4\pi\sigma_x\sigma_y} \quad (1.1)$$

The number of interactions (N_i), with respect to the process i with a cross section σ_i , is given by

$$N_i = \sigma_i \int L dt \quad (1.2)$$

The table 1.2 summarizes some relevant parameters of LHC (Schmidt, 2006). The LHC is constructed to get a luminosity of $L = 10^{34} \text{ cm}^{-2} \text{ s}^{-1}$ to study proton-proton collisions. This value is approximately 100 times more than the current luminosities reached by the existing colliders. It is conceived to get a luminosity of $L=10^{27} \text{ cm}^{-2} \text{ s}^{-1}$ to study the heavy ion collision (CMS Collaboration, 2008).

Table 1.2. Some of the LHC main parameters (Schmidt, 2006).

Beam energy at collision(p-p)	7	TeV
Energy at injection	0.45	TeV
Circumference	27	km
Dipole field at 7 TeV	8.33	T
Luminosity(pp)	10^{34}	$\text{cm}^{-2}\text{s}^{-1}$
Nominal bunch spacing	25	ns
Beam size at IP / 7 TeV	15.9	μm
Distance between beams (arc)	194	mm
Energy loss/turn	7	keV
Operating temperature	1.9	K
Protons per bunch	1.15×10^{11}	
Number of bunches / beam	2808	
Number of collisions / crossing	20	
Number of dipoles	1232	
Number of quadrupoles	858	
Number of correcting magnets	6208	
Number of RF cavities	8/beam	
Beam energy at collision(pb-pb)	2.75	TeV

The first beams of LHC were circulated successfully on 10th September 2008. Unfortunately, a fault occurred on a small number of superconducting magnets on 19th September 2008. The repair required a long time which overlapped with the planned winter shutdown. The LHC beams are expected to circulate again at the end of November 2009 (LHC Machine, <http://lhc-machine-outreach.web.cern.ch/lhc-machine-outreach>).

The LHC will provide collisions at the highest energies so far observed in the laboratory conditions and physicists are willing to see what they will reveal in huge detectors at the four collision points. The main detectors in the LHC are:

The **CMS** detector (**C**ompact **M**uon **S**olenoid) is designed to explore the physics of the terascale as one of two general-purpose LHC experiments. The terascale is an energy region where physicists believe that they will find answers to the central questions at the heart of 21st-century particle physics: Are there undiscovered principles of nature? Is Higgs mechanism responsible for visible mass of the universe? How can we solve the mystery of dark energy? Are there extra dimensions of space? How did the universe come to be? (CMS TDR, 2006)

The **ATLAS** detector (**A** **T**oroidal **L**HC **A**pparatu**S**) is the world's largest general-purpose particle detector like CMS measuring particles produced in proton-proton collisions at LHC aiming to discover new physics (ATLAS TDR, 1999).

The **ALICE** (**A** **L**arge **I**on **C**ollider **E**xperiment) is going to study relativistic heavy ion interactions. The purpose of the ALICE collaboration is to study the physics of strongly interacting matter at extreme densities where the formation of a new phase of matter, **the quark-gluon plasma**, is expected (ALICE TDR, 2001).

The **LHCb** (**L**arge **H**adron **C**ollider **b**eauty experiment) is designed to study CP violation and other rare phenomena in decays of hadrons with heavy flavours, in particular *B* mesons (LHCb TDR, 2005).

The **TOTEM** detector is constructed to observe elastic scattering and diffractive dissociation and measure the total proton-proton cross section at LHC (TOTEM TDR, 2004).

1.2. The Compact Muon Solenoid (CMS) Detector

The CMS experiment which is designed to explore the physics at the TeV energy

scale is a general purpose detector at LHC. The primary aims of the experiment are to reveal the electroweak (EWK) symmetry breaking mechanism and the evidence of physics beyond the SM in proton-proton collisions at 7 TeV per beam, as well as to study the features of the strongly interacting matter produced in *Pb-Pb* collisions at the highest energy densities so far reached in the laboratory. While running in the heavy-ion mode, the two lead beams circulating in opposite directions, at an energy of 2.75 TeV per beam will be collided (CMS TDR, 2007; CMS Collaboration, 2008).

There are several alternatives to SM referring to new symmetries, new forces or constituents. Moreover, there is a great hope to discover a unified theory. The new discoveries could take the form of supersymmetry or extra dimensions, or modification of gravity. Thus there are many compelling reasons to investigate the TeV energy scale (CMS Collaboration, 2008).

The CMS is installed approximately 100 meters underground nearby the village of Cessy in French side. CMS detector measures about 21.6 m in length, 14.6 m in diameter and 12 500 metric tons in weight. The CMS detector can be seen in figure 1.3 (CMS TDR, 2007). It is typically roughly cylindrical, with different types of detectors wrapped around each other; each detector type specializes in particular particles to detect and identify. Such kind of detectors are called "hermetic" due to the fact that they are designed to let as few particles as possible to escape; the name " 4π detector" comes from the fact that such detectors are designed to cover nearly all of the 4π steradians of solid angle around the interaction point. Forward sampling calorimeters expand the pseudorapidity range to high values providing very good hermeticity (CMS Collaboration, 2008).

There are four main subsystems of the CMS; the magnet, the tracking, the calorimetry and the muon system; a strong superconducting solenoid allows the detector to keep a compact design in a high magnetic field environment (CMS TDR, 2007). The location of the central part of the detector is in a 4 T magnetic field which is parallel to the beam direction. It is 13 m in length and 6 m in diameter. Along with the central silicon pixel and microstrip tracking detector; the inner tracking system measures charged track momenta with high resolution. A high resolution electromagnetic calorimeter ($|\eta| < 3$) and a hadronic calorimeter ($|\eta| < 5$) of high granularity performs E_T^{miss} measurements and jet identification of high quality within the solenoid coil. A very good and redundant muon detection system ($|\eta| < 2.4$) is embedded in the flux

return iron yoke of the magnet.

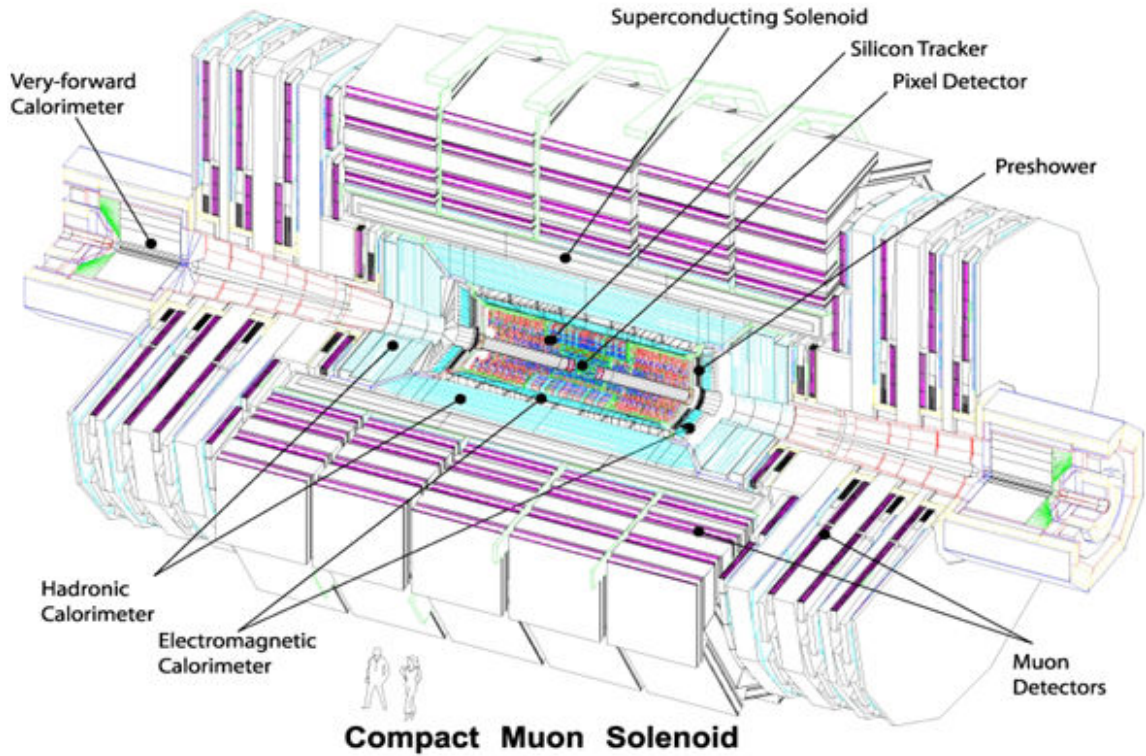


Figure 1.3. A different view of the CMS detector (CMS Collaboration, 2008).

There are two other detectors covering the very forward hemisphere; CASTOR ($5.3 < |\eta| < 6.6$) and the Zero-Degree Calorimeters (ZDC, $|\eta| > 8.3$ for neutrals). The TOTEM experiment sharing the interaction point with CMS provides two extra trackers at forward rapidities (T1 at $3.1 < |\eta| < 4.7$ and T2 at $5.5 < |\eta| < 6.6$) (CMS TDR, 2007).

The definition of the coordinate system of the CMS detector is centered at the nominal collision point inside the experiment. The y -axis is pointed vertically upward, the x -axis is pointed radially outward toward the center of the LHC. Hence, the z -axis is pointed along with the beam direction toward the Jura mountains. Generally a pseudo-spherical coordinate system is used: in the transverse plane geometry is defined by the radius, r , and the azimuthal angle Φ according to y -axis. θ denotes the polar angle which is measured from the z axis. Hence, the transverse energy and momentum to the beam direction are indicated by E_T and p_T , respectively, are calculated from the x and y components of the momenta. The disequilibrium of energy measured in the transverse plane is denoted by E_T^{miss} . Figure 1.4 shows schematic symbolizations of the response

to various types of particles superimposed on a transverse slice through the detector (CMS TDR, 2007). Pseudorapidity is a coordinate describing the angle of a particle relative to the beam axis (CMS Collaboration, 2008). It is defined as;

$$\eta = -\ln \tan\left(\frac{\theta}{2}\right) \quad (1.3)$$

where θ is the angle between the particle momentum and the beam axis. In terms of the momentum η can be written as;

$$\eta = \frac{1}{2} \ln \left(\frac{|\vec{P}| + P_L}{|\vec{P}| - P_L} \right) \quad (1.4)$$

where P_L is the longitudinal momentum. In the limit where the particle is travelling close to c , speed of light or the particle mass is close to zero, it is numerically close to rapidity which is defined as:

$$y = \frac{1}{2} \ln \frac{E + p_z}{E - p_z} \quad (1.5)$$

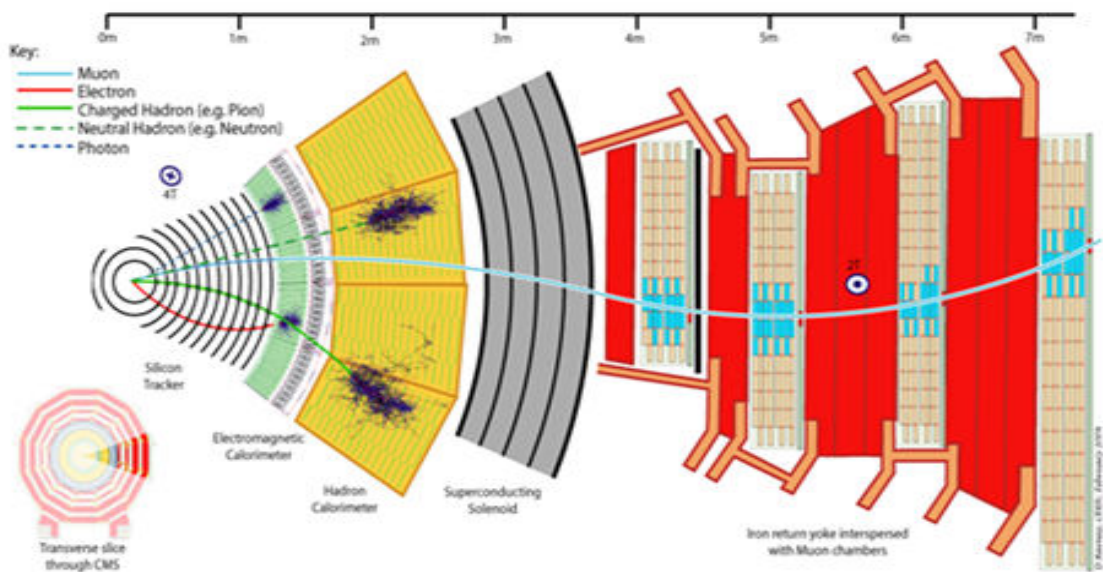


Figure 1.4. A transverse slice through one segment of the CMS detector indicating the responses of the various detecting systems to different types of particles.

The detector requirements for CMS to reach the aims of the LHC physics program can be summarized as follows:

- There must be good muon identification and momentum resolution over a wide range of momenta and angles, dimuon mass resolution must be $\approx 1\%$ at 100 GeV, the momenta of the charged muons must be smaller than 1 TeV to be determined unambiguously (CMS Collaboration, 2008).
- There should be good charged-particle momentum resolution and reconstruction efficiency in the inner tracker. Efficient triggering and offline tagging of τ 's and b-jets, require pixel detectors close to the interaction region (CMS Collaboration, 2008).
- Good electromagnetic energy resolution, diphoton and dielectron mass resolution should be around 1% at 100 GeV, wide geometric coverage, π^0 rejection, and efficient photon and lepton isolation at high luminosities (CMS Collaboration, 2008).
- To get good missing-transverse-energy and dijet-mass resolution requires hadron calorimeters with a large hermetic geometric coverage and with fine lateral segmentation (CMS Collaboration, 2008).

1.3. General Design and Description of the Centauro And SStrange Object Research (CASTOR) Detector

This chapter will describe the CASTOR calorimeter and its components. CASTOR is an international project in which several institutes from eight countries are collaborating.

1.3.1. Design of the CASTOR Calorimeter

The CASTOR calorimeter is designed in two semi-circular sections of 4-octants each in order to surround the fixed beam pipe, inner radius 3.7 cm, outer 14 cm and depth $10.5 \lambda_1$ (CASTOR Specifications; <http://cmsdoc.cern.ch/cms/castor/html/>). Figure 1.5 indicates the allowed envelope for locating the calorimeter in the CMS forward region (CASTOR EDR, 2007).

The calorimeter will be located at 14.385 m from the interaction point, in the pseudorapidity (η) range of $5.1 \leq \eta \leq 6.6$. As a matter of fact, the η -range covered will

be $5.3 \leq |\eta| \leq 6.46$ for the EM section with 99% containment and $5.25 \leq |\eta| \leq 6.31$ for the HAD section with 95% containment. Complete overlap with the HF calorimeter is ensured by the latter η range. Therefore, the CMS pseudorapidity range will be extended to a total of about 11.5 η -units by CASTOR, being only on one side of the interaction point (IP), as shown in figure 1.6 (CASTOR EDR, 2007).

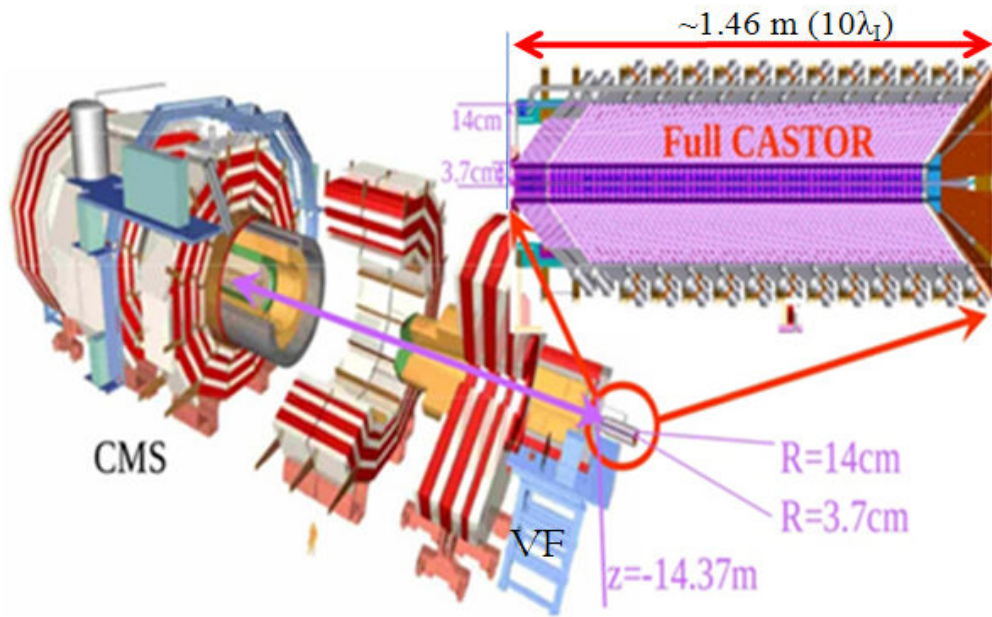


Figure 1.5. Positioning of CASTOR calorimeter in the CMS forward area.

CASTOR is a sampling calorimeter which is segmented into an electromagnetic (EM) and a hadronic (HAD) part, it is divided into 16 sectors azimuthally symmetrical around the beam pipe. It is also longitudinally divided into 14 parts, 2 for the EM and 12 for the HAD sections. The schematic design of the calorimeter is shown in figure 1.7. The construction of the calorimeter is in layers of tungsten (W) plates as the absorber sandwiched by fused silica quartz (Q) plates as the active medium which is called a “sampling unit” (SU) (CASTOR EDR, 2007).

The passage of the charged particles produces signals of Cherenkov radiation forming showers (primarily e^+ , e^-) through the quartz medium. The index of refraction of quartz is $n = 1.46-1.55$ for the wavelengths $\lambda = 600-200$ nm. The Cherenkov threshold velocity is $\beta_c = 1/n = 0.65-0.69$, and consequently, for $\beta_c \approx 1$ the angle of emission is $\theta_c = \arcsin(1/n \beta) = 46^\circ-50^\circ$ (CMS TDR, 2006; CMS TDR, 2007; CASTOR EDR, 2007).

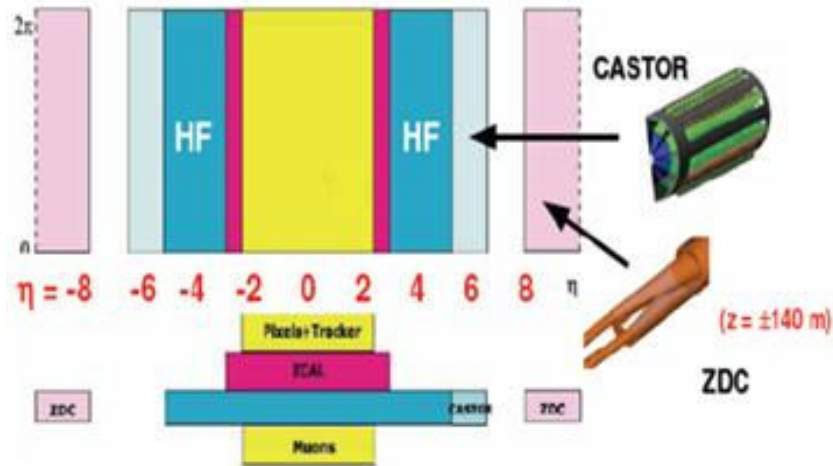


Figure 1.6. Pseudorapidity-azimuthal coverage of the full CMS experiment (CASTOR EDR, 2007).

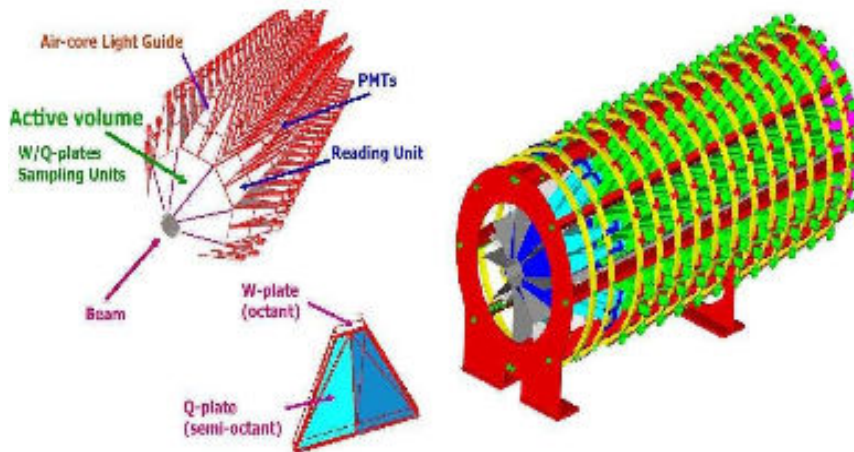


Figure 1.7. Schematic design drawing of the full CASTOR detector (CASTOR EDR, 2007).

There are 5 tungsten and 5 quartz layers, per subdivision, which is also called a reading unit (RU or channel), in both the EM and HAD sections (CASTOR EDR, 2007). The electromagnetic part has $32(2 \times 16)$ channels and a depth of $2 \times 10 = 20X_0$ (radiation lengths). The EM depth is equal to 0.77 interaction lengths. Each EM channel (RU) contains 5 tungsten and 5 quartz plates of thickness 5 mm and 2 mm, respectively. The hadronic section has $192(12 \times 16)$ channels and depth $12 \times 0.77 = 9.24 \lambda_1$ (interaction lengths). Each HAD RU contains 5 tungsten and 5 quartz plates of thickness 10 mm and 4 mm, respectively. The tungsten/quartz (W/Q) plates are located within eight octant stainless steel trapezoidal-shaped containers and are inclined at $\sim 45^\circ$

to the hitting particles for the maximum Cherenkov light production. The light which is collected from SU is focused by air-core light guides onto the corresponding PMTs as shown in figure 1.8 (CMS TDR, 2006; CMS TDR, 2007; CASTOR EDR, 2007). In total the detector has 16×14 subdivisions (224 channels).

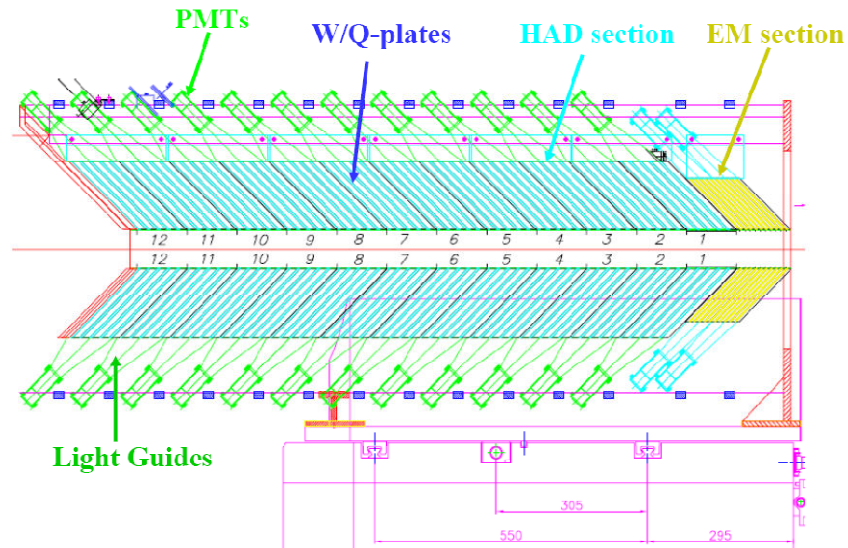


Figure 1.8. Longitudinal cross-sectional view of half of CASTOR calorimeter design (CASTOR EDR, 2007).

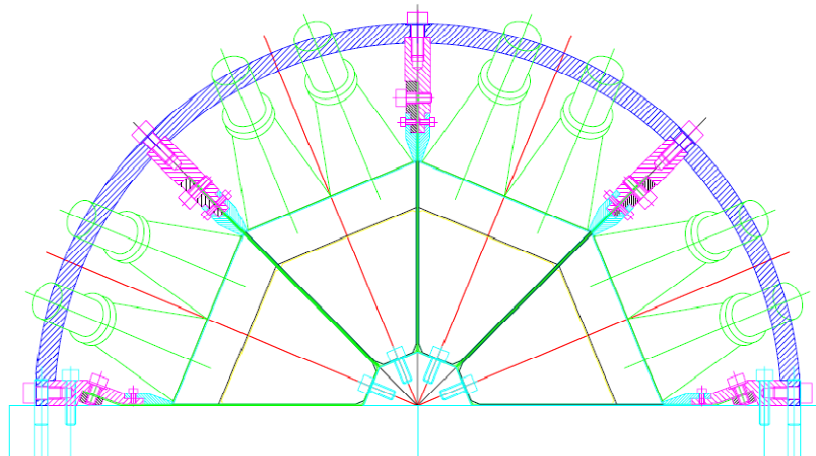


Figure 1.9. Front view of half of the CASTOR calorimeter design (CASTOR EDR, 2007).

The front view of the detector design, with the four octants forming half of the calorimeter is shown in figure 1.9. The subdivision of each octant into two semi-octants

(eight-section segmentations) with the corresponding RUs are clearly seen (CASTOR EDR, 2007).

1.3.2. The Components of the CASTOR Calorimeter

1.3.2.1. The CASTOR Skeleton

In the final construction design half of the skeleton which has four octants is made from stainless steel (Figure 1.10). While this analysis was being made, the first half of the skeleton was ready. Later, the second half of the skeleton was made in DESY.

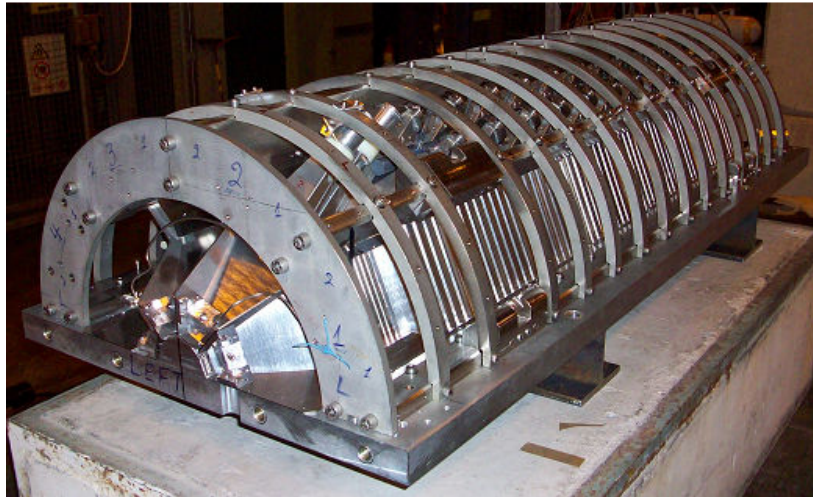


Figure 1.10. The $\frac{1}{2}$ CASTOR detector skeleton.

1.3.2.2. The Tungsten Plates

C. A. Starck GmbH fabricated the tungsten plates which are made out of tungsten alloy, containing 97% W, 1.3% Fe and 1.7% Ni. The density is $18.5 \pm 0.2 \text{ g/cm}^3$. For the EM section the thickness is 5 mm and for the HAD section the thickness is 10 mm, but the effective thickness increases to 7.07 mm for EM and 14.14 mm for HAD at 45° inclination (Dalphin, 2006). Figure 1.11 shows the octant trapezoidal shape and dimensions of the tungsten plates. The two lateral sides are tapered accordingly so as the 45° tilted plate fits in an octant wedge (CASTOR EDR, 2007).

The CERN Metrology Section measured the geometry, dimensions, consistency and density of samples of the W-plates (CASTOR EDR, 2007).

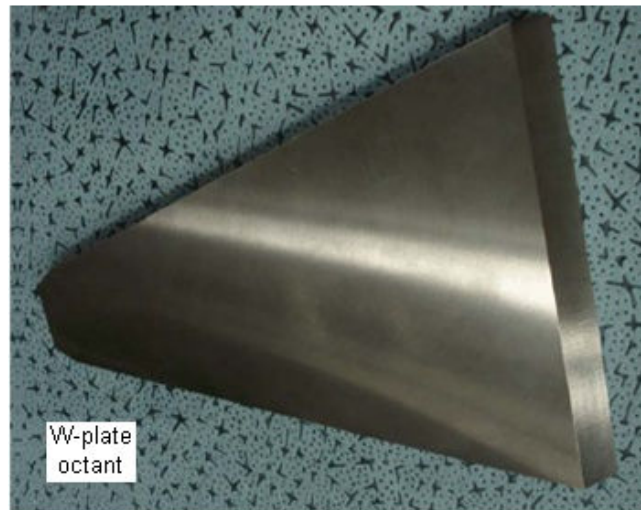


Figure 1.11. The view of the tungsten plate (<http://cmsdoc.cern.ch//cms/castor/html/>).

1.3.2.3. The Quartz Plates

The quartz plates designed in semi-octant geometry define the 16-section azimuthal segmentation of the calorimeter. For the EM and HAD sections the thicknesses are 2 mm and 4 mm respectively. The figure 1.12 shows the semi-octant construction designs of the EM and HAD Q-plates. The two semi-octants (Right, Left) are located side by side along their vertical side and are optically separated by thin Al foil. The light guides are located on top of the semi-octant quartz plates (Sampling Units) to form the RU (CASTOR EDR, 2007).

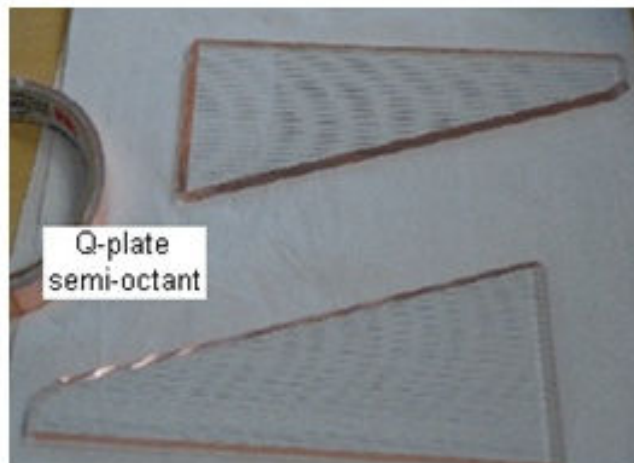


Figure 1.12. The view semi-octant quartz plate (<http://cmsdoc.cern.ch//cms/castor/html/>).

1.3.2.4. The Air-Core Light Guides

Total reflection at the quartz plate upper edge mostly channels the Cherenkov photons, generated in the 5 quartz plates of each RU of the calorimeter, and air-core light guides collect and transmit them to the PMTs. The efficiency of light spread and its dependence on the light-source position are very important parameters, which characterize the light guide and crucially affect the performance of the detector. Figures 1.13 (a, b, c) show the design drawings of the EM and HAD light guides, respectively (CMS TDR, 2006).

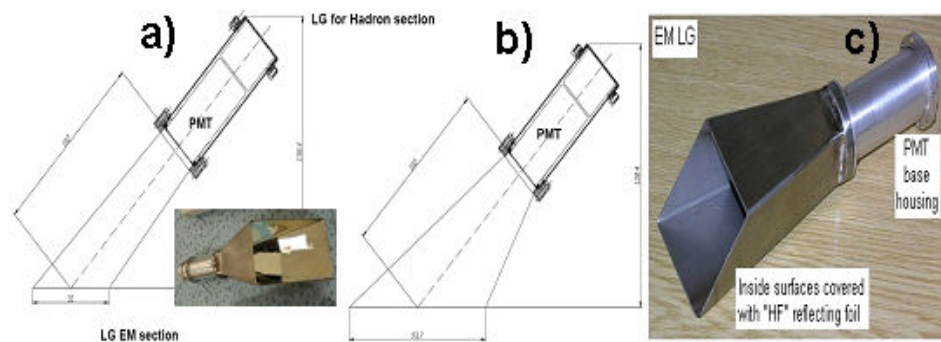


Figure 1.13. a) Cross section of the EM light-guide with the PMT and base housing, b) Cross section of the HAD light-guide with the PMT and base housing, c) EM light-guide with the PMT base housing (CASTOR EDR, 2007).

Reflecting foil covers the inside walls of the light guides to transmit the Cherenkov light. The reflecting platform is an aluminum reflector facing dielectrics SiO_2 and TiO_2 , the same one used in HF. Tyvek paper is used as an emitter for the small fraction of light that may escape through the surfaces at incidences smaller than the total reflection angle. Furthermore, tyvek preserves the polished quartz plate's interface with tungsten (CASTOR EDR, 2007).

1.3.2.5. PMTs of CASTOR

The Photomultiplier tubes (PMTs) are the last main part of the calorimeter which will collect the light and produce signals proportional to the amount of light coming from the light guide. PMTs and their components will be discussed in more detail in one of the coming chapters (2.1, 2.2 and 2.3).

It was considered to use three types of PMTs in CASTOR: Hamamatsu R5380Q-sel, R7378A and RIE FEU187. In one of the coming chapters some parameters (gain, timing etc) of Hamamatsu R7378A will be discussed in more detail (CASTOR EDR, 2007). In final installation Hamamatsu R5505 PMTs were used.

The Hamamatsu PMTs have a radiation hard synthetic silica entrance window, meanwhile the RIE have a radiation hard glass housing (CASTOR EDR, 2007).

The R5380Q was irradiated up to 18 Mrad with a Co-60 gamma source and showed very small (the order of 5%) changes of the gain and the Quantum Efficiency (QE) after the irradiation. Before and after the irradiation changes can be seen on gain and QE in the figure 1.14 (CASTOR EDR, 2007).

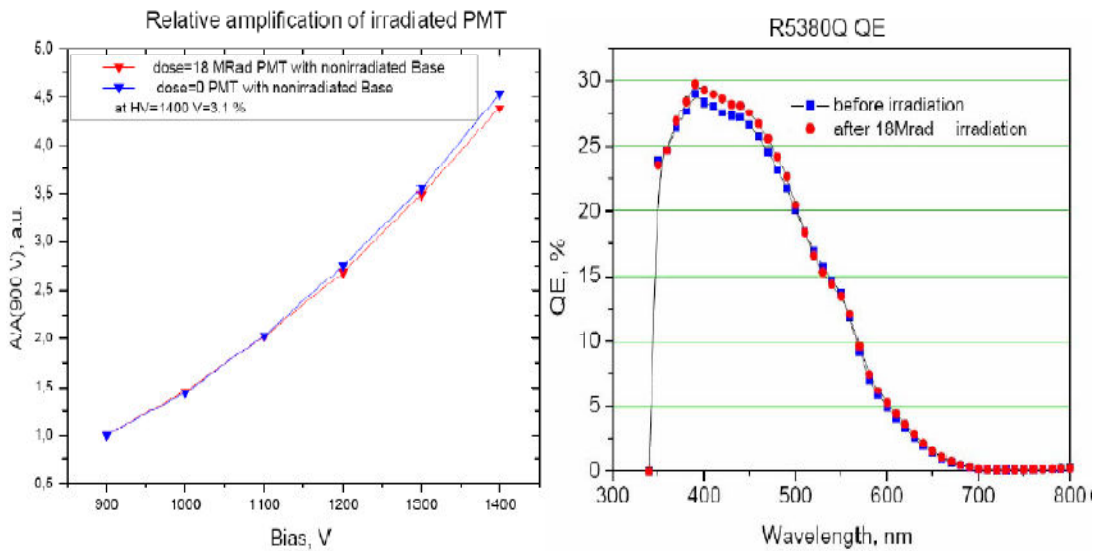


Figure 1.14. Before and after irradiation of the Hamamatsu R5380Q of PMT’s gain (L) and QE (R) (CASTOR EDR, 2007).

Table 1.3. Some typical features of the PMTs which were considered for use in CASTOR (CASTOR EDR, 2007).

PMT Type	Gain @ 1000V	Anode D.C. @ 1000 V	Rise Time @ 1000 V	Electron Transit/Spread
R5380Q-SEL	6×10^3 (6-stage)	10 nA max	1.6 ns	12 ns
R7378A	2×10^6 (10-stage)	20 nA max	1.5 ns	17/0.9 ns
FEU187	5×10^4 (12-mesh)	-----	-----	-----

1.3.3. Physics with the CASTOR Detector

The usage of CASTOR in the CMS experiment will increase its capacity both for proton-proton and heavy-ion collisions. The physics reached by CASTOR is increased because one can relate its measurements with data from the other CMS detectors.

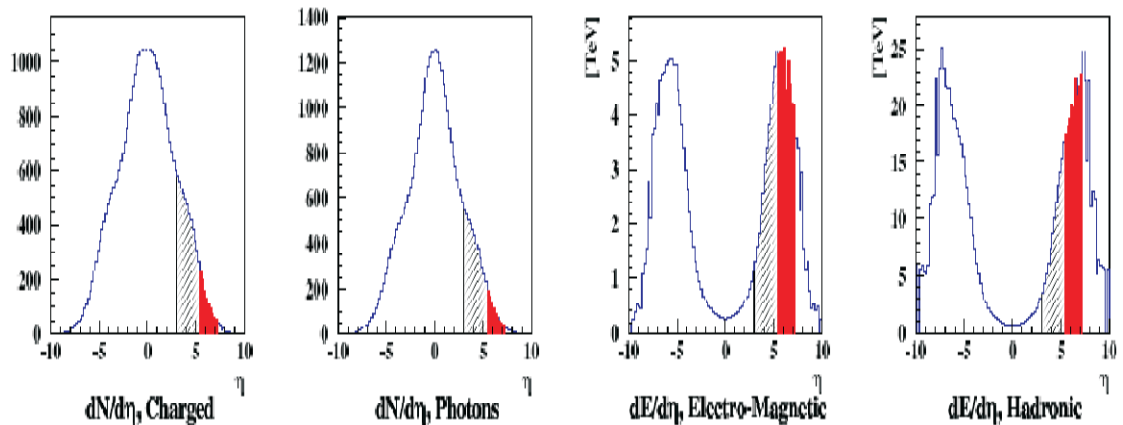


Figure 1.15. The distribution of the number of particles (left) and energy (right) versus pseudorapidity for $Pb-Pb$ at LHC (Norbeck, 2006).

HF, CASTOR, ZDC and the central calorimeters will provide an almost hermetic measurement of the flow of particles and energy. Figure 1.15 illustrates the region of pseudorapidity which is particularly important and is covered by CASTOR. It will contribute mainly to 1) new discoveries (Higgs, BSM, Centauro), 2) QCD (diffractive, low- x physics and multi-parton interactions, quark-gluon-plasma, Bjorken- x whose values that are 200 times smaller than the smallest values available at RHIC requires small angles and large Q^2 for $Pb-Pb$ collisions (Norbeck et al., 2006)), and 3) cosmic ray physics, as examples for the interdisciplinary topics accessible with the detector (D'Enterria et al., 2007).

1.3.3.1. QCD Oriented Physics

1.3.3.1.(1). Multiple Parton Interactions and Underlying Event

In proton-proton collisions, multiple hard interactions will happen between the

partons of the colliding beam protons. They will cause a very important uncertainty in the interpretation of certain hadronic final states produced either by new physics (Higgs or SUSY) or via double or even multiple parton interactions. In addition, an offset in energy and the multiplicity in the underlying event will be led by soft interactions between the remnants of the colliding beam protons. To gain insight into the dynamics of multiple interactions and the underlying event structure, energy-flow measurements as well as trigger on deposited energy in CASTOR are very essential. Unique information on the flow and on the EM/HAD contributions to forward particle production will be provided by CASTOR, together with the TOTEM tracking station T2 (CASTOR EDR, 2007). Figure 1.16 is a schematic simulation of a proton-antiproton collision where a hard 2-to-2 parton scattering with a certain transverse momentum happens by using QCD Monte- Carlo models.

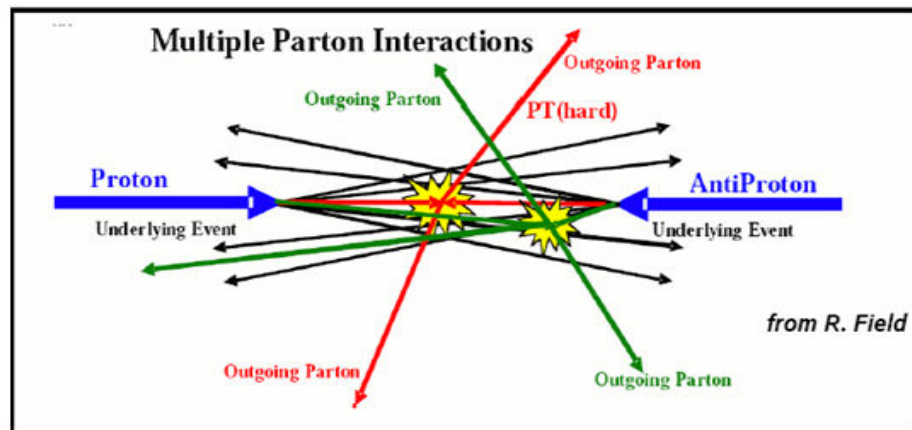


Figure 1.16. Schematic view of PYTHIA's model of the "underlying event" in a proton-antiproton collision with multiple parton interactions (Affolder, 2002).

1.3.3.1.(2). Low- x Physics; Parton Saturation

Energies and luminosities at which LHC will operate are so high that unprecedented low- x values will be gained with the possible production of hard probes for instance jets, heavy quarks or Drell-Yan pairs. The possibility to study the proton Parton Distribution Functions (PDFs) at very small parton momentum fractions ($x \sim 10^{-6}$) is opened up by the measurement of forward jets ($pp \rightarrow j X$) or Drell-Yan pairs ($pp \rightarrow l^+ l^- X$) within CASTOR's η coverage. On the contrary to the fast rise of the PDFs

seen in electron-proton collisions at such low- x values at HERA (Figure 1.17), there are such a large number of gluons that non-linear (gg fusion) QCD effects become crucial, yet not described by the linear DGLAP (Dokshitzer, 1977; Gribov, 1972; Altarelli, 1977) or BFKL (Balitsky, 1978; Kuraev, 1977; Lipatov, 1976) equations, leading to parton saturation (Heavy Ion Physics TDR, 2007). The ability to measure jets with a large separation (“Mueller-Navelet” dijets) serving as an optimal probe of BFKL and gluon saturation evolution at low- x is also offered by the existence of two CASTOR detectors on either side of the interaction point (Mueller and Navelet, 1987).

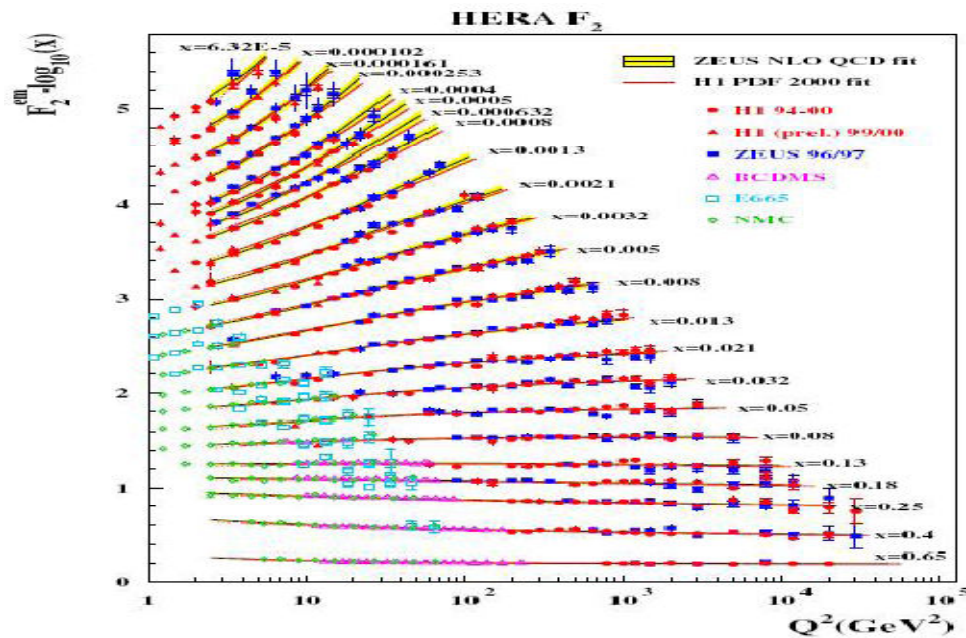


Figure 1.17. $F_2(x, Q^2)$ structure function measured at HERA in proton DIS and fixed target experiments. A strong rise of F_2 as well as scaling violation is evident at small x (Adloff et al, 2001).

1.3.3.1.(3). Diffractive QCD

CASTOR can provide a significant contribution to the study of diffractive processes. Because of the exchange of two-gluons in a colour singlet state, one or both protons remaining intact after the interaction ($pp \rightarrow pp X$) characterise diffractive events. A large rapidity gap from the reaction products (X) is used to separate those protons (Arneodo and Diehl, 2005) and CASTOR can perform a service as a precious experimental tool in tagging such rapidity gaps, because of the expanded rapidity

coverage that the calorimeter offers. Due to the relatively high rate of diffractive events – their cross section accounts around 1/4 of the total proton-proton cross section – to gain a correct projection of the expected pile-up activity in high-luminosity proton-proton scenarios a reliable measurement of soft and hard diffractive interactions is important (CASTOR EDR, 2007).

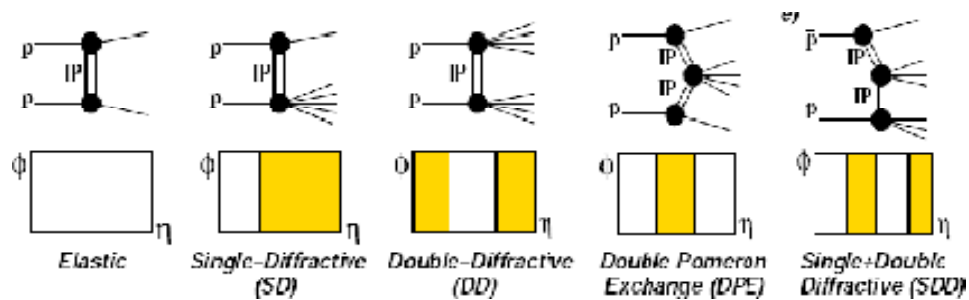


Figure 1.18. Rapidity gaps for diffractive scattering (D’Enterria, 2007).

1.3.3.1.(4). Heavy Ion Physics, Quark-Gluon-Plasma (QGP)

The optimal use of the CASTOR in the basic L1 trigger and centrality determination for heavy-ion collisions at the LHC is allowed by this device forward coverage and fast response (CASTOR EDR, 2007). Though a relatively small number of particles will be produced within its acceptance, they will carry a large fraction of the total energy flow. Because of this, the pseudorapidity region of CASTOR is very important for the study of heavy-ion collisions (Figure 1.19).

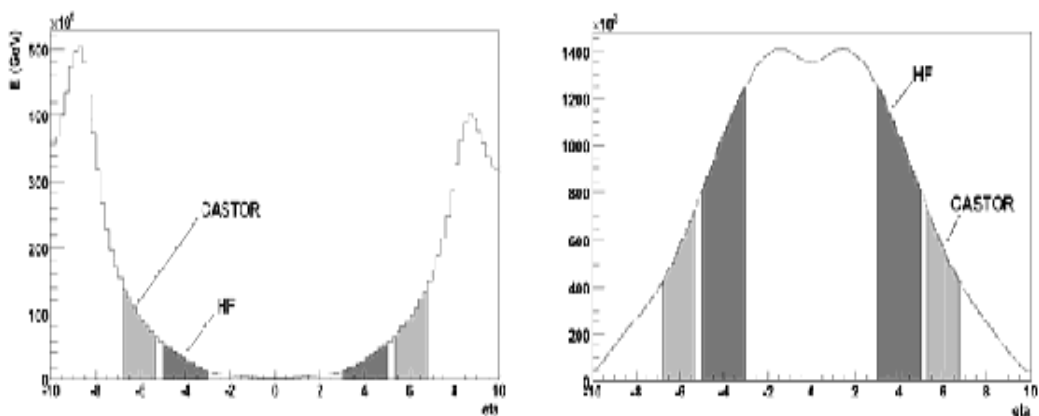


Figure 1.19. The distribution of number of particles (right) and energy (left) distribution as a function of the pseudorapidity in *Pb-Pb* collisions.

A monotonic correlation with the transverse or total energy is shown by the impact parameter of the colliding ions. Therefore, an estimate of the event centrality through the measurement of the energy deposited within its forward eta window can be provided by CASTOR. The resolution of the impact parameter is measured to be approximately 0.6 fm, using just the total energy deposited in the forward region of CASTOR (D'Enterria et al., 2007). The multiplicities of the $Pb - Pb$ particles, which is measured through their energy in CASTOR rapidities, are in the “limiting fragmentation” range in which the prediction of a reduced hadron density is approached by Colour-Glass-Condensate (CGC). Moreover, a relatively large net baryonic content characterises this kinematic regime in order to provide a unique view of the baryochemical-potential dependence of the properties of the QGP produced in $Pb - Pb$ collisions (CASTOR EDR, 2007). Also CASTOR will play an important role on the study of hard probes at forward rapidities, extending the studies that will be made for the pp runs (Figure 1.20).

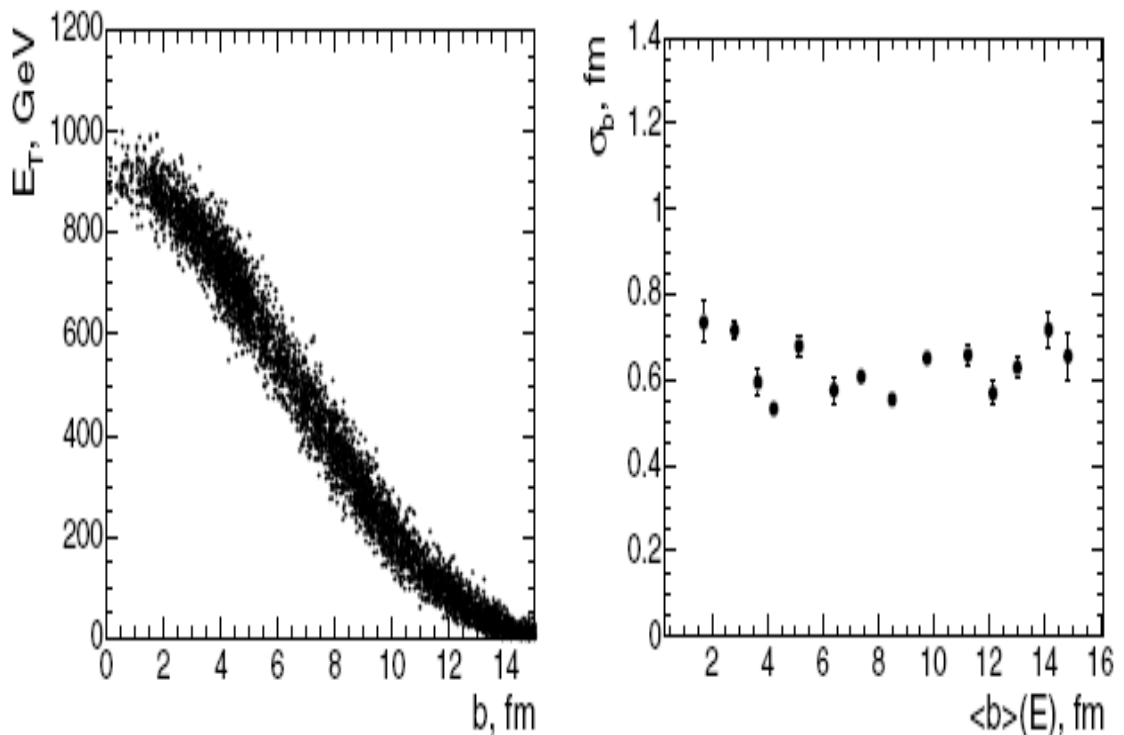


Figure 1.20. Left: Transverse energy deposited in CASTOR as a function of the impact parameter. Right: Impact parameter resolution using the total energy deposited in CASTOR (Heavy Ion Physics TDR, 2007).

1.3.3.2. Discovery Physics

1.3.3.2.(1). Higgs Physics

The gluon-gluon fusion is a dominant process for Higgs production, however the vector boson fusion (VBF) process where virtual W bosons are radiated by quarks to form a Higgs ($pp \rightarrow qqH$), has also a large cross section at all evidential Higgs masses (Figure 1.21).

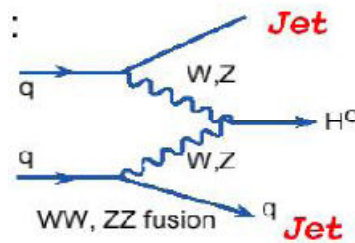


Figure 1.21. Feynman diagram of the VBF production mode (D’Enterria, 2007).

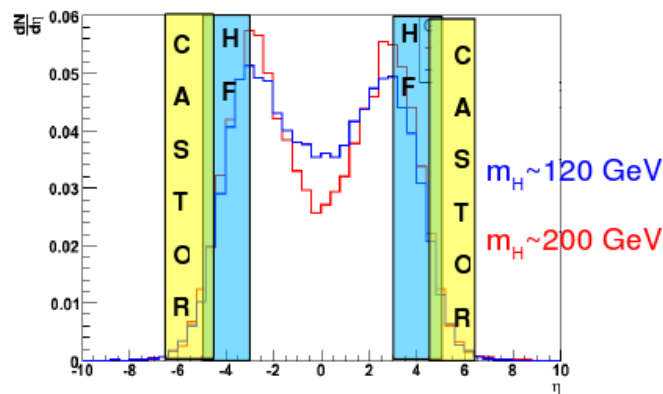


Figure 1.22. CASTOR contribution to a 15% increase of jet tagging efficiency when combined with the HF calorimeter (D’Enterria, 2008).

The VBF process is well-known for a Higgs of mass larger than about 130 GeV because the two quarks which radiate the W pair which then fuse to create the Higgs continue in the forward/backward direction and can be detected as “tag jets” (D’Enterria, 2007). The final state consists of two jets at small angles in accordance with the proton beams and a Higgs at wide angles. CASTOR can contribute to the study of the VBF production

mode by suggesting the capability of jet reconstruction in an expansion pseudorapidity range, particularly when combined with the HF calorimeter. The dN/dn distribution of VBF quarks shows that the jet tagging efficiency is increased with CASTOR by 15% (Figure 1.22) (D'Enterria, 2007).

1.3.3.2.(2). BSM Physics

A large amount of missing transverse energy (MET) characterizes many “new physics” signals. The hermiticity of the detector is one of the most crucial parameters for the search of such BSM signals. CASTOR will expand the continuous coverage of CMS from $\Delta\eta\sim 10$ to $\Delta\eta\sim 11.5$ allowing one to measure more exactly the amount of MET in $p - p$ collisions although CASTOR is not segmented in “ θ ” (CASTOR EDR, 2007).

1.3.3.3. Cosmic-ray Physics (Centauro's and Strangelets) (Gladysz-Dziadus, 2001)

Centauro related events were first discovered in high altitude emulsion chamber experiments. The first experiment was the Pamir experiment, at an altitude of 4400 meters, to observe this type of events (Figure 1.23). A “Centauro” event was first described and confirmed deeply by the Chacaltaya experiment of Brazil-Japan collaboration, conducted in the Bolivian Andes at an altitude of 5200 meters. These reported events consist of few particles, almost all hadronic, accompanied by very few photons. It is shown that at these high energies (~ 700 TeV), hadrons can be generated without neutral pions or eta mesons which decay into photons. The name of Centauro, originally from Greek mythology, is given to these events which are asymmetric and almost free of photons and has long penetrating hadronic components (Gladysz-Dziadus, 2001). High imbalance between the hadronic and photonic component, which is difficult to explain, mainly characterizes a Centauro-type event. Many models have been recommended for their explanation but the exotic nature of those events still remain.

According to the results obtained from Pamir and Chacaltaya experiments, the existence of several types of Centauro species is indicated by hadronic components. The following features characterize these events (Gladysz-Dziadus, 2001):

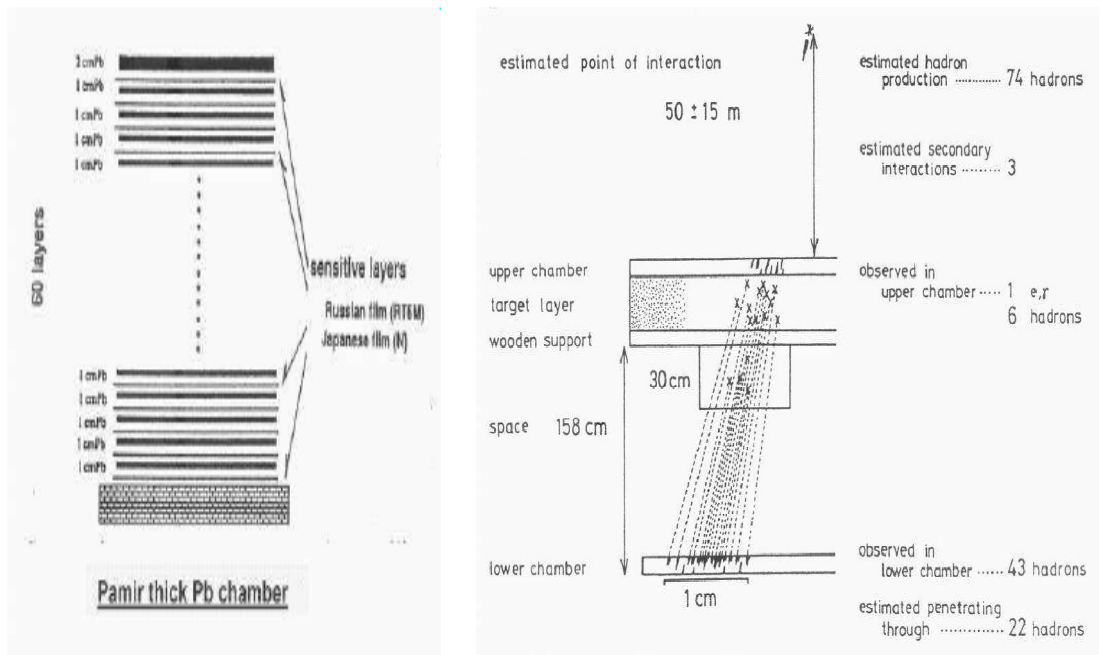


Figure 1.23. Illustration of Centauro I in Chacaltaya experiment (Gladysz-Dziadus, 2001).

- abnormal dominance of the hadrons in multiplicity and energy content,
- while comparably low total hadron multiplicity with an expected event having the same energy in nucleus-nucleus collisions,
- there is higher transverse momentum of produced particles and high energy range, for threshold energy of their production ~ 1000 TeV.

The Centauro events can be separated into several groups with respect to their characteristics, for instance: Centauros of original type called Centauro I, Mini-Centauros, Chirons, Geminions (Gladysz-Dziadus, 2001).

These abnormal events are obviously difficult to explain. The formation of a quark-gluon plasma, incorporated in scenarios with strange quark matter in heavy ion collisions is one of the possible mechanisms for the production of Centauro events.

Figure 1.24 shows the development and evolution of the Centauro fireball. To explain the basic characteristics of Centauro events, a phenomenological strange quark matter (SQM) model is proposed. The critical points of this model are discussed below, in association with the long-flying component of Centauro-type events (Gladysz-Dziadus, 2001).

Formation of a quark-matter fireball: The fireball is formed in central collisions of ultrarelativistic cosmic-ray nuclei with air nuclei, in the baryon-rich

fragmentation region. When it is formed, it contains just u , d quarks and gluons. The fireball has quite high matter density and high energy at first. The production of quarks is suppressed by large baryo-chemical potential since the very high baryochemical potential does not allow the creation of \bar{u} and \bar{d} quarks. The gluon-fusion $g \rightarrow s\bar{s}$ is the dominant mechanism (Gladysz-Dziadus, 2001).

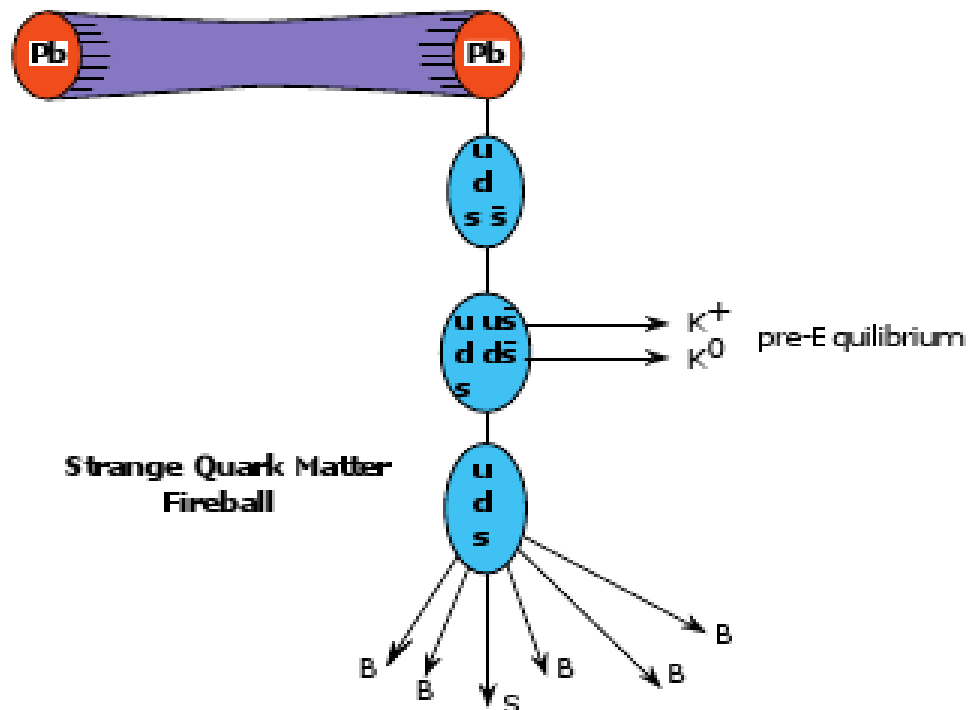


Figure 1.24. Schematic drawing of time evolution of Centauro fireball (Gladysz-Dziadus, 2001).

Chemical equilibrium: K^+ ($\bar{s}u$) and K^0 ($\bar{s}d$) mesons carrying away all strange antiquarks and positive charge can be emitted by the fireball during the relaxation time for gluon fusion state. The initial temperature and entropy are also decreased by the emitted kaons. Kaons are rapidly emitted because of their small mass and high thermal velocity. They are not seen in the ground detectors since they are lost in electro-nuclear cascade process because of their decay production to mesons in the atmosphere (Gladysz-Dziadus, 2001).

Strange quark matter state: After kaons are emitted, the Centauro fireball is a mixture of u , d and s quarks, s quarks can be emitted quickly with u and d anti-quarks. This may result in a light strange quark-matter state. Very large density, low

temperature and low value of charge to mass ratio compared to the original quark–matter fireball still characterizes the fireball. The fireball has a limited excess of s – quarks and as a result of this, it might become a long - lived strangelet, able to travel a long distance before decaying (Gladysz-Dziadus, 2001).

Hadronization: At last the Centauro fireball can decay into non–strange baryons and strangelet(s) having very high strangeness. The strangelet temperature is hoped to be lower than that predicted for Centauro fireball. Strangelets can be defined as highly deep-penetrating particles in detector materials, often accompanying the exotic cosmic–ray events. The experimental Centauro characteristics derived from five “classical Chacaltaya Centauros” are based on this scenario (Gladysz-Dziadus, 2001).

The search for droplets of SQM (so called “*strangelets*”), expected to be produced in $Pb - Pb$ collisions, is one of the main goals of the CASTOR detector. Witten (Witten,1984), also suggested the possibility of strangelets being produced by neutron stars, which could convert to more stable SQM stars and possibly reach the Earth, first proposal for the existence of stable SQM (Witten,1984).

SQM could have essential cosmological results, as for example explaining the dark matter problem. It has also been suggested that the long penetrating component observed in the Centauro cosmic ray events is associated with the strangelets (Asprouli et al., 1994; Gladysz-Dziadus, 1997).

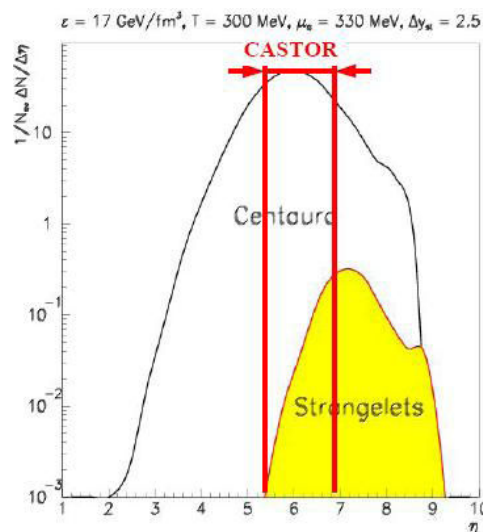


Figure 1.25. Probability of Centauro and strangelet detection versus the pseudorapidity. A large fraction of the Centauro fireball decay products and strangelets are within CASTOR's acceptance (Gladysz-Dziadus, 2001).

The probability of Centauro and strangelet detection versus the pseudorapidity, as well as the energy of the produced strangelets (Gładysz-Dziadus, 2005), as derived from a Monte Carlo generator for Centauros based on a phenomenological model (Angelis et al., 2004) is shown in figure 1.25.

The production of strangelets, which could be formed in the hot and dense environment of two colliding nuclei, is allowed to be tested in heavy-ion experiments. It is expected that strangelets are produced in the very forward region and within CASTOR's eta coverage (Figure 1.26). A preferred region is assumed to create a dense quark matter fireball, because of the richness of baryons (Gładysz-Dziadus, 2005; Angelis et al., 2004).

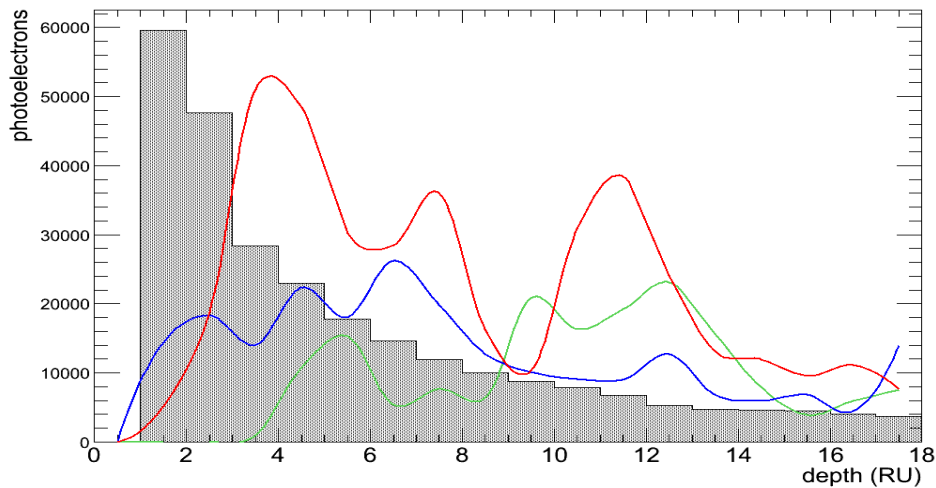


Figure 1.26. Longitudinal profile of the signal produced by strangelets of various energies, $E=6$ TeV (green), $E=8$ TeV (blue) and $E=12$ TeV (red), compared to the background estimated with the HIJING generator (Panagiotou and Katsas, 2007).

2. MEASUREMENT OF THE PMTs CHARACTERISTICS

In this chapter the measurements of the various characteristics of the photomultiplier tubes of the type R7378A of Hamamatsu brand which was intended to be used at CASTOR (chapter 1.3.2.5) Calorimeter going to describe. In table 1.3 and table 2.1 (for more details), several characteristic of the R7378A PMTs can be seen. It is very important to understand the performance of the PMTs in order to optimize the operation of the CASTOR Calorimeter. The measurements contain the anode dark current, the anode current, the cathode current, the gain, the transit time, the pulse width and the rise time. The results of the measurements are accumulated in a database. This chapter explains some basic components of the PMTs, Çukurova University PMT testing station, equipment and the testing procedure (systems) and displays the results of the measurements.

2.1. The Photomultiplier Tubes (PMTs)

Photomultiplier tubes (PMTs), are excessively sensitive detectors of light in the ultraviolet, visible, and near-infrared regions of the electromagnetic spectrum. A typical PMT is shown in figure 2.1. The signal produced by the incident light is increased by these detectors by as much as 100 million times, in multiple dynode stages, providing photons to be detected individually when the incident energy of light is very low (Photomultiplier, <http://en.wikipedia.org/wiki/Photomultiplier>).

PMTs have some important combinations such as high gain, low noise, high frequency response, and large area of collection and they are extremely important in nuclear and particle physics, motion picture film scanning (telecine), medical diagnostics including blood tests, astronomy, medical imaging, and high-end image scanners known as drum scanners (Photomultiplier, <http://en.wikipedia.org/wiki/Photomultiplier>).

2.1.1. The Design of the PMTs

PMTs consist of an input window, photocathode, focusing electrodes, a number of dynodes and an anode enveloped by evacuated glass (stem). A typical working

principle of PMT is shown in figure 2.2. Incident photons strike to the photocathode and emit electrons with low energy because of the photoelectric effect. These few electrons are accelerated and focused by the electric field towards a series of dynodes where extra electrons are produced. Each dynode has a higher positive voltage than the previous one. This showering effect generates 10^5 to 10^7 electrons for each photon hitting the first cathode depending on the series of dynodes and the accelerating voltage. At the end these electrons are accumulated at the anode where the level of the signal can be measured (PMT Design, <http://elchem.kaist.ac.kr/vt/chem-ed/optics/detector/pmt.htm>).

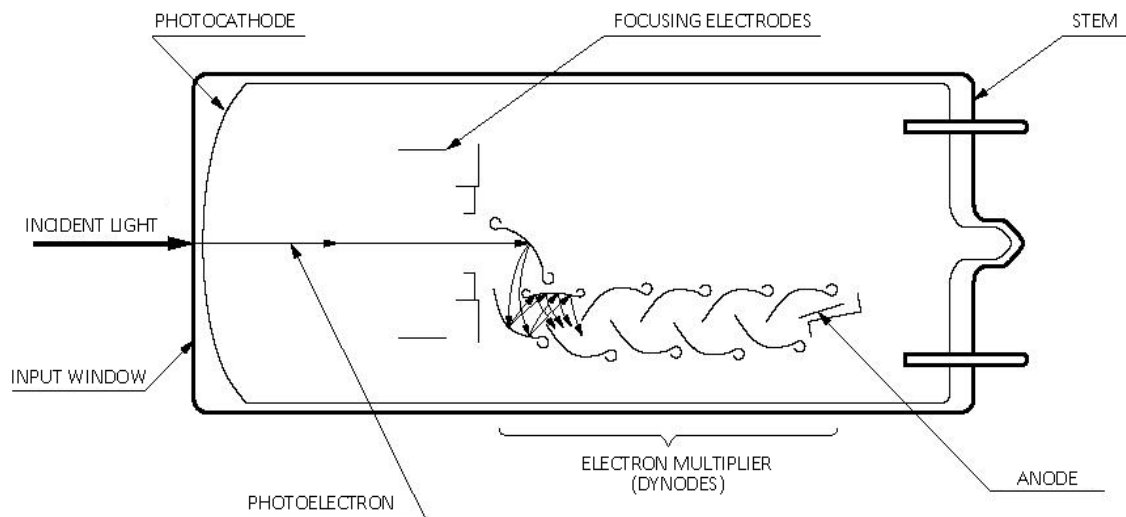


Figure 2.1. The Cross-Section of the PMT (Hamamatsu Photonics and Assemblies, 2005).

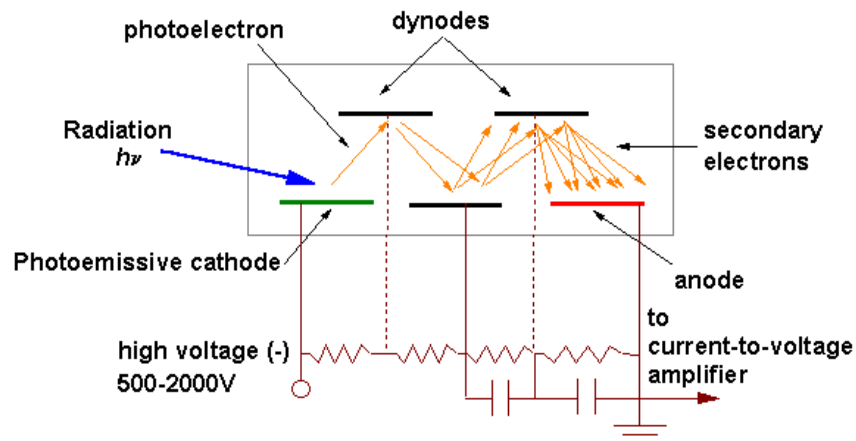


Figure 2.2. The schematic view of working principle of the PMT (PMT Design, <http://elchem.kaist.ac.kr/vt/chem-ed/optics/detector/pmt.htm>).

The head-on or end-on design, where light goes into the flat, circular top of the tube, is one of the well-known photomultiplier orientations and the side-on design, where light enters at a particular spot on the side of the tube, is the second important photomultiplier orientation. In addition, the transmission of the window material through which the light passes and the arrangement of the dynodes affect the performance of different photocathode materials. Various combinations of the dynode, window material, photocathode materials and other design variables are used for making different kinds of photomultiplier models (Photomultiplier, <http://en.wikipedia.org/wiki/Photomultiplier>).

2.1.1.1. The Photocathode of the PMTs

2.1.1.1.(1). The Photocathode Materials of the PMTs

The photocathode is a photoemissive area with very little work function. Following materials are used for high energy physics applications (Hamamatsu Photonics and Assemblies, 2005):

- **Bialkali**, has a spectral response which is suitable for the emission spectra of most scintillators. Hence, it is mostly used for scintillator applications.
- **High Temperature Bialkali**, whose major application is oil well logging, is especially useful at higher operating temperatures until 175 °C. Moreover, it can perform with very low dark current at the room temperature.
- **Extended Green Bialkali**, a variant of bialkali photocathode, has particularly high sensitivity in the green region. It fits for scintillating tile or fiber calorimeters with wavelength shifters and for CsI (TI) scintillators.

The spectral response range, defined by the materials of the photocathode and the window, is shown in figure 2.3 (Hamamatsu Photonics and Assemblies, 2005).

2.1.1.1.(2). The Spectral Response of the PMTs

Energy of the incident light is converted into photoelectrons by the external photoelectric effect of the photocathode of the PMT. The efficiency of transformation which means photocathode sensitivity depends on the wavelength of the incident light.

This dependence is called the spectral response characteristics (Hamamatsu Photonics and Assemblies, 2005).

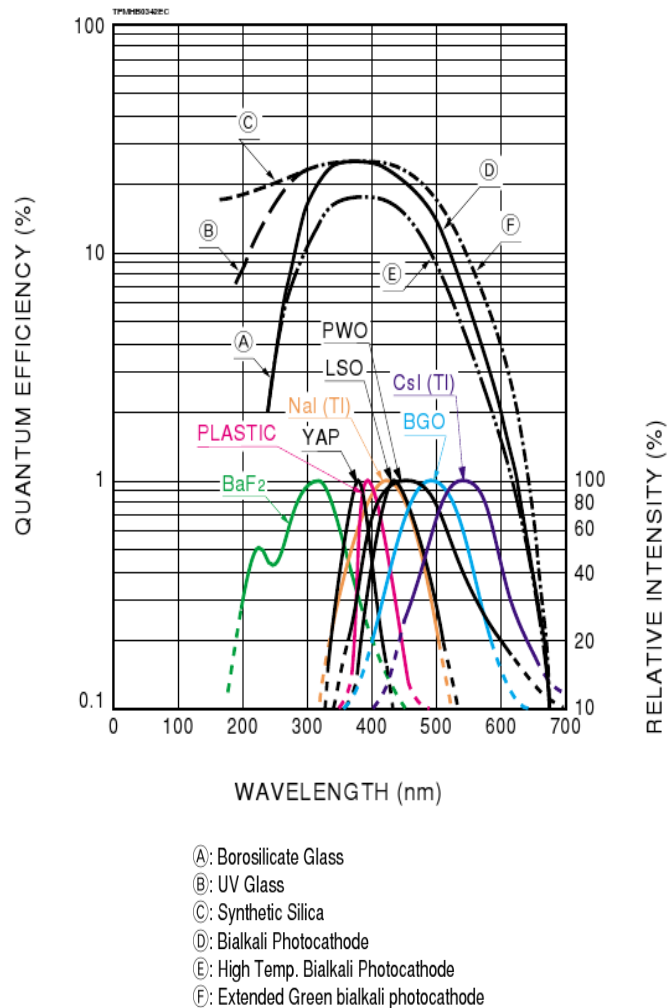


Figure 2.3. Typical spectral response and emission (Hamamatsu Photonics and Assemblies, 2005).

The photocathode material on the long wavelength edge and the window material on the short wavelength edge determine the spectral response range (Hamamatsu Photonics K.K., 2006).

2.1.1.1.(3). The Quantum Efficiency and Radiant Sensitivity for the PMTs

Quantum efficiency (QE) means the ratio of the number of photoelectrons emitted from the photocathode to the number of incident photons expressed as a percentage.

The QE equation is given below (Hamamatsu Photonics and Assembl., 2005);

$$QE = \frac{\text{Number of Photoelectrons}}{\text{Number of Photons}} \times 100(\%) \quad (2.1)$$

Radiant sensitivity (S) means the ratio of the photoelectric current from the photocathode to the incident radiant power at a given wavelength, determined in A/W (ampere per watt).

The S equation is given below (Hamamatsu Photonics and Assembl., 2005);

$$S = \frac{\text{Photoelectric Current}}{\text{Radiant Power of Light}} \quad (2.2)$$

Radiant sensitivity and quantum efficiency are related to each other at a given wavelength (Hamamatsu Photonics and Assemblies, 2005);

$$QE = \frac{S \times 1240}{\lambda} \times 100(\%) \quad (2.3)$$

where λ is the wavelength measured in nanometers.

2.1.1.2. The Window Materials of the PMTs

Some of the well known window materials used in PMTs are as follows;

- **Borosilicate glass**, is the most commonly used material, sends light from the infrared to around down to 300 nm. It includes very little potassium (K_2O and ^{40}K) which is able to create unwanted background noise because of its radioisotopes. For this reason, the low noise borosilicate glass (this is called K-free glass) may be used for scintillation counting applications.

- **UV-transmitting glass**, transmits ultraviolet light well, is widely used. The UV break off wavelength is about 185 nm.

- **Synthetic silica**, transmits ultraviolet light down to 160 nm. Silica is unsuitable for the stem material of tubes because of having a different thermal expansion coefficient from kovar metal which is used for the tube leads.

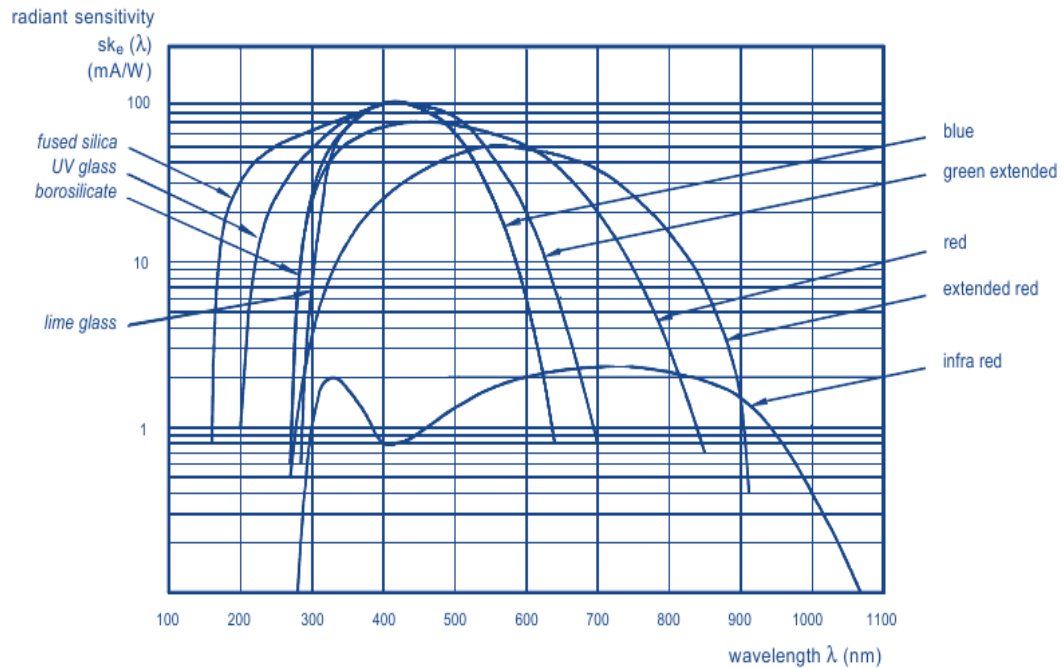


Figure 2.4. Typical spectral sensitivity features of standard photocathodes associated with window materials (Photonics, 2007).

2.1.1.3. The Dynodes (Electron Multiplier) of the PMTs

A low noise electron multiplier which increases electrons in vacuum with a secondary emission process causes the higher sensitivity (high gain and high S/N ratio) of PMT. The electron multiplier contains several stages of electrodes which are called dynodes. The main types of dynodes are shown in figure 2.5 (Photomultiplier Tubes and Assemblies, 2005; Photonics, 2007).

- **The linear-focused type** of PMTs' dynodes continuously increase the number of electrons and focus the electron paths. This type of multiplier provides fast timing characteristics, high gain and high linearity (Hamamatsu Photonics K.K., 2006; Photonics, 2007).

- **The venetian-blind type** is another type of dynodes which contains an assembly of parallel strips. This type of dynodes provide great collection efficiency, and respectable immunity to external magnetic fields (Hamamatsu Photonics K.K., 2006; Photonics, 2007).

- **The box or box and grid type** multiplier has a big collection surface at the first dynode, and therefore great collection efficiency, but a bit degraded timing

characteristics (Hamamatsu Photonics K.K., 2006; Photonics, 2007).

- **The circular cage type** multiplier leads to highly compact arrangements (Hamamatsu Photonics K.K., 2006; Photonics, 2007).

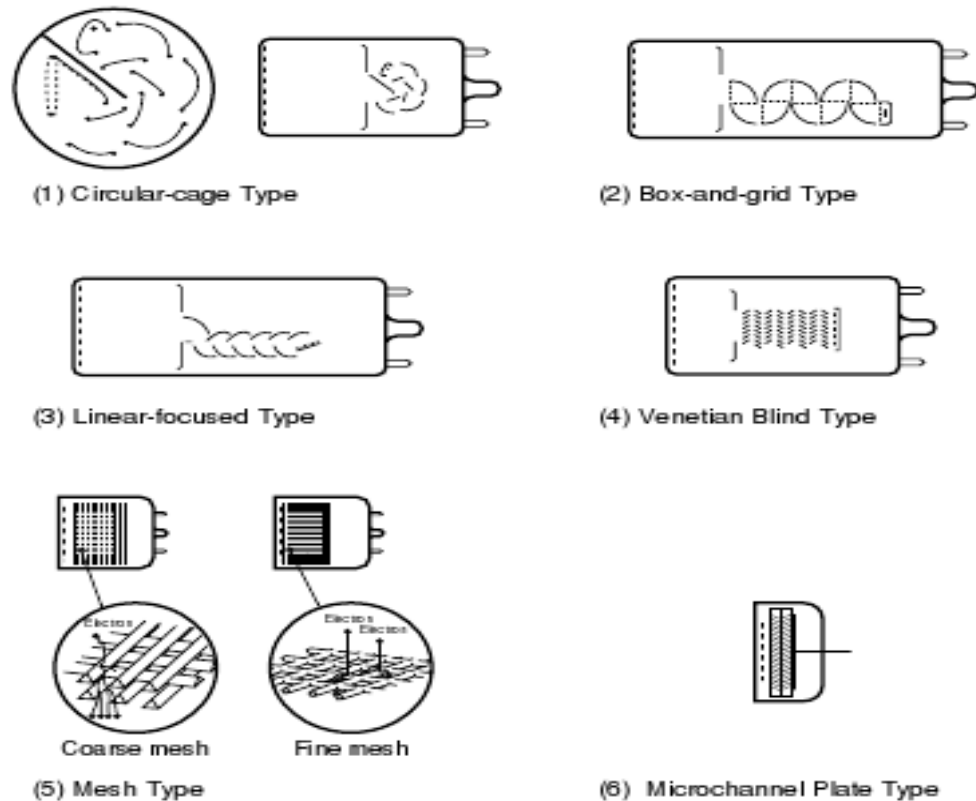


Figure 2.5. The schematic view of the dynode (electron multipliers): (1) circular cage, (2) box-and-grid (3) linear focusing, (4) venetian blind, (5) foil and (6) MCP (Hamamatsu Photonics K.K., 2006; Photonics, 2007).

- **The microchannel plate (MCP) type of dynode** multiplier contains a microchannel-plate electron increase with a proximity focused cathode at one side and an anode at the other. The microchannel plate where one electron at the input is multiplied is a compact aggregation of parallel glass tubes of microscopic diameter (6 - 25 μ) (Hamamatsu Photonics K.K., 2006; Photonics, 2007).

- **The foil** multiplier with dynodes are pierced by metal foil, which are precision-designed alternatives to standard mesh dynodes. Foil dynodes which supply quite low crosstalk are utilized in the segmented tubes of multi-channel PMTs (Hamamatsu Photonics K.K., 2006; Photonics, 2007).

2.1.1.4. The Anode of the PMTs

The anode of the PMTs is an electrode which collects secondary electrons multiplied in the cascade process through multi-stage dynodes and outputs the electron current to an external circuit (Hamamatsu Photonics Assemblies, 2005).

The PMT anode current has a relationship with the photoelectric output from the photocathode and gain. Photoelectric current is proportional to the density of the incident light (Photonics, 2007).

2.1.1.4.(1). The Gain (Current Amplification)

An electric field accelerates photoelectrons which are emitted from a photocathode to strike the first dynode and produce secondary electron emissions. These secondary electrons then beat upon the next dynode to generate additional secondary electron emissions. Repeating this cascade process, through successive dynode stages, a high gain is achieved. Thus a little photoelectric current from the photocathode can be detected as a large output current from the anode of the PMT. Gain is the ratio of the anode output current to the photoelectric current from the photocathode. Ideally the gain of the PMT is shown as δ^n , where n is the number of dynode stages and δ is an average secondary emission factor. The secondary electron emission ratio δ is given by (Hamamatsu Photonics Assemblies, 2005):

$$\delta = AE^\alpha \quad (2.4)$$

where A is a constant, E is the voltage between the dynode stages, and α is a coefficient defined by the dynode material and the geometric structure. Its value is frequently between 0.7 and 0.8. If a voltage (V) is applied between the cathode and the anode of the PMT having n dynode stages, the gain G is defined as (Hamamatsu Photonics Assemblies, 2005);

$$G = \delta^n = (AE^\alpha)^n = \left\{ A \left(\frac{V}{n+1} \right)^\alpha \right\}^n = \frac{A^n}{(n+1)^{\alpha n}} V^{\alpha n} = K V^{\alpha n} \quad (2.5)$$

(K : constant)

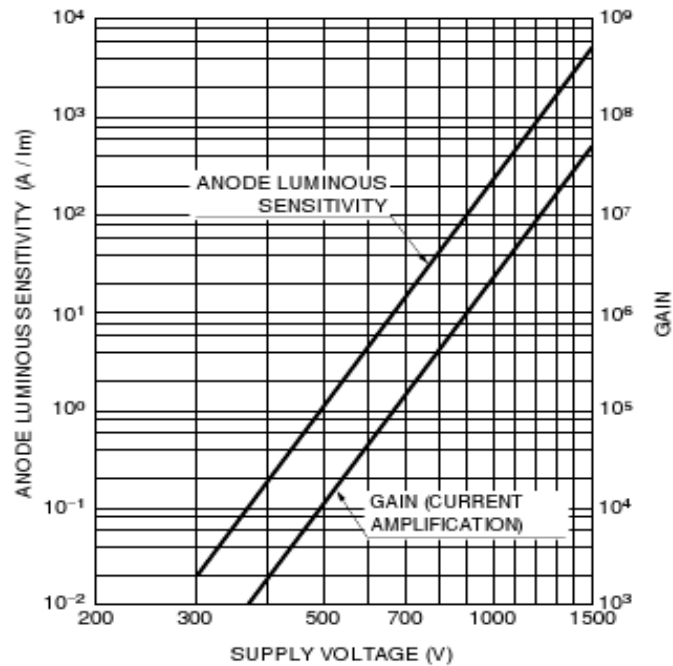


Figure 2.6. Sample of gain vs. supply voltage (Hamamatsu Photonics K.K., 2006).

Figure 2.6 shows the gain characteristics. Due to the fact that PMTs usually have 8 to 12 dynode stages, the changes in applied voltage between stages increase the anode output directly by the 6th to 10th power. The output signal of the PMT is very sensitive to fluctuations in the power supply voltage, hence the power supply should be extremely stable and demonstrate minimum ripple, drift and temperature coefficient (Hamamatsu Photonics and Assemblies, 2005).

2.1.1.5. The Anode Dark Current of the PMTs

A small quantity of output current which occurs in a PMT even if it is in complete darkness is called the anode dark current. The dark current and the noise are crucial factors to define the lower limit of light detection. Main reasons of the dark current are explained as follows (Hamamatsu Photonics and Assemblies, 2005):

- **Thermionic emission of electrons:** Because the materials of the photocathode and dynodes have very low work functions, they emit thermionic electrons even at room temperature. The dark current originates mostly from the thermionic emission of the photocathode, and it is increased by the dynodes (Photonics, 2007).
- **Ionization of residual gases:** The flow of photoelectrons can ionize the

remaining gases inside the PMT. If these ions hit the photocathode or earlier stages of dynodes, secondary electrons can be emitted. Therefore, this effect causes relatively large output noise pulses which are generally observed as after pulses following the primary signal pulses which may be a problem in detecting short light pulses (Hamamatsu Photonics and Assemblies, 2005).

- **Glass scintillation:** In case of deviation of electrons from their normal trajectories and hitting the glass envelope, scintillations may happen and dark pulses may occur. PMTs may be used with the anode at a high voltage and the cathode at the ground potential so that these pulses can be eliminated (Hamamatsu Photonics and Assemblies, 2005).

- **Ohmic leakage:** Insufficient insulation of the glass stem base and socket results in ohmic leakage which may be another source of dark current. This primarily occurs in operation of a PMT at a low voltage or low temperature. In addition dirt and humidity on the surface of the tube may create ohmic leakage (Hamamatsu Photonics and Assemblies, 2005).

- **Field emission:** In operation of the PMT at a voltage close to the maximum value, strong electric fields causing dark pulses may emit electrons from electrodes (Hamamatsu Photonics and Assemblies, 2005).

2.1.1.6. The Linearity of the PMTs

Charge linearity is the proportionality of the number of incident photons to the number of electrons collected at the anode. Current linearity is the ratio between incident flux and anode current; in this relationship therefore, time is an additional parameter. Internal and external factors set limits on both charge and current linearity (Photonics, 2007).

2.1.1.7. The Collection Efficiency of the PMTs

In order to multiply efficient electrons at each stage of dynode, the electron multiplier mechanism of a PMT is designed with consideration to the electron trajectories. Although some of the electrons can deviate from their proper trajectories, they do not contribute to multiplication very much (Hamamatsu Photonics K.K., 2005).

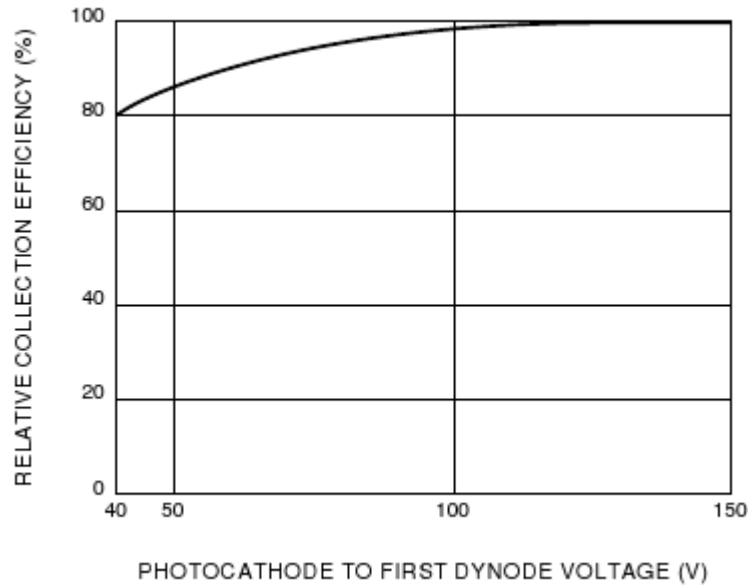


Figure 2.7. Collection efficiency as a function of photocathode-to-first dynode voltage (Hamamatsu Photonics K.K., 2005).

Generally, the probability of photoelectrons landing on the effective area of the first dynode is called the collection efficiency. The effective area is the area of the first dynode in which photoelectrons may be multiplied effectively at the successive dynode stages without deviating from their proper trajectories. In spite of existing secondary electrons which do not contribute to multiplication at the second dynode or latter dynodes, they will have less effect on the total collection efficiency as the number of secondary electrons emitted increases greatly. So the photoelectron collection efficiency at the first dynode is important. Figure 2.7 shows typical collection efficiency on photomultiplier tube (Hamamatsu R6095) as a function of cathode-to-first dynode voltage. Figure 2.7 shows that approximately 100 volts must be applied between the cathode and the first dynode. Energy resolution, detection efficiency and signal-to-noise ratio in scintillation counting are influenced by the collection efficiency. The detection efficiency is the proportion of the detected signal to the input signal of a photomultiplier tube (Hamamatsu Photonics K.K., 2005).

The collection efficiency of the PMTs, a subjective parameter, is difficult to measure and for which no standardized methods have been defined. It differs considerably between PMT types, reflecting differently designed electron-optical input systems (Photonics, 2007).

2.1.1.8. The Time Response of the PMTs

In applications where the incident light comes as pulses the anode output current signal should reproduce a waveform faithful to the incident pulse waveform. This event depends on the anode pulse time response (Hamamatsu Photonics and Assemblies, 2005). The following parameters are used to describe the time response:

- **Rise Time:** If a delta-function light pulse illuminates the whole photocathode, the time for anode output pulse to rise from 10% to 90% of the peak amplitude. It is shown in figure 2.8 (Hamamatsu Photonics and Assemblies, 2005).

- **Electron Transit Time:** The time interval between the arrival of a delta-function light pulse at the photocathode and the instant when the anode output pulse reaches its peak amplitude is called electron transit time. It is shown in figure 2.8 (Hamamatsu Photonics and Assemblies, 2005).

- **Transit Time Spread (TTS):** The fluctuation of individual pulses in transit time is called the transit time spread or the transit time jitter. It may be determined by the FWHM of the frequency distribution of electron transit times. It is related to the number of incident photons (Hamamatsu Photonics and Assem., 2005). It is shown in figure 2.9.

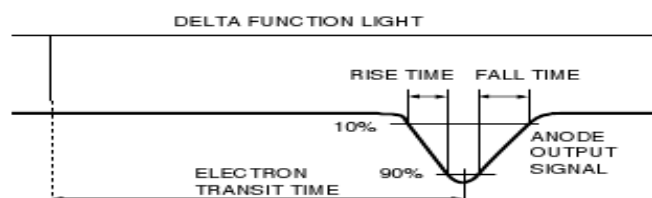


Figure 2.8. Definition of rise time and transit time for PMTs (Hamamatsu Photonics K.K., 2006).

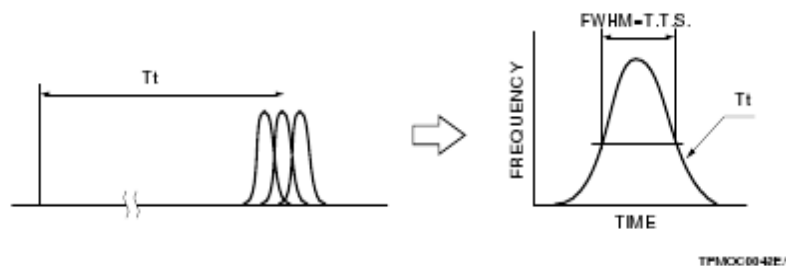


Figure 2.9. Definition of TTS of the PMTs (Hamamatsu Photonics and Assemblies, 2005).

2.2. Çukurova University PMT Test Station

The stable operation of the detector is closely related to the performance of the PMTs. With the aim of understanding the performance of the PMTs, a testing station was funded at Çukurova University in Adana.

The station was set up by funds from State Planning Organization (DPT) and Turkish Atomic Energy Commission (TAEK). The station allows us to measure several characteristics of the PMTs.

2.2.1. Basic Equipment in the Çukurova PMT Test Station

The basic equipment in Çukurova PMT test station are as follows:

1. There are two dark boxes. One of them is used for measuring dark current, anode current, linearity and collection efficiency (called gain box which has the dimensions $60 \times 72 \times 145 \text{ cm}^3$). The other box is used for measuring timing parameters (Figure 2.10). Inside of both boxes are covered with black fabric to keep light off the system and reflection of inside light. All kinds of measurements of the PMTs are done in these two boxes.
2. There are two types of voltage supplies. One of them is direct current (DC) supply which lets us feed the device from 0 to 30 volt and supports the light source and PIN diode. The latter one is a high voltage (HV) supply which is in 40 – 2400 Volt range and supports the PMTs. They can be seen in figure 2.11.
3. Four ns pulses in UV region at 337 nm are emitted by a Spectra-Physics VSL-337ND-S nitrogen laser. This laser and a halogen tungsten lamp are both used as a light source. Figure 2.12 shows them schematically.
4. There are several types of Neutral Density Filters (NDF) such as glass, quartz and in different colors. They are shown in figure 2.13.
5. There are two types of home-made bases, one for the anode current and another one for the cathode current. They are shown in figure 2.14.
6. There is an analog-digital and digital-analog converter that converts signals from analog to digital and from digital to analog. Connection to eight analog input (AI) channels, two analog output (AO) channels, 12 digital

input/output (DIO) channels, and a 32-bit counter with a full-speed USB interface are provided by the NI USB-6008/6009. It is shown in figure 2.15.



Figure 2.10. Dark boxes; a) dark, anode, linearity and collection efficiency measurements done in gain box, b) timing measurements done in timing box.

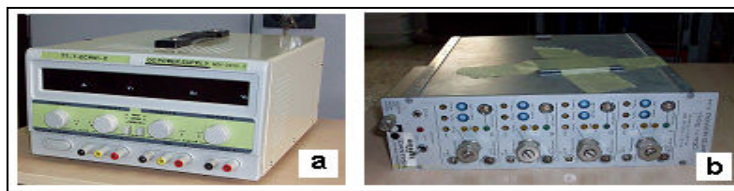


Figure 2.11. Voltage supplies a) direct current (DC) supply, b) high voltage (HV) supply.



Figure 2.12. Light sources a) laser, b) tungsten lamp.

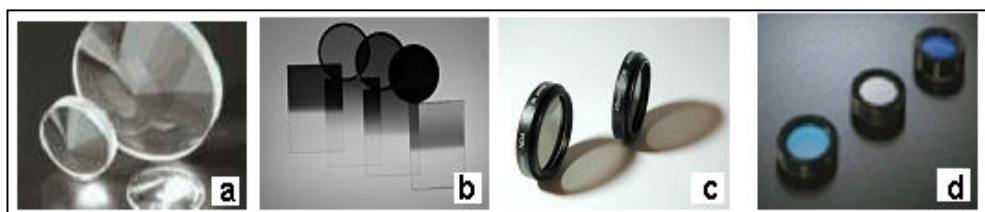


Figure 2.13. Neutral Density Filters (NDF) a) glass, b) quartz, c – d) colored filters.

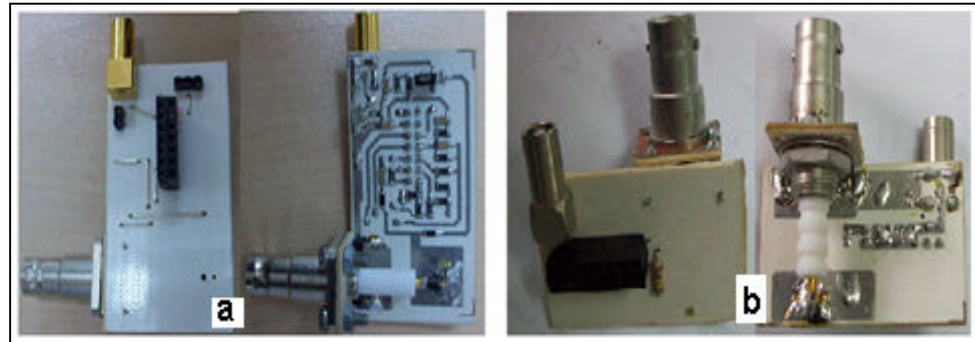


Figure 2.14. Views of the front and the behind of the bases a) anode base, b) cathode base.



Figure 2.15. Analog-digital and digital-analog converter.

7. Keithley brand digital picoammeter with 10 fA resolution (Figure 2.16) reads signals which come from PMTs. They are saved in the main control desk by NI LabVIEW program.



Figure 2.16. Keithley brand picoammeter.

8. LeCroy brand oscilloscope is used for taking the PMT timing parameters. It is shown in figure 2.17. LeCroy has combined the type of high performance front amplifier, ADC, memory and triggering and designed them all into a

very affordable package. Basic oscilloscope functions are easily at hand using the front panel knobs. It allows to zoom in to see in details on the bright touch panel color screen. It includes an industry-leading signal acquisition path which provides a 5 GS/s ADC on every channel (Model 6051 two channels) and 1 Mbyte of standard memory. This oscilloscope has 500 MHz passive probe (one per channel). This 2.5 mm high impedance probe offers excellent characteristics for probing everyday signals.



Figure 2.17. LeCroy brand oscilloscope.

9. After light leaves the beam splitter, some of it comes to the PIN Diode which creates the signal used in oscilloscope as a trigger. It is shown in figure 2.18. It is appropriate to use the PIN diode for attenuators, fast switches, photodetectors, and high voltage power electronics applications.



Figure 2.18. PIN Diode.

2.2.2. Installation of the Gain System

Some parameters of the PMTs are measured in the system which is shown in figure 2.19. In order to keep the light out of the system, the box (system) is put in a dark laboratory. The box blocks the light coming from out of the system. All measurements

(about gain) are done in that box. There are some basic parts of the system; the halogen tungsten lamp fed by the DC supply is used as a light source. Light which comes from halogen tungsten lamp passes through the NDF and reaches the PMT. There are two bases which let us feed PMT by HV and take signal from PMT. Signal coming from PMT goes to the picoammeter. The signal is taken by picoammeter in pico, nano, micro and mili amper units and is stored by the LabVIEW program in the main desk.

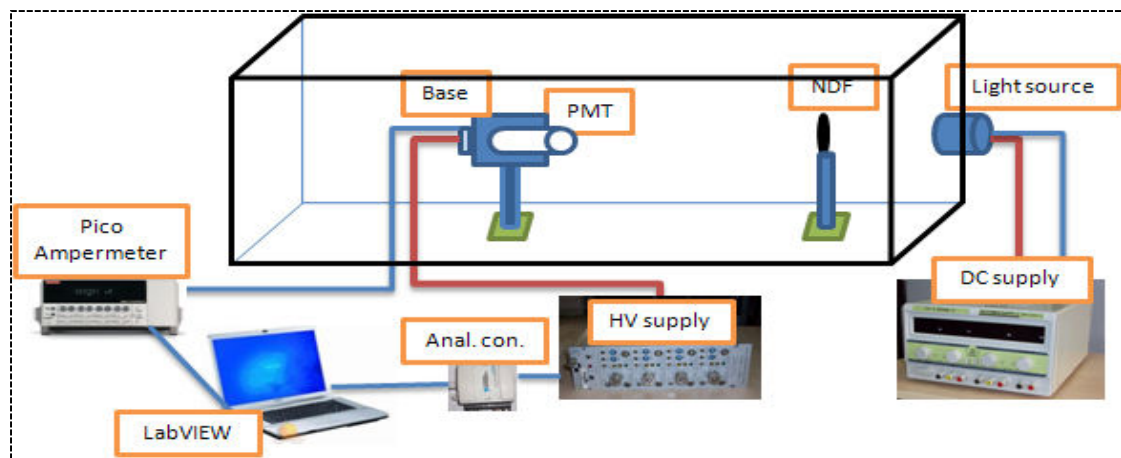


Figure 2.19. Schematic view of the gain installation.

2.2.3. Installation of the Timing System

The system used for the timing parameters studies is shown in figure 2.20. The timing box is put in a dark laboratory so that we can keep the light out of the system. The box prevents the light to enter the system. Timing measurements are done in that box. There are some basic parts of the system; the laser producing 337 nm pulse is used as a light source. Light which comes from laser passes through the NDF and reaches the beam splitter which separates the light beam into two parts (50/50). One part arrives at the PIN diode which is fed by the DC supply creates a signal and another part passes through several NDFs and then reaches the PMT. These NDFs are used to provide appropriate attenuation levels of the light. There is a base which lets us feed PMT by HV and takes signal from the PMT. At the end two signals are acquired. One of them which comes from the PIN diode is used as a trigger. The latter one comes from the PMT. Both of them go to the oscilloscope and are used to measure the timing parameters.

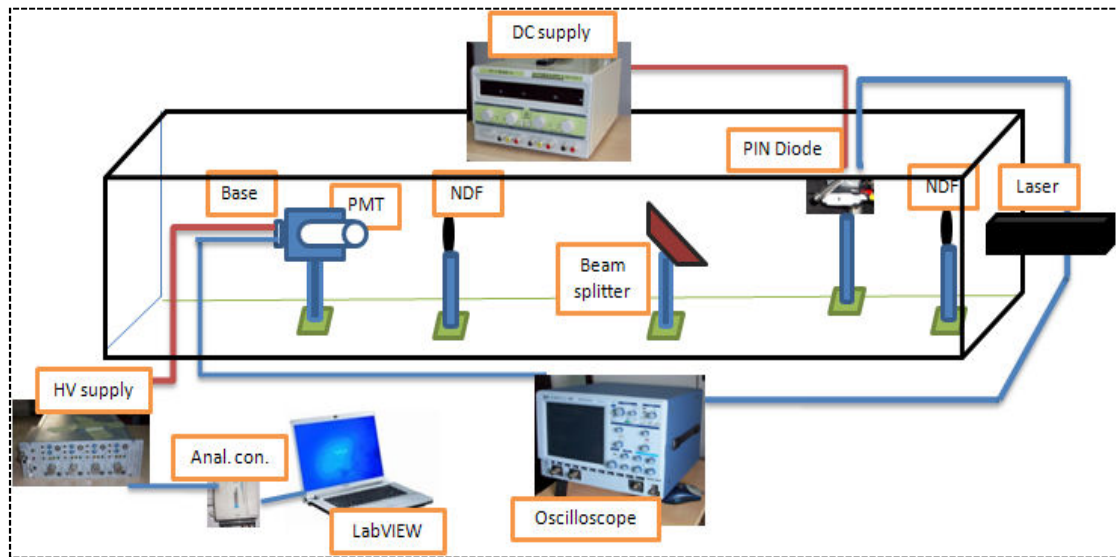


Figure 2.20. Schematic view of the time setup.

2.3. Measurements of the CASTOR PMTs at Çukurova University Test Station

Several features of the PMTs which were defined in chapter 2.1 were measured with system which was mentioned in chapter 2.2. The PMTs measurement procedures will be explained and the results will be summarized in this chapter.

The University of Çukurova Test Station was designed initially to compare measurements and if the results of the measurements were not suitable for quality control, they would be eliminated.



Figure 2.21. A view of the Hamamatsu R7378A PMT.

The laboratory in which measurements were done was kept dark and the temperature was below 25 °C.

The Hamamatsu R5380Q PMTs were tested at Çukurova University test station and results were presented at the 11th Vienna Conference on Instrumentation, Vienna, February 19-24, 2007 (Aydin et al., 2007). During May-July 2008, we tested the Hamamatsu R7378A PMTs (Figure 2.21) properties which are listed in table 2.1, as given by Hamamatsu.

Some of the tests, anode dark current, anode current, cathode current and timing parameters, were taken for all the PMTs whereas linearity and collection efficiency tests were done only on several randomly chosen PMTs.

Measurements were done in two dark boxes.

Table 2.1. Specifications of Hamamatsu R7378A PMTs.

Parameter	Value
Type	Head on
Window Material	Synthetic Silica
Total Faceplate	25.4±05 mm
Active Diameter	22 mm
Photocathode Material	Bialkali
Photocathode Effective Area	22 mm
Dynode Structure	Linear Focused
Number of Dynodes (Stages)	10
Spectral Response	160-650 nm
Peak Sensitivity	420 nm
Supply Voltage	1250 V
Average Anode Current	0.1 mA
Cathode Luminous Sensitivity	90 µA/lm
Anode Luminous Sensitivity	180 A/lm
Anode Dark Current After 30 min.	< 20 nA
Anode Pulse Rise Time	1.5 ns
Electron Transit Time	17 ns
Gain	2.0×10 ⁶

2.3.1. The Measurements Done in the Gain Box

The measurements such as anode dark current, anode current, cathode current, linearity and collection efficiency have been done in the gain box, defined in section 2.2.2. A randomly chosen PMT was measured in several different times because of the stability of the system. After finding the ideal conditions, PMTs were tested one by one. PMTs were fed by high voltage and then signals, read ten times in the picoammeter, were sent to the main desk, where the LabView programme took and saved their average values.

2.3.1.1. The Measurement of the Anode Dark Current and the Anode Current of the PMTs

In order to take PMTs anode dark current and anode current, the PMTs were fed by high voltage from 500 Volt to 1100 Volt in 50 Volt steps. For this process, the anode base was used.

A small quantity of current which can be measured in a PMT even if it is operated in complete darkness is called the dark current. The reasons for dark current can be found in chapter 2.1.1.5.

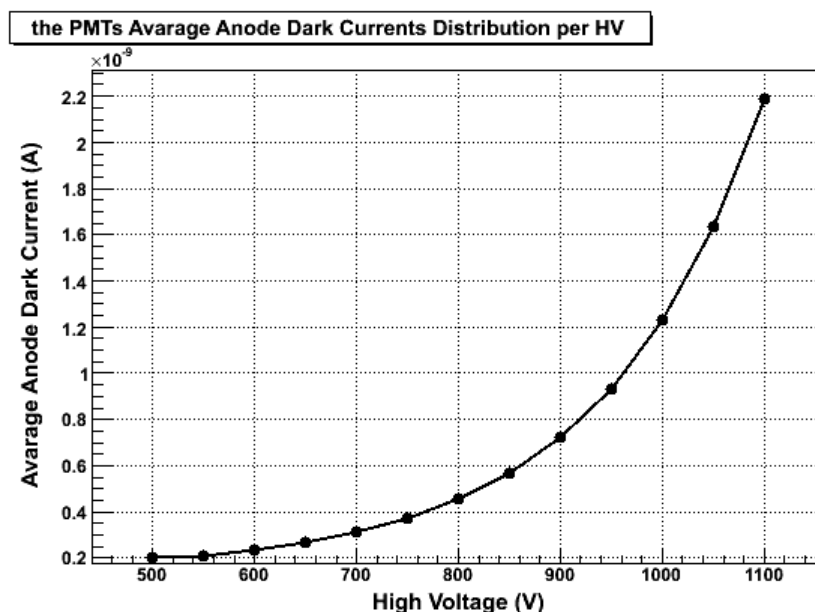


Figure 2.22. Average anode dark current values of all PMTs as a function of each HV.

PMTs were fed by high voltage (~ 750 V) in the dark box for approximately 30 minutes then anode dark current was measured. Average anode dark current values of all the PMTs as a function of each high voltages are given in figure 2.22. Anode dark current increases with an increasing high voltage, but the rate of increase is not linear. Anode dark current values of all the PMTs at 1 kV are given in figure 2.23. The average value of anode dark current at 1 kV was measured as 1.23 nA. The dark current values of all the PMTs are less than 20 nA at 1 kV which is given by Hamamatsu.

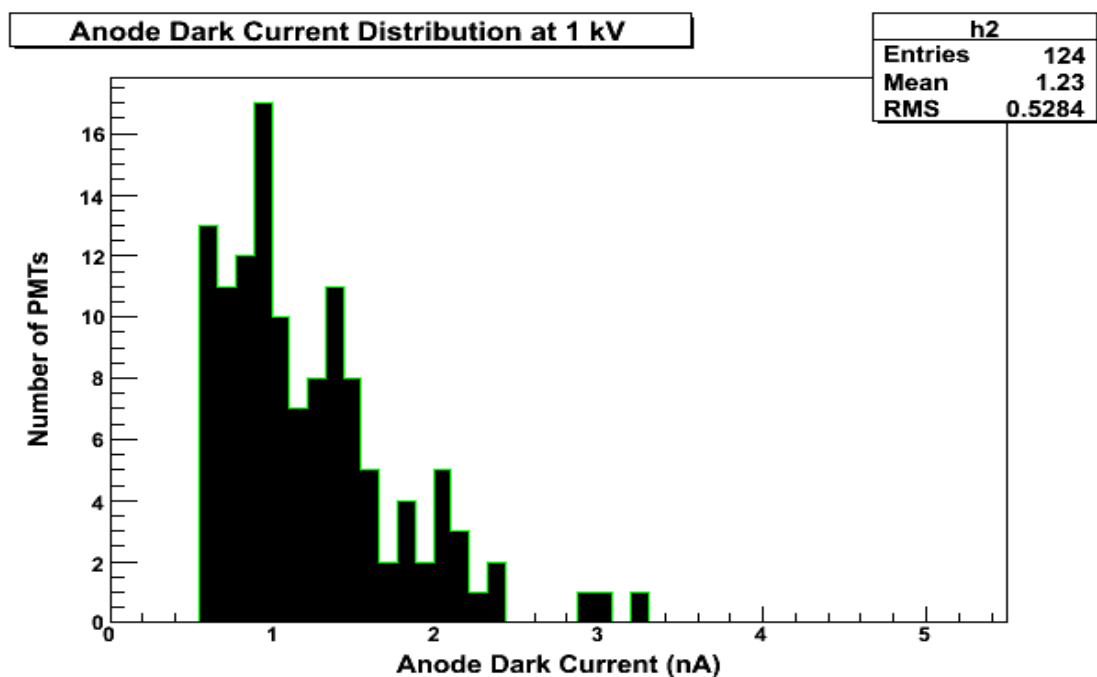


Figure 2.23. Anode dark current values of all the PMTs at 1 kV.

To measure the anode current, a halogen tungsten lamp, supplied by 10 volts, was used as the light source. A green filter was put in front of the light source to stabilize the system. There was another filter (NDF, factor = 4) after the green filter which had a $1/10^4$ factor to absorb the light. We need to use the NDF in order not to saturate the PMTs. Average anode current values of all the PMTs as a function of each HV are given in figure 2.24. Anode current increases with an increasing high voltage, but the rate of increase is not linear. And anode current values of all the PMTs at 1 kV are given in figure 2.25. The average value of anode current at 1 kV was measured to be 1.277×10^{-5} A.

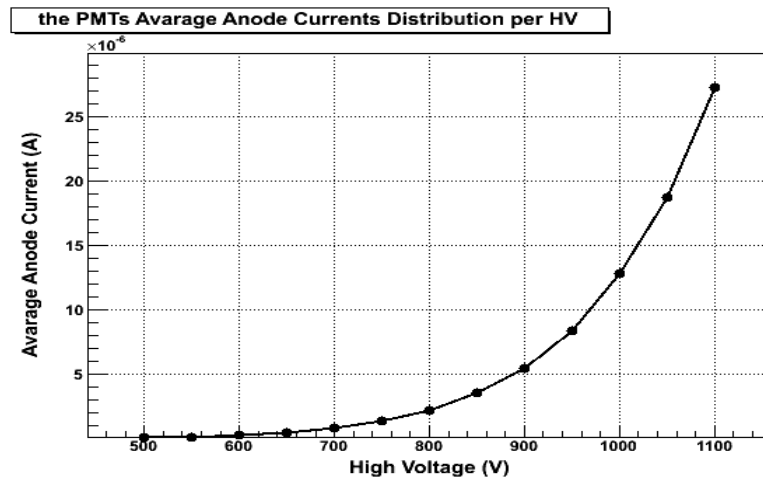


Figure 2.24. Average anode current values of all the PMTs as a function of each HV.

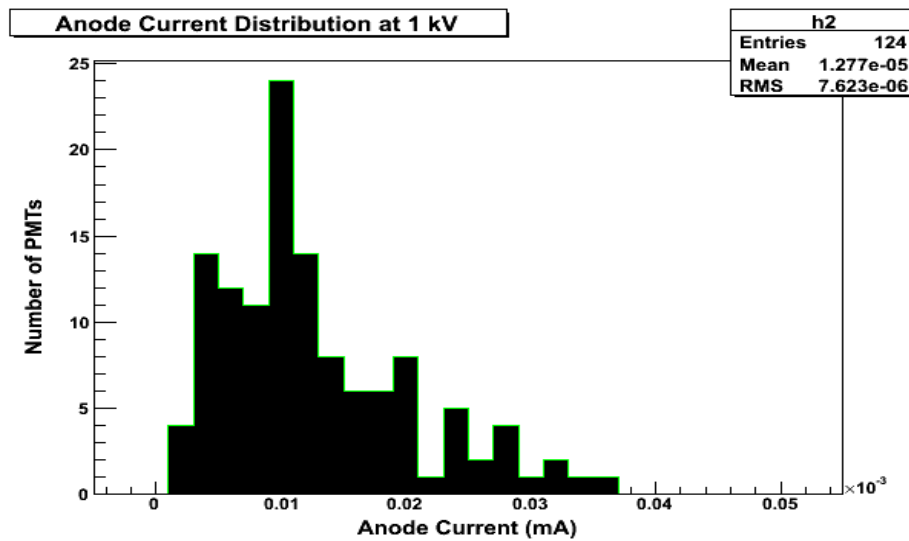


Figure 2.25. Anode current values of all the PMTs at 1 kV.

2.3.1.2. The Measurement of the Cathode Current of the PMTs

In order to study the cathode current of all the PMTs, the PMTs were fed by high voltage from 115.5 Volt to 254.1 Volt in 11.55 Volt steps. For this process, the cathode base was used.

To measure the cathode current, halogen tungsten lamp, supplied by 10 volts, was used as the light source. A green filter was put in front of the light source. NDF was not used for this process. Cathode current values of all the PMTs as a function of HV

are given in figure 2.26. There is a fluctuation on cathode current in high voltages, but the rate of the fluctuation is not so big on the cathode current. Cathode current values of all the PMTs at 232 volts are given in figure 2.27. The average value of the cathode current at 232 volts was measured to be 64.89×10^{-9} A.

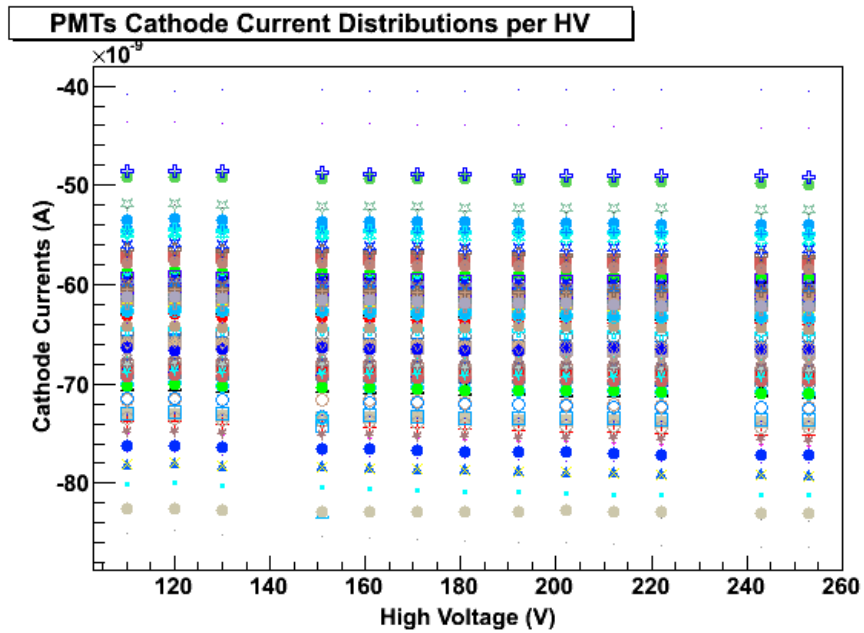


Figure 2.26. Cathode current values of all the PMTs as a function of HV.

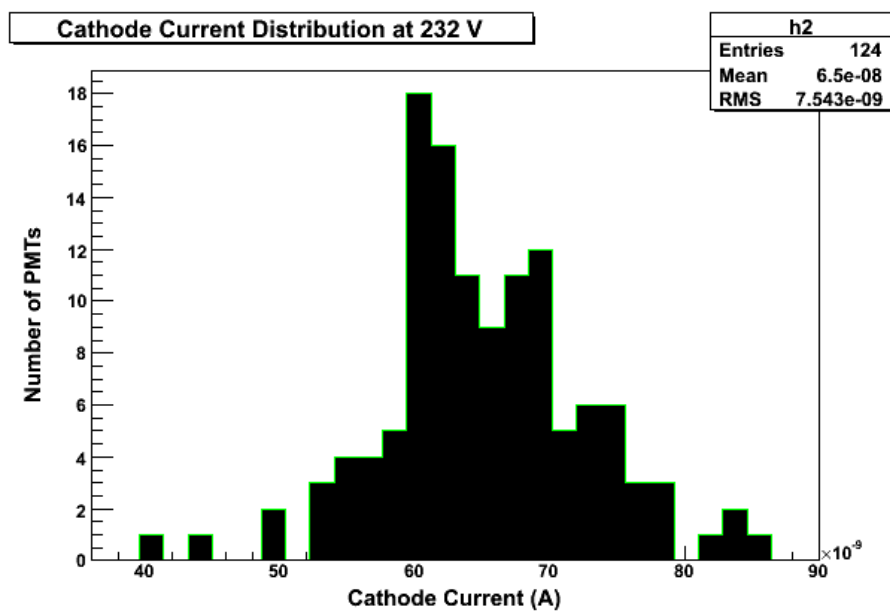


Figure 2.27. Cathode current values of all the PMTs at 232 V.

2.3.1.3. The Gain Measurement

The PMT gain is defined as the proportion of the anode current to the cathode current (more details can be found in section 2.1.1.4.1). To calculate the gain of the PMT, $G = \frac{I_a}{I_c}$ is used. In this formula, I_a is the anode current and I_c is the cathode current. To find the real value of G , we have to multiply G by 10^4 because of the NDF factor. The gain increases quickly with the applied voltage and changes with temperature, incident-light wavelength, and mean anode current (Akgun, 2002).

Average gain values of all the PMTs as a function of each HV are given in figure 2.28. Gain values of all the PMTs at 1 kV are given in figure 2.29. The average value of the gain at 1 kV was measured to be approximately 1.949×10^6 for all the PMTs.

The measurements were repeated several times and the results obtained were consistent.

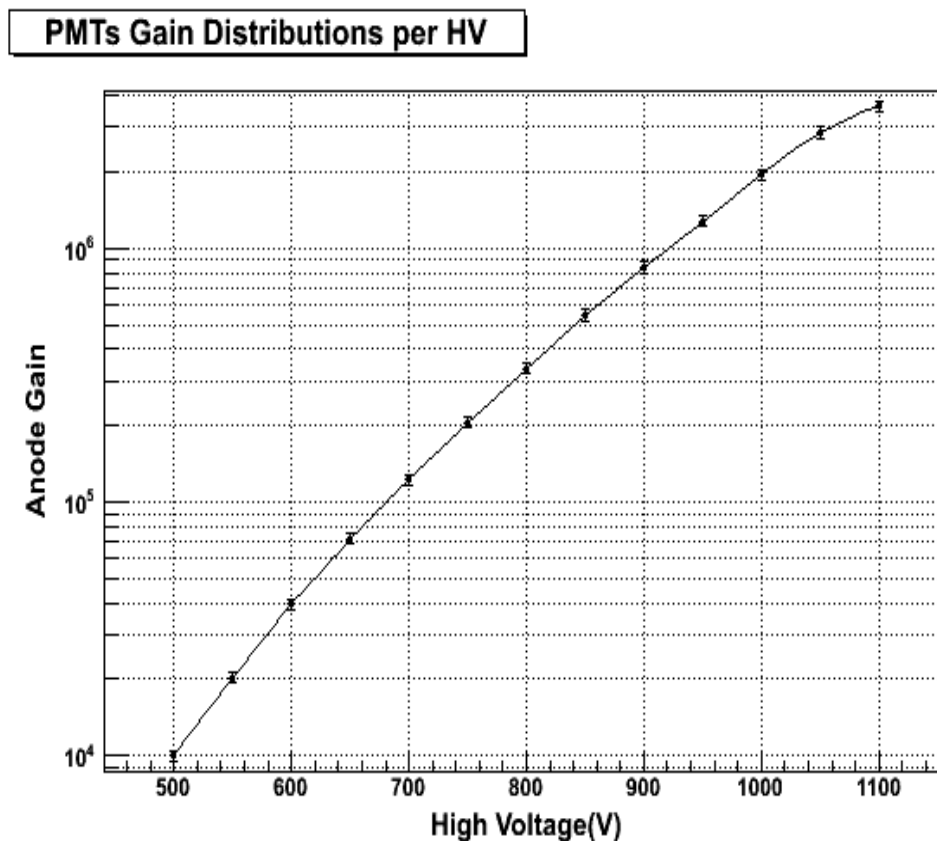


Figure 2.28. The average gain measurements of all the PMTs as a function of HV.

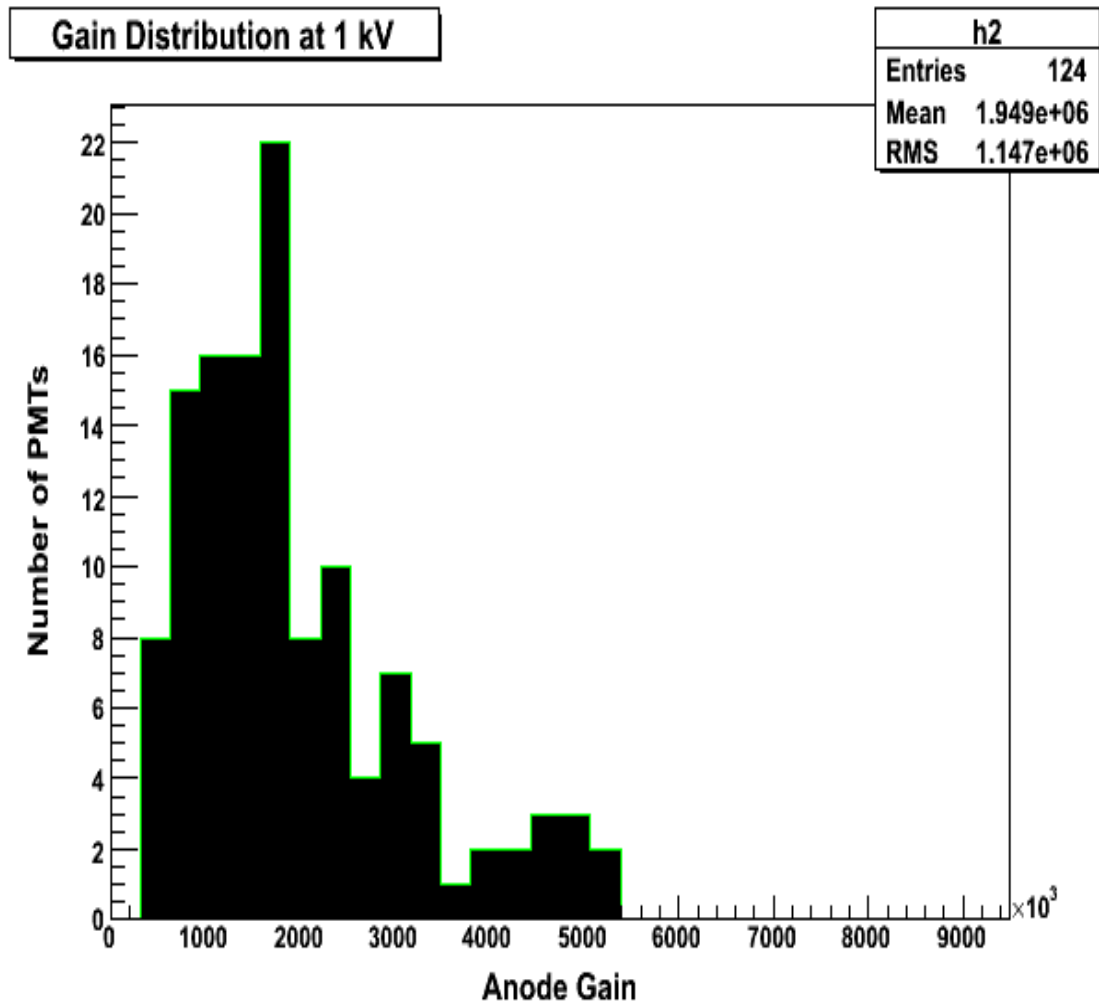


Figure 2.29. Gain current values of all the PMTs at 1 kV.

2.3.1.4. The Measurements of the Linearity of the PMTs

Only some of the PMTs linearity properties were studied because of the limited time. The details of the subject can be found in section 2.1.1.6. The halogen tungsten lamp, supplied by different values between 7-10 volts, was used as the light source. The incident light is very important for the study of the linearity. In order to control the light, several NDFs were used from a factor of 3 to 7.5 in steps of 0.5 factors. The PMTs were fed by different high voltage values (700 - 900 Volt) to obtain very high and very low anode currents. For this process, the anode base was used.

Anode current decreases when incident light decreases. As a result, anode current is linear with the incident light. It can be seen in figure 2.30.

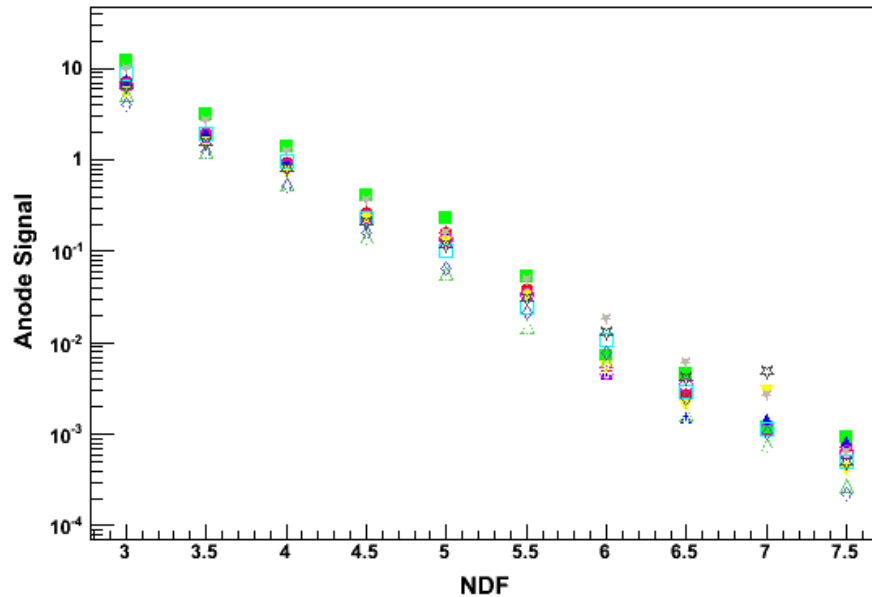


Figure 2.30. Anode signals of the candidate PMTs as a function of NDF.

2.3.1.5. The Measurements of the Collection Efficiency of the PMTs

Only some of the PMTs collection efficiency properties were studied because of the limited time. The details of the subject can be found in chapter 2.1.1.7. The halogen tungsten lamp, supplied by a fixed potential value, was used as a light source.

In order to study PMTs collect efficiency, the PMTs were fed by different high voltages (0.0 – 0.025 – 0.05 – 0.1 – 0.2 – 0.3 – 0.5 – 0.75 – 1.0 – 1.5 – 2.0 – 2.5 – 3.0 – 4.0 – 5.0 – 5.5 – 6.0 – 7.5 – 8.0 – 9.0 – 10.0 – 11.0 – 12.5 – 15.0 – 17.5 – 20.0 – 22.5 – 25.0 – 27.5 – 30.0 – 32.5 – 39.0 – 49.0 – 59.0 – 69.0 – 79.0 – 90.0 – 100.0 – 110.0 – 120.0 – 130.0 – 141.0 – 151.0 Volt). For this process, the cathode base was used. Cathode current with respect to HV can be seen in figure 2.31.

2.3.2. The Measurements Done in Timing Box

For the smooth operation of the calorimeter, well defined time response of the PMT's is crucial. In order to get successive collisions which are going to occur in 25 ns intervals at the LHC, the resulting time response of PMTs must be less than this time interval.

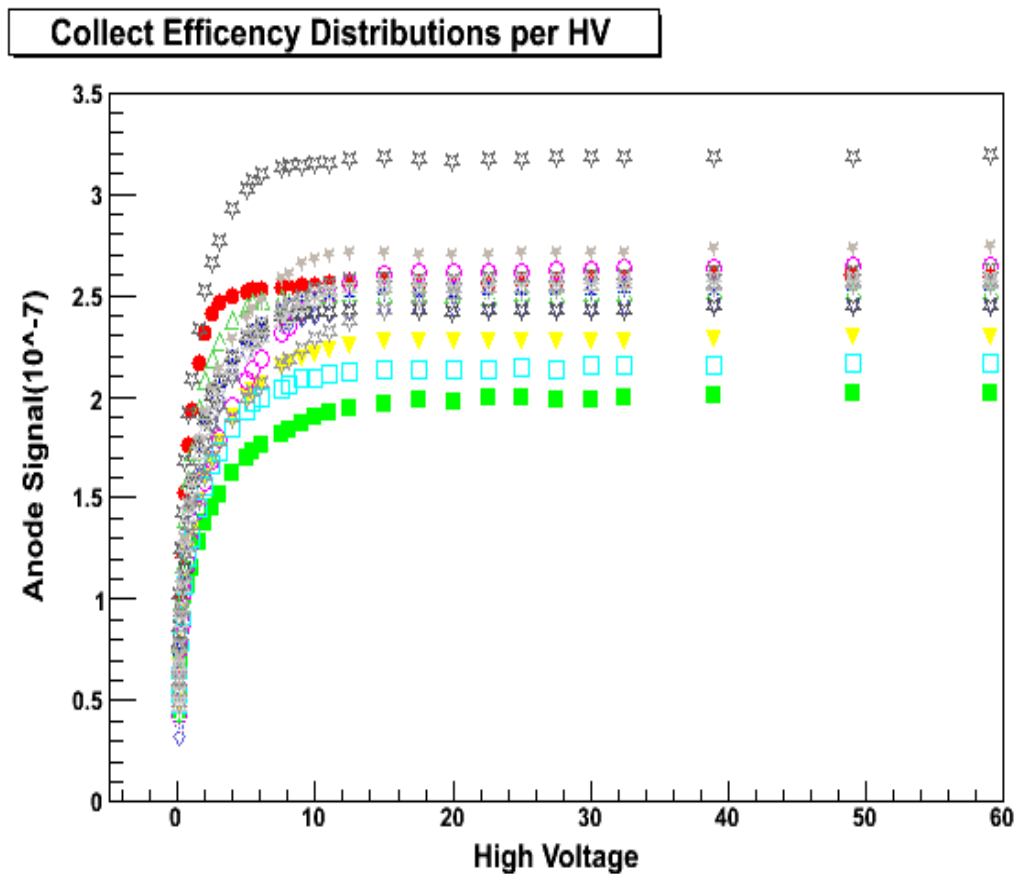


Figure 2.31. Cathode signals of the applied PMTs as a function of HV.

The measurements were performed in the time box, as explained in chapter 2.2.3. PMTs were tested one by one. PMTs were fed by high voltage from 500 V to 1000 V in 50 V steps. In these measurements, the anode base and laser as a light source were used. Then signals came to the LeCroy oscilloscope which has two channels, so called C1 and C2. The signals which came from PMTs went to C2. The signals which came from the PIN diode were used as a trigger and went to C1. With the help of the interface programme of the oscilloscope, we could take transit time, fall time, rise time, transit time spread, pulse width, amplitude and area. Data is taken in the single sample mode by the oscilloscope. About 100 signals are acquired and then the averages are calculated by an internal program of the oscilloscope. The oscilloscope does all these measurements automatically. The screenshot (Figure 2.32) of the each HV step was saved and then we obtained the data from the screenshot.

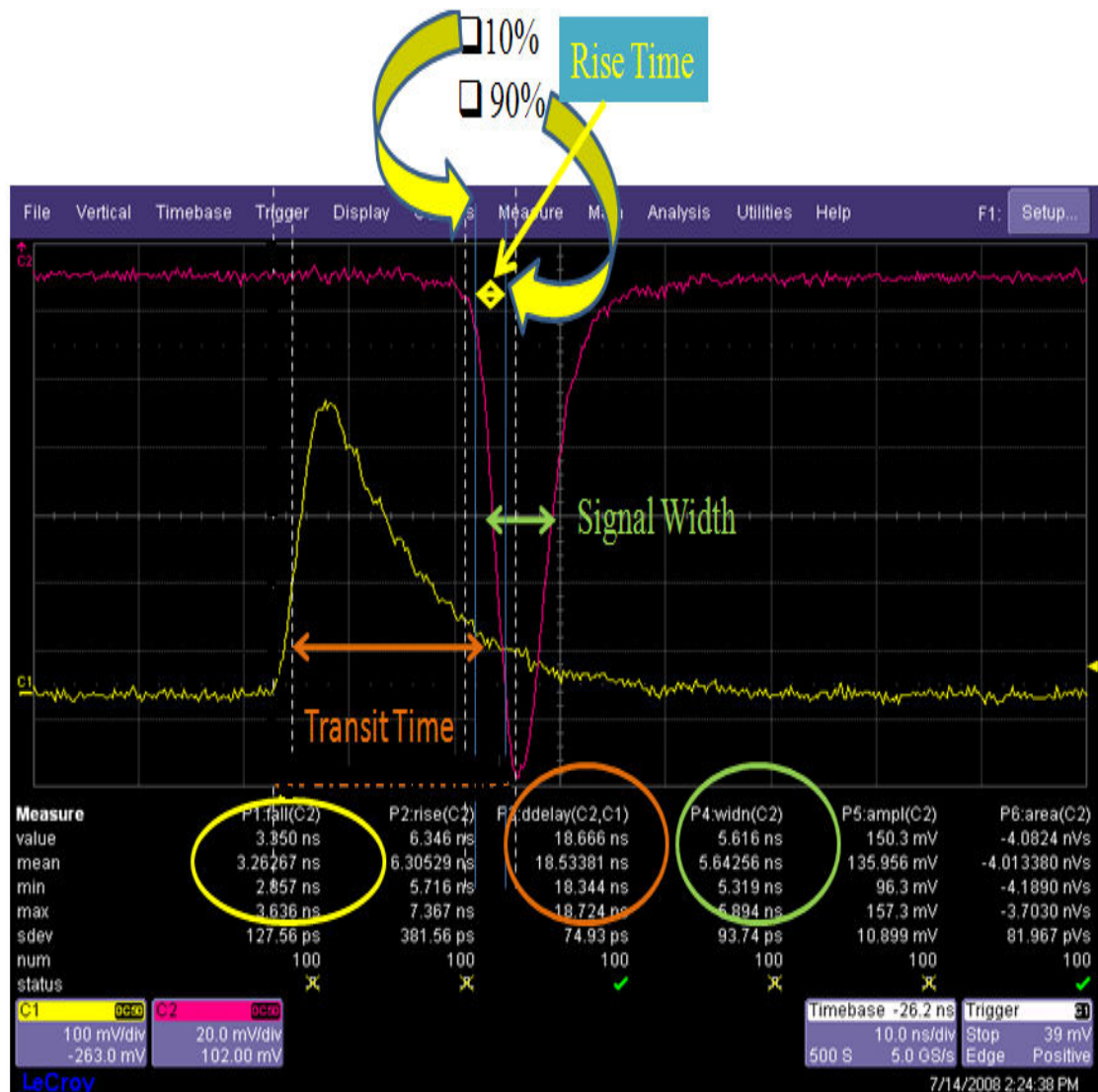


Figure 2.32. Screenshot of the oscilloscope.

2.3.2.1. The Analysis of the PMTs Rise Time

Rise time, defined in chapter 2.1.1.8, is the time interval when the signal increases from 10% to 90% of its maximum amplitude.

Since the signal is negative, fall was saved as the rise time, given in figure 2.32. Average rise time values of all the PMTs as a function of each high voltage are given in figure 2.33. And the rise time values of all the PMTs at 1 kV are given in figure 2.34. The average value of the rise time at 1 kV was measured to be 2.48 ns.

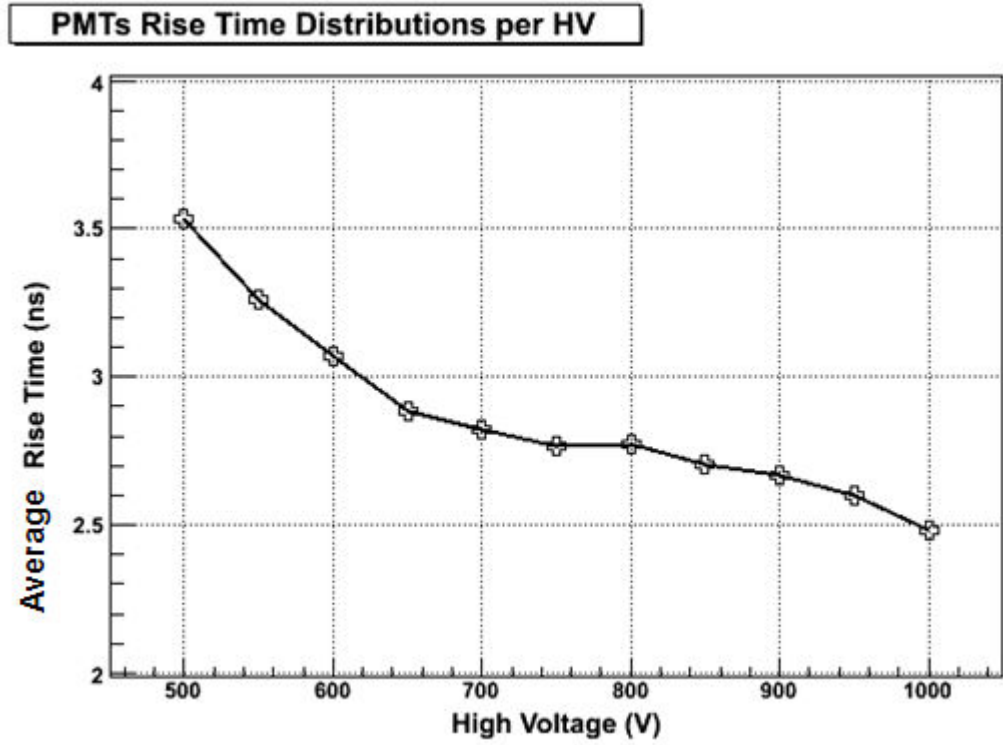


Figure 2.33. Average rise time values of all the PMTs as a function of each HV.

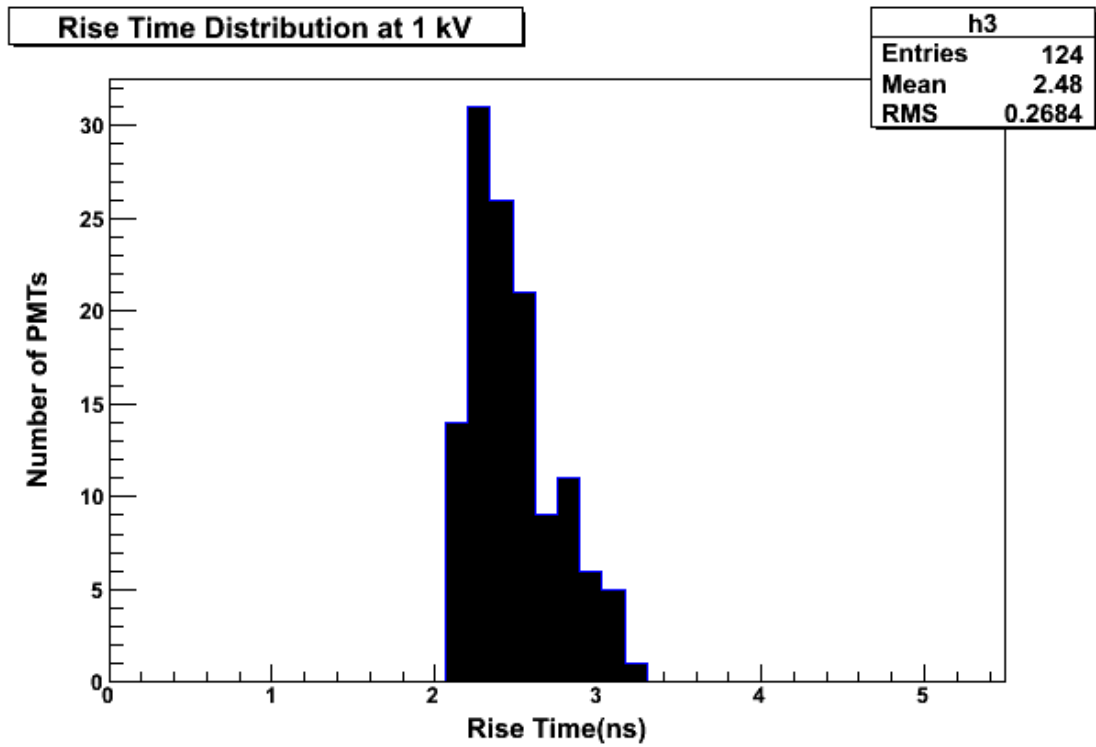


Figure 2.34. Rise time values of all the PMTs at 1 kV.

2.3.2.2. The Analysis of the PMTs Pulse Width

The pulse width is defined as the full width at half maximum (FWHM). Average pulse width values of all the PMTs as a function of each high voltages are given in figure 2.35. And pulse width values of all the PMTs at 1 kV are given in figure 2.36. The average value of pulse width at 1 kV was measured to be 6.008 ns.

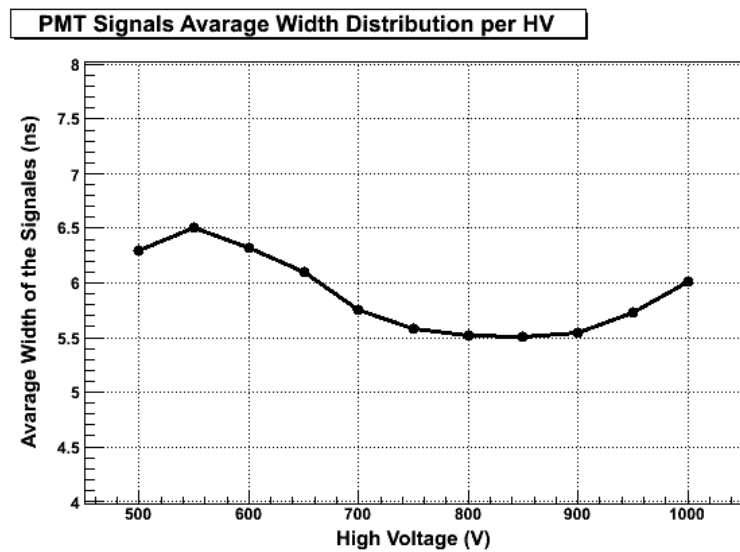


Figure 2.35. Average pulse width values of all the PMTs as a function of each HV.

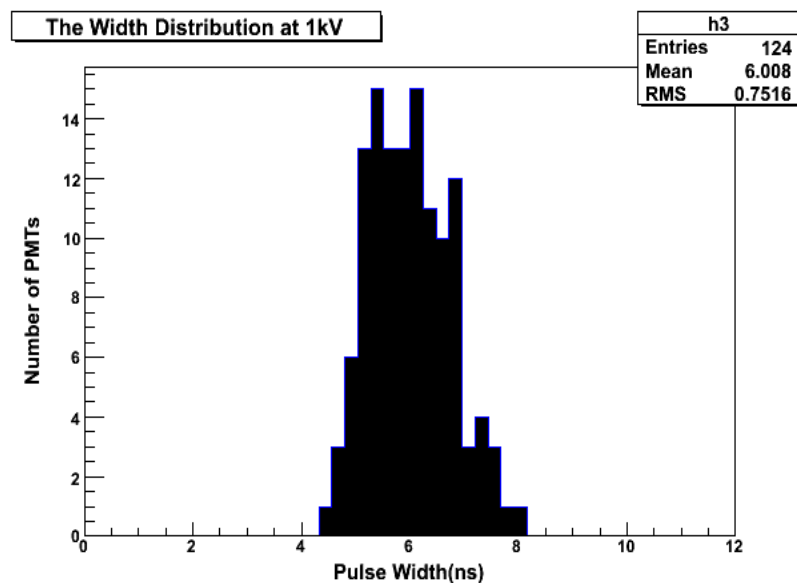


Figure 2.36. Pulse width values of all the PMTs at 1 kV.

2.3.2.3. The Analysis of the PMTs Transit Time

The meaning of the transit time is the time difference between the PIN diode signal and the PMT signal when both of them reach their half maximum of the peak values successively.

That is, the transit time is the travel time of the photoelectrons, emitted by incident light in the cathode, from the photocathode to the anode via the dynodes.

Average transit time values of all the PMTs as a function of each HV are given in figure 2.37. As it can be seen from the figure, transit time depends on the voltage applied to the PMT. When PMT is fed by the highest voltage, the lowest transit time is obtained. The transit time values of all the PMTs at 1 kV are given in figure 2.38. The average value of the transit time at 1 kV was measured to be 13.72 ns.

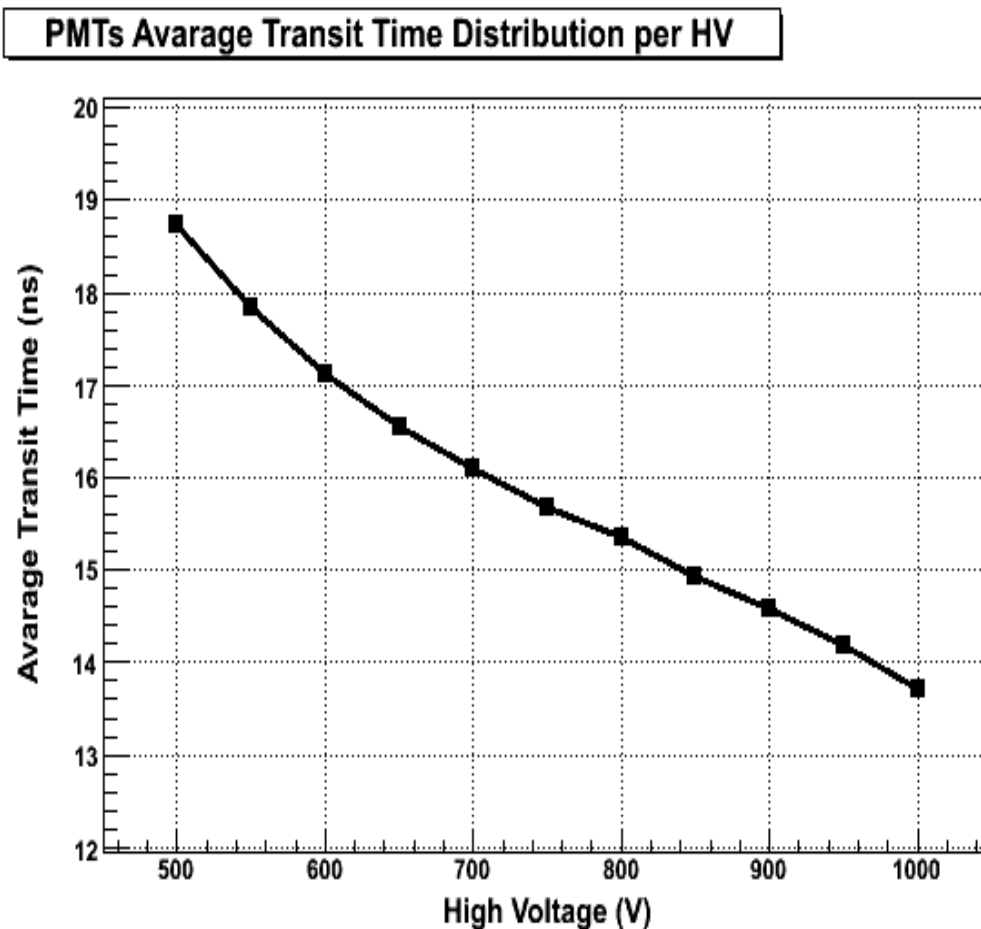


Figure 2.37. Average transit times of all the PMTs as a function of each HV.

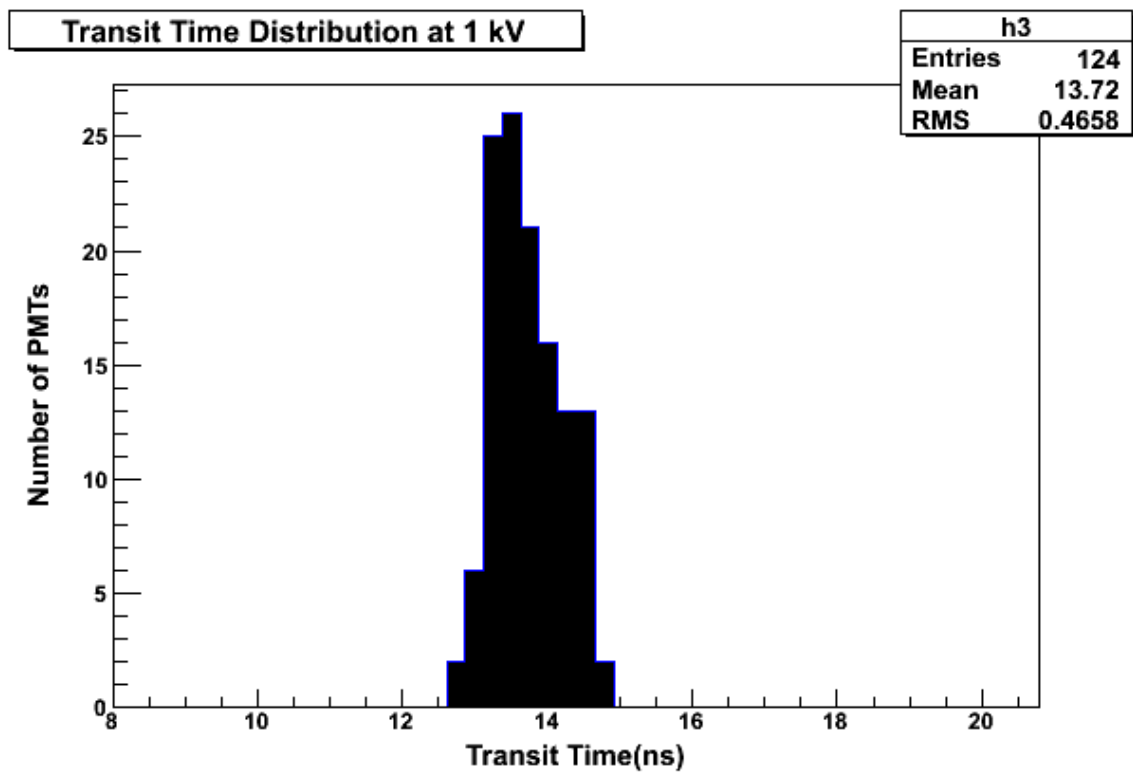


Figure 2.38. Transit time values of all the PMTs at 1 kV.

The total detection time of a signal can be the sum of the transit time (13.72 ns in average) and the pulse width (6.008 ns in average). If the detection time is smaller than 25 ns, it means it is a good device for CASTOR. As a result of this study, the average value of the detection time at 1 kV was measured to be 19.728 ns. The highest value of the detection time is 22.232 ns which belong to the PMT with serial number BA0975. So, Hamamatsu R7378A type of the PMT is suitable for CASTOR studies.

3. CASTOR TEST BEAM 2008

The test beam environment and the analysis results of the CASTOR prototype test beam data which is collected at CERN in the summer of 2008 will be described in this chapter.

3.1. Environment of the Test Beam Area

Basically, environment of the test beam area which is used in this study is going to be presented in this section.

3.1.1. The Super Proton Synchrotron (SPS)

The Super Proton Synchrotron (SPS), which has been working since 1976 and can be seen schematically in figure 1.2, is a 6.9 km long particle accelerator at CERN. Antiprotons, electrons and positrons (for use as the injector for CERN's electron-positron collider (LEP)) and heavy ions were used to be accelerated by the SPS. The SPS is currently used as the final pre-injector for high-intensity proton beams for CERN's LHC, accelerating protons from 26 GeV to 450 GeV (Super Proton Synchrotron, http://en.wikipedia.org/wiki/Super_Proton_Synchrotron). In the continuation of the ongoing fixed target research program, SPS is used to provide 400 GeV proton beams for a number of active fixed-target experiments such as NA48 and NA61/SHINE in North Experimental Area of CERN. CASTOR prototype was exposed to a secondary beam in summer of 2008 in North Experimental Area. There were approximately 10^{12} protons per burst (Introduction to the H2 beam, <http://ab-div-atb-ea.web.cern.ch/ab-div-atb-ea/BeamsAndAreas/h2/H2manual.html>).

3.1.2. North Experimental Area (NEA) at the SPS

The primary proton (400 GeV/c) beam of the SPS may be taken out from the long straight section (LSS2) to the NEA. The extracted beams which are carried by surrounding bending magnets and beam-splitting system and focusing elements over a number of hundreds of meters are separated into three beam channels each ending in a

target (T2, T4, T6) where the secondary particle beams are produced (Figure 3.1), close to the surface but deep enough to be shielded by the landscape around them. Secondary beams that are produced by targets 'T2' and 'T4' are for the Experimental Hall North 1 (EHN1) (SPS Primary Targets, https://twiki.cern.ch/twiki/bin/view/ABATBEA/SPSPPrimaryTargets#T2_%20Wobble).

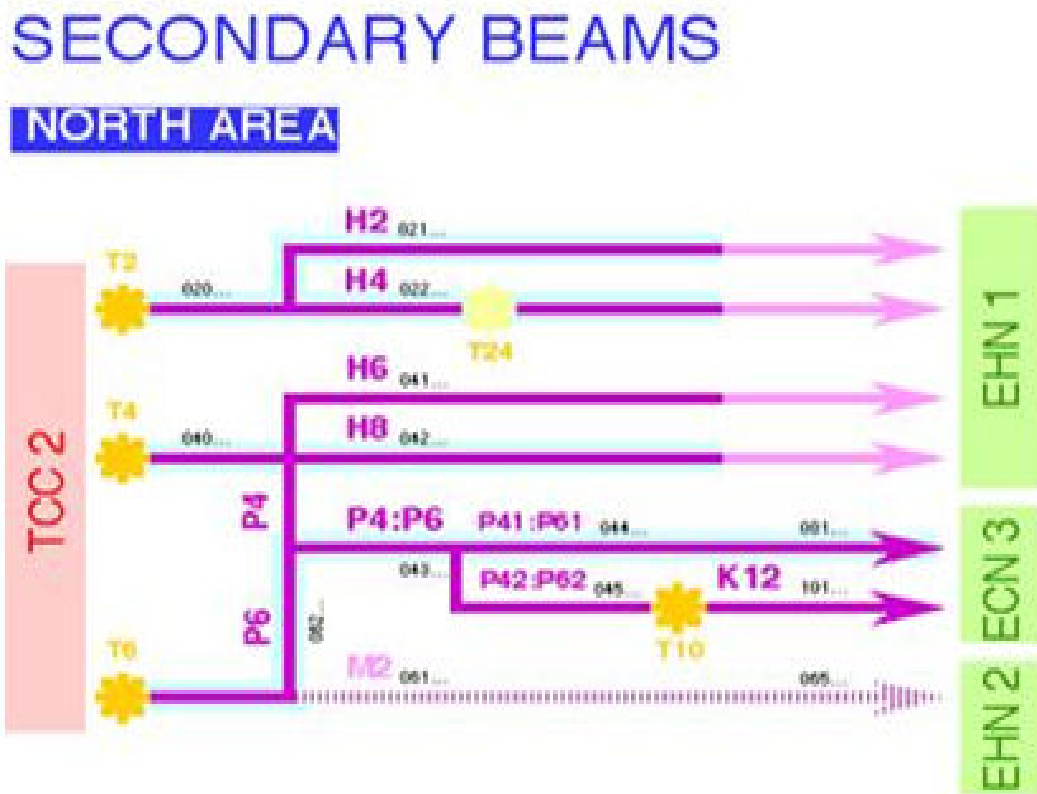


Figure 3.1. Layout of the North Area (<http://nahandbook.web.cern.ch/nahandbook/default/common/software/Beatch.htm>).

Design of all target stations of NEA are alike. In every station, there are several targets, made of mostly beryllium ($500 \times 160 \times 2 \text{ mm}^3$) or lead, of different lengths and cross-sections that are mounted on a common support, which the CERN Control Centre (CCC) control room may move so that the target can be selected and its position in the beam can be adjusted (SPS Primary Targets, https://twiki.cern.ch/twiki/bin/view/ABATBEA/SPSPPrimaryTargets#T2_Wobble). The beam information can be read from the so-called 'PAGE-1' TV screens in the electronics cabins and control rooms (Figure 3.2).

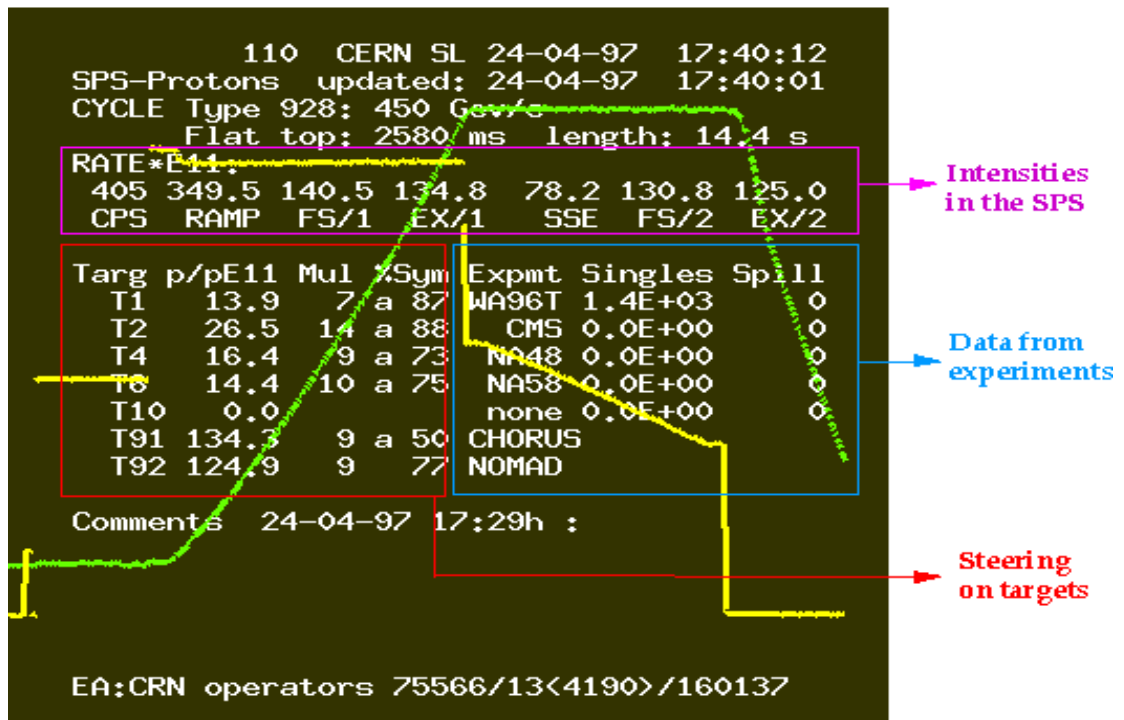


Figure 3.2. 'PAGE-1' TV screen in the experimental huts (<http://sl.web.cern.ch/SL/eagroup/Page-1.html>).

A massive iron shield (TAX), in which holes have been penetrated for the passage of primary and secondary beams, encircles the assembly completely. The incident proton flux can be seen by a beam monitor (Figure 3.2) station upstream of the target and horizontal and vertical split-foil detectors (Collimator) serve to focus the beam on the target.

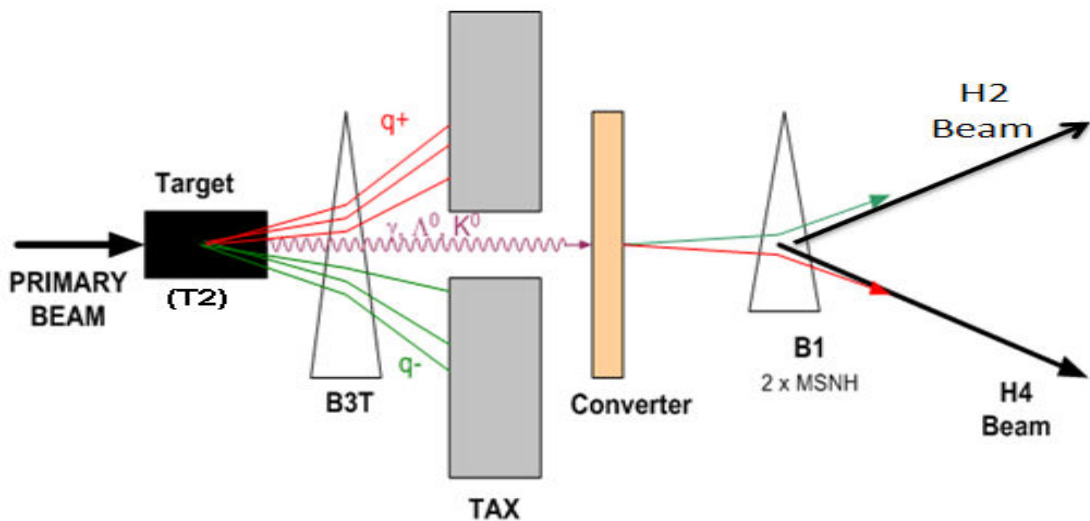


Figure 3.3. Upstream of the H2 beam line.

Beam can be headed by bending magnets. The cross-sectional profile of the beam incident on the target can be measured by a mini-scanner located before the target. The emerging particle flux is detected by a second beam monitor downstream from the target stations. It can be seen in figure 3.3. There are two derivated secondary beams called the H2 and H4 beams to EHN1 from the T2 target and thanks to the T2 wobbling station (Introduction to the H2 beam, <http://ab-div-atb-ea.web.cern.ch/ab-div-atb-ea/BeamsAndAreas/h2/H2manual.html>).

3.1.3. The H2 Beam Line

Hadrons, electrons or muons of energies between 10 and 350 GeV/c, as well as 400 GeV/c (primary) protons are provided by a secondary particle beam (also 1-9 GeV tertiary particle) called the H2 beam line. The H2 beam line is a member of the T2 target at NEA (EHN1, building 887) (Introduction to the H2 beam, <http://ab-div-atb-ea.web.cern.ch/ab-div-atb-ea/BeamsAndAreas/h2/H2manual.html>). Target T2 is approximately 590 m far from the prototype. To produce the tertiary particles, there is another target which is called T22, placed approximately 97 m upstream from the prototype.

Several characteristics of the H2 beam line are given in table 3.1.

Table 3.1. Several features of the H2 beam line (Introduction to the H2 beam, <http://ab-div-atb-ea.web.cern.ch/ab-div-atb-ea/BeamsAndAreas/h2/H2manual.html>).

Some Main Parameters of H2	
Maximum momentum	360 GeV/c 450 GeV/c for primary protons
Acceptance	$\pm 1.5 \mu\text{sr}$ ($2.5 \mu\text{sr}$ at $p < 200\text{GeV}/c$)
Maximum $\Delta p/p$	$\pm 2\%$
Intrinsic $\Delta p/p$ with slit = 0	$\sim 0.05\%$
Height of beam in EHN1:	2460 mm
Length of beam	615 m

3.1.3.2. Using Several Detectors in the H2 Beam Line

There are several detectors which the H2 beam line is equipped with. The layout of the H2 detectors can be seen in figure 3.5.

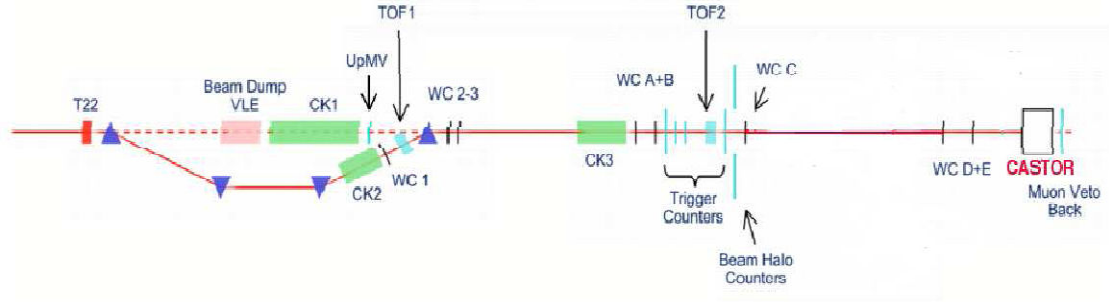


Figure 3.5. Layout of the H2 detectors in NEA.

Cerenkov counters (CK): There are two Cerenkov counters in the beam line. One of which is in the High Energy part. The second one is in the very low energy part. They are used to identify the particles. According to the momentum range used, they can be filled by helium and nitrogen.

Time of Flight Detector (TOF): TOF detector is a detector which is able to separate a lighter and a heavier fundamental particle of the same momentum using their time of flight between at least two scintillators. The first of the scintillators makes a clock active upon being struck and the other one stops the clock upon being struck. When the two masses are indicated by m_1 and m_2 and have velocities v_1 and v_2 , the time of flight difference is as follows (Time of flight detector, http://en.wikipedia.org/wiki/Time_of_flight_detector):

$$\delta t = L \left(\frac{1}{v_1} - \frac{1}{v_2} \right) \approx \frac{L_c}{2p^2} (m_1^2 - m_2^2) \quad (3.1)$$

The distance between the scintillators is shown as L . The approximation is in the relativistic limit at momentum p (c is speed of light in vacuum). Generally, the apparatus' time resolution is shown as δt (Time of flight detector, http://en.wikipedia.org/wiki/Time_of_flight_detector; Abdullin et al, 2008).

Wire Chambers (WC): There are eight WCs called WC1, WC2, WC3, WCA, WCB, WCC, WCD and WCE in H2 beam line. WCs are filled by ArCO₂ (50/50). They let us make beam profiles in two planes. They have 10×10 cm² active area within 11×11 cm² of a window (Figure 3.6). The spatial resolution is around 350 μm in both *x* and *y* coordinates. They operate properly for beam rates above 10³ particles per burst (Akchurin et al., 2007).



Figure 3.6. A view of WCs (C and D).

Scintillation (SCINT): Counters which run in a sensitive area of 100 mm diameter are used for triggering the beam. The rate between the two main magnets is counted, and many 'parasitic' particles of H₂ & H₄ are seen by SCINT01. In H₂ beam line, there are four scintillation counters (S1, S2, S3 and S4) (Figure 3.7). They were made of polystyrene scintillators of 1 cm thickness. The beam trigger typically consisted of the coincidence of the S1&S2&S4 which is approximately define a 4×4 cm² surface area (Introduction to the H₂ beam, <http://ab-div-atb-ea.web.cern.ch/ab-div-atb-ea/BeamsAndAreas/h2/H2manual.html>; Abdullin et al, 2008).

Muon Veto Counters: Muon counters (Muon Veto Front (MVF), Muon Veto Wall (MVW) and Muon Veto Back (MVB)) are used to tag the energetic muons. The MVB is a 80×80 cm² scintillation counter (Figure 3.8) (Abdullin et al, 2008).

HF Table: The CASTOR prototype is fixed stably and exposed to H₂ beam on the HF table that can move horizontally and vertically. Therefore, prototype can be focused in any direction and because of this feature we can analyze several parameters of the prototype.



Figure 3.7. A view of SCINT (S1, S2 and S4).



Figure 3.8. A view of MVB.

3.2. CASTOR Test Beams

The analysis results of the CASTOR detector test beam data collected at CERN in the summer of 2008 will be presented in this chapter.

3.2.1. Previous Beam Tests of the CASTOR Prototypes (2003-2004-2007)

Before the 2008 beam test, three prototypes (2003, 2004 and 2007) of CASTOR were studied. Only main conclusions of those studies will be given here.

Beam Tests 2003: The CASTOR test beam was studied at first for the Cherenkov light transmission efficiency of different types of air-core light guides, and also an analysis of the calorimeter linearity and resolution as a function of energy and impact-point, obtained with 20 - 200 GeV electron beams from CERN/SPS tests was performed. Only an EM section with several combinations of the calorimeter such as different combinations of structures for the active material of the calorimeter (quartz plates and fibres), different light-guide reflecting materials (glass and foil reflectors) and photodetector devices (photomultipliers and avalanche photodiodes) have been tested and compared (Aslanoglou et al., 2008).

To summarize the study, equipping the CASTOR calorimeter with quartz-plates as the active material, APDs as photodetector devices, and light-guides with foil reflector were suggested as a promising option (Aslanoglou et al., 2008).

Beam Tests 2004: The second prototype of CASTOR, was the first to test the hadronic part together with the electromagnetic part of the detector and its design was very close to the final design of the detector, consisting of quartz plates, air-core light-guides, equipped with Dupont (AlO+SiO₂+TiO₂) reflective foil, and avalanche photodiodes (APDs) as well as photomultiplier tubes (PMTs). The responses of the calorimeter using two different types of photodetectors (APDs, PMTs) were compared, the energy linearity and resolution were studied, as well as the spatial resolution of the prototype to electromagnetic and hadronic showers were studied with $E = 20 - 200$ GeV electrons, $E = 20 - 350$ GeV pions, and $E = 50, 150$ GeV muons from the CERN/SPS (Aslanoglou et al., 2007).

Beam Tests 2007: The third prototype of CASTOR used quartz plates which were taken from the original DELPHI experiment and air-core light-guides which were equipped with reflective foil. Two different types of photodetectors the Hamamatsu R5380Q and RIE FEU187 PMTs were used to compare the responses of the calorimeter. The energy linearity and resolution, the uniformity, as well as the spatial resolution of the prototype to electromagnetic and hadronic showers were studied with $E = 10 - 200$ GeV electrons, $E = 20 - 350$ GeV pions, and $E = 50 - 150$ GeV muons in beam tests

which were carried out in the H2 line at SPS during two weeks in 2007 (Aslanoglou et al., 2008).

3.2.2. The CASTOR Test Beam 2008 Analysis

The fourth prototype of CASTOR contains a full-length octant, containing the electromagnetic and hadronic sections, with a total of 28 readout-units (Figure 3.9). It was constructed with successive layers of tungsten plates as absorber, and fused silica quartz plates as active medium, air-core light-guides, equipped with reflective foil, and two different types of photodetectors the Hamamatsu R5380Q and RIE FEU187 PMTs were used to compare the responses of the calorimeter. More detailed information about the materials used can be seen in chapter 1.3.2.

The CASTOR Test Beam 2008 (TB08) was scheduled from 12 June to 26 June 2008. In order to test several characteristics of the EM and HAD parts of the prototype, the uniformity, the energy linearity, the energy resolution and the spatial resolution, different type of beam particles such as electrons from 10 to 200 GeV, pions from 20 to 350 GeV and muons from 150 to 300 GeV were used. Also to study very low energies (VLE) response, electrons and pions, having energies between 1 - 9 GeV, were used.

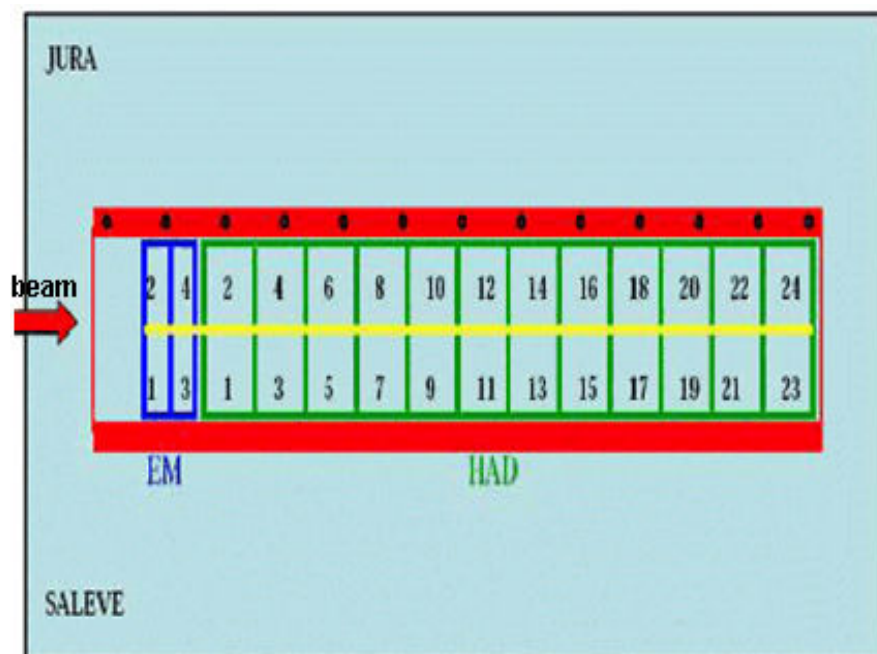


Figure 3.9. Schematic view of the CASTOR prototype IV (Aslanoglou et al., 2008).

3.2.2.1. Front-End Detectors on the Prototype in H2 Beam Line

It is crucially important to know the exact behavior of the beam. Scintillation (SCINT) counters are used to understand whether there is a real beam or not. If there is a real beam, the data from SCINT counters will be used as trigger. Such information was used during data taking. There are four SCINT (S1, S2, S3 and S4) signals whose behavior we can see in figure 3.10.

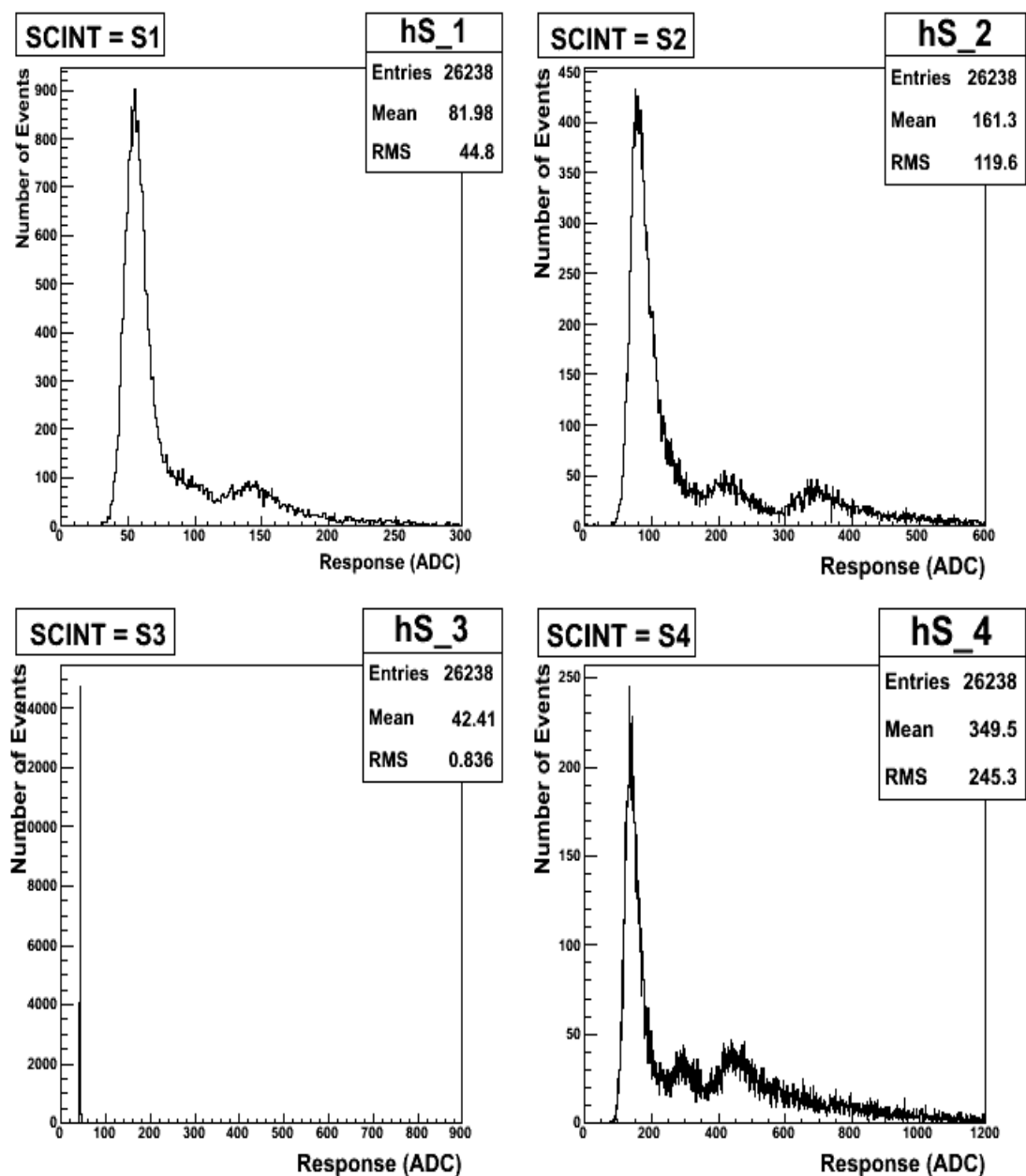


Figure 3.10. Behavior of the scintillators (S1, S2, S3 and S4).

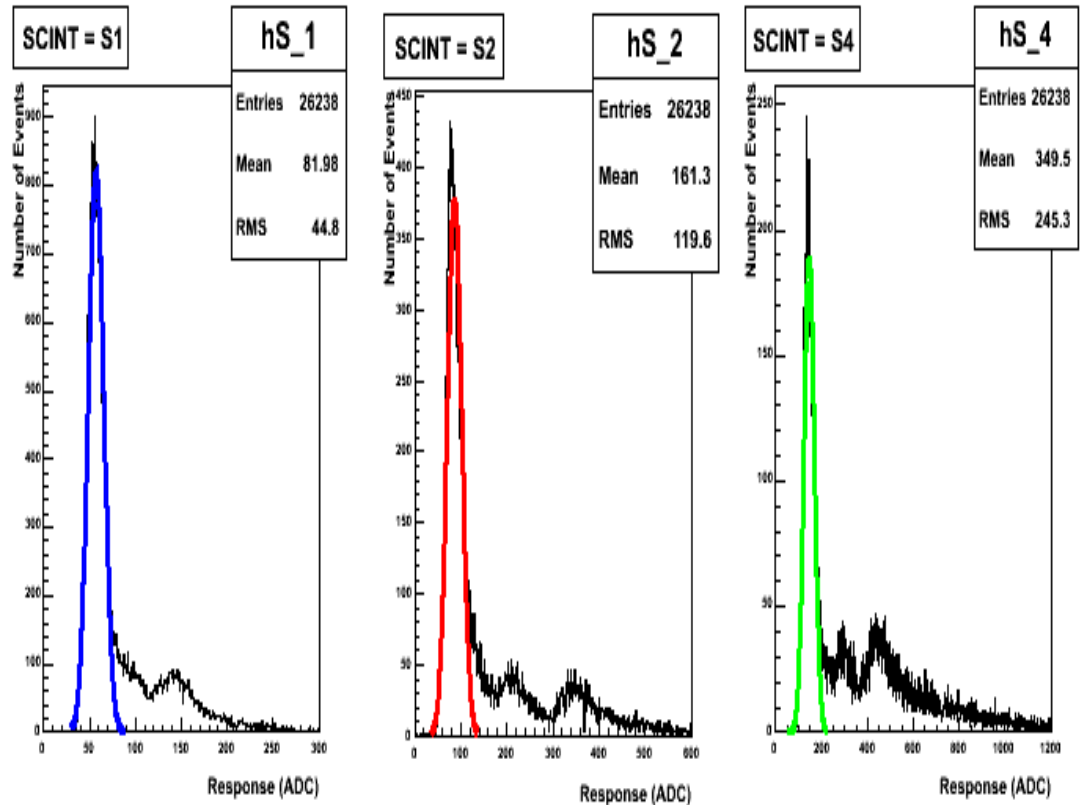


Figure 3.11. To select single hits, first peak was used around 3σ (S1 & S2 & S4).

From the figure 3.10, it can be seen that S1, S2 and S4 worked properly, however, S3 had a problem. Therefore, only S1, S2 and S4 signals were used. The beam trigger typically contains the coincidence S1 & S2 & S4, which was defined as a 4×4 cm² area on the front face of the calorimeter. In addition, they were used to select the single hits.

The S1 & S2 & S4 coincidence was used to eliminate multi-particle events off-line since it gave a clean pulse height distribution of single and multiple particles in the beam. To select events which had single hits a gauss fit was applied over the first peak ($\pm 3\sigma$) (in figure 3.11). In order to keep events around these values and to reject events which have more than one hit, SCINT (S1, S2, and S4) was used. All runs were checked for this which were used in this analysis.

Especially, for the studies of the spatial resolution (surface scan) and others we need to know the beam position. In order to clarify the beam position, WC information is very important. So, we had to know which WC worked properly. In figure 3.12, all WCs information (A, B, C, D and E) can be seen.

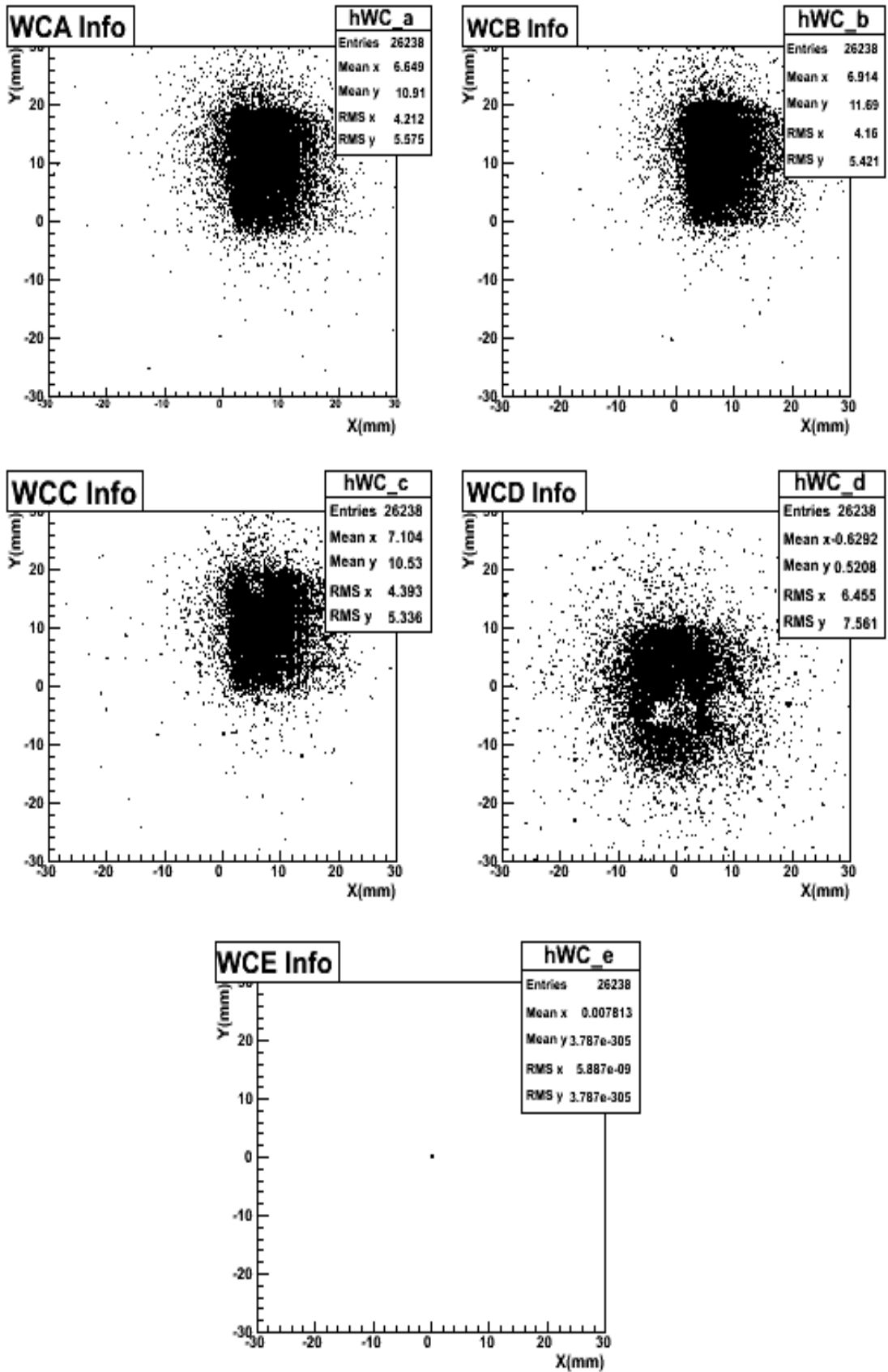


Figure 3.12. WCs (A, B, C, D and E) information in two dimensions.

The WCE is the closest to the prototype so the information of the WCE is more precise on the prototype. However, it did not work in some runs. So we had to find out which WCs worked fine and clarify the best one. All runs were checked for this which were used in this analysis.

To reject or keep the muons from the runs, we need to tag the muons. In order to identify muons, Muon Veto Back (MVB) detector, behind the prototype in H2 line, and SCINT information were used. First MVB information with the pedestal trigger was used and the muon peak was found and this information was used in the beam trigger to define muons. This method allowed us to tag the muons. The MVB pedestal signals can be seen in figure 3.13.

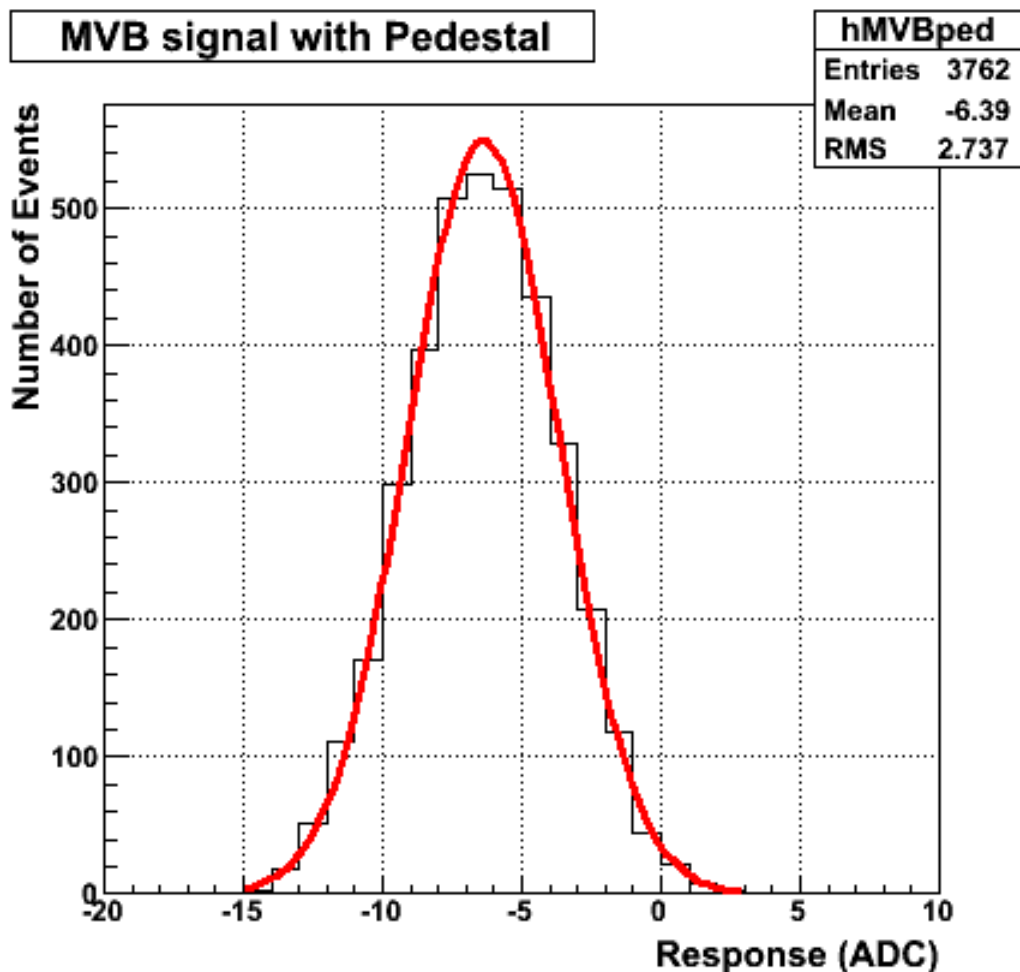


Figure 3.13. The MVB signals with pedestal trigger.

3.2.2.2. Preparation for the Analysis

Since Readout Units (RUs) of the prototype IV were not identical, we need to calibrate RUs for a good analysis. In order to calibrate the RUs, 150 GeV muons, penetrating the whole calorimeter, were used. In table 3.2, the inter calibration coefficients corresponding to the RUs used in this analysis are shown. These coefficients were calculated by other members of the collaboration using the same test beam data.

Table 3.2. The inter calibration coefficients corresponding to the RUs.

RU (Channel)	Inter-Calibration	RU (Channel)	Inter-Calibration
SALEVE	Constants	JURA	Constants
EM1	1.000000	EM2	1.545280
EM3	0.989969	EM4	1.267020
HAD1	2.116620	HAD2	1.722910
HAD3	1.929140	HAD4	1.724090
HAD5	5.277410	HAD6	1.988920
HAD7	2.782380	HAD8	1.471590
HAD9	1.740900	HAD10	2.345470
HAD11	2.442380	HAD12	6.844690
HAD13	2.506350	HAD14	1.000000
HAD15	2.907920	HAD16	1.000000
HAD17	2.028260	HAD18	1.000000
HAD19	2.358480	HAD20	1.000000
HAD21	1.427020	HAD22	---
HAD23	5.091080	HAD24	---

The pion, electron or muon beams are not purely clean in most cases. Beams are contaminated with some other particles and need to be cleaned. With this purpose, some standard cuts were applied. For instance; to clean the pion beams, MVB information was used (mentioned in section 3.2.2.1) to reject the muons from the pion beams and to reject the electrons from the pion beams, fraction electromagnetic cut was applied. The

fraction electromagnetic (fem) is the ratio of the EM sum signals to the sum of the EM+HAD signals. To clean the electron beams, MVB information was applied to reject the muons from the electron beams and fem cut was used to reject the pions from the electron beams. Also both for pion beams and electron beams, single hit events were required and to choose the single hit events, SCINT information was used as it was explained in section 3.2.2.1. Cut details are given in table 3.3.

Table 3.3. Type of cuts used to clean beams.

Type of Beam	TYPE OF CUTS			
	Single particle	Muon rejection	e^- or π rejection	Position def.
Pion	S1 & S2 & S4 (response $\mp 3\sigma$)	MVB (response $\mp \sigma$)	fem < 0.95	WCs
Electron	S1 & S2 & S4 (response $\mp 3\sigma$)	MVB (response $\mp \sigma$)	fem > 0.95	WCs

In figure 3.14, the sum of the signals of the EM part vs the sum of the signals of the HAD part is shown. In (a) the effect is shown without cuts and in (b) with cuts for pion beams (banana). In (c) the effect is shown without cuts and in (d) with cuts for electron beams.

In figure 3.15.a, the effect of each cut (on the number of entries single hit, single hit & rejection of muons and single hit & rejection of muons & rejection of electron respectively) can be seen for the pion beams and in figure 3.15.b, the effect of each cut (single hit, single hit & rejection of muons and single hit & rejection of muons & rejection of pion respectively) can be seen for electron beams.

In order to reject unwanted particles (muons, electrons) and single hits from pion beams several cuts were applied. Results of the cuts can be seen in figure 3.15 b respectively. After applied all cut remaining yellow signal belongs to pion beams and also after all cuts remaining pion events sum of HAD vs sum of EM plotted in figure 3.14 b. Both of these plots show that cuts worked fine and cleaned pion beams.

Similar cuts used for electron beams and results can be seen in figure 3.15 a and figure 3.14 d. Again both of these plots show that cuts worked fine and cleaned the electron beams.

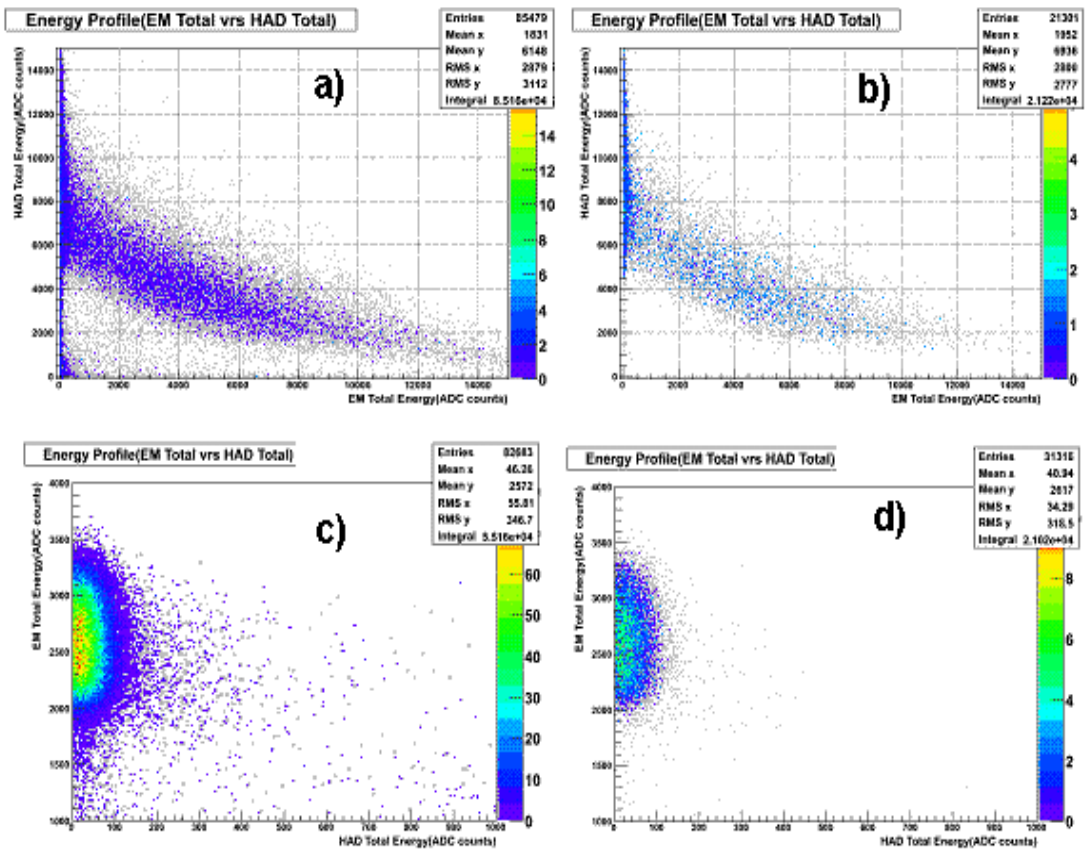


Figure 3.14. The EM signal sum vs the HAD signal sum for (a) pion beams without cuts and (b) pion beams with cuts (banana) (c) electron beams without cuts and (d) electron beams with cuts.

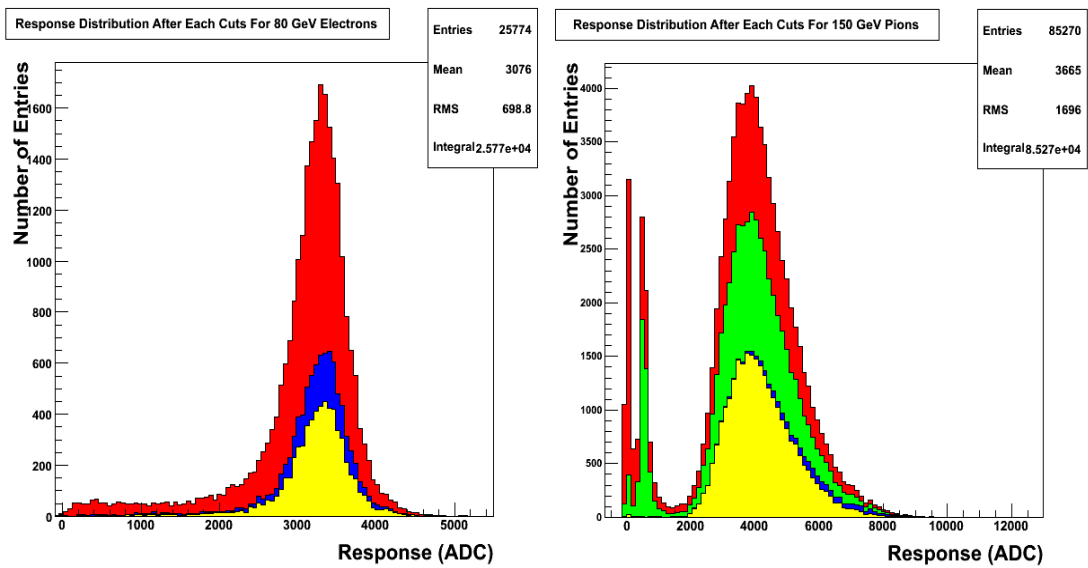


Figure 3.15. a) the effect of cuts (one over another respectively) for electron beams and b) the effect of cuts (one over another respectively) for pion beams.

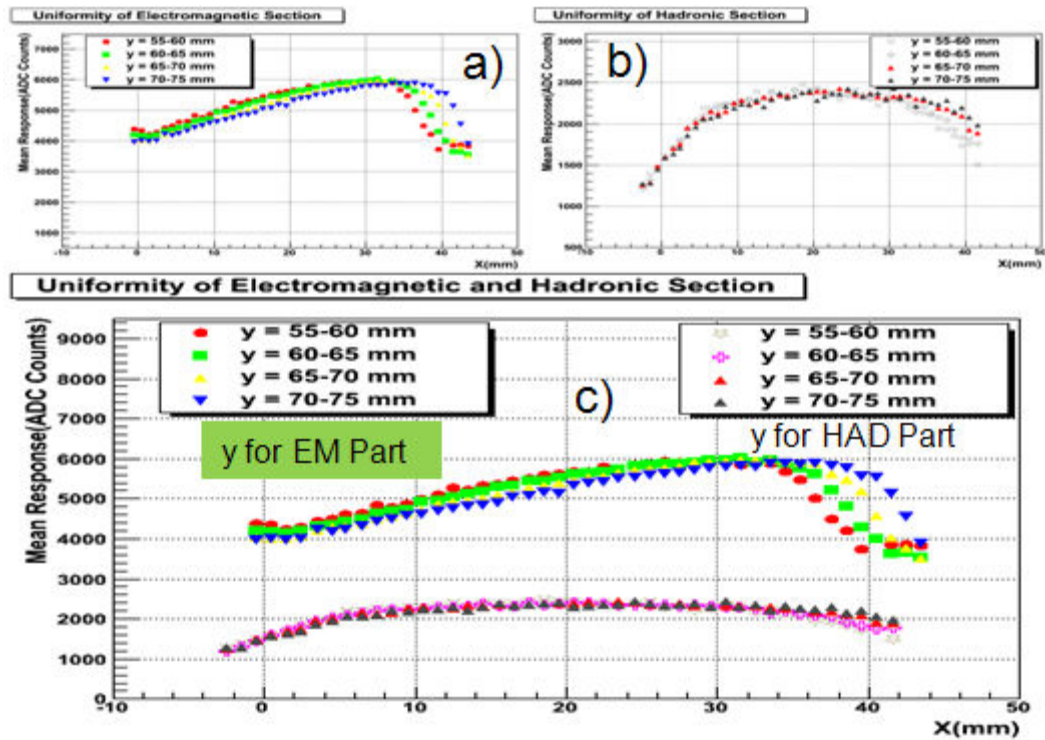


Figure 3.16. Uniformity study with different particles a) for EM section (with electrons) b) for HAD section (with pions) and c) show both EM and HAD.

The response uniformity of the prototype is very important particularly in surface scan analysis. The uniformity can be studied using electron, pion or muon beams. The response, total signal in the EM + HAD1 section, is plotted as a function of the x position for different y positions to study the uniformity with 100 GeV electrons as shown in figure 3.16.a. And this plot is repeated for 80 GeV pions in figure 3.16.b.

The signal distributions show non-uniformity for the EM sections whereas they are uniform for the HAD sections.

3.3.3. Energy Resolution and Linearity

When an energetic enough particle hits the calorimeters, it loses its energy in the calorimeter, so we can measure a signal in the active material of the calorimeter proportional to the energy of the hitting particles.

If the calorimeter is able to absorb the radiation completely, this information can be used to calculate the amount of energy deposition. This information may be saved as the signal is generated.

In an ideal calorimeter, the expectation is that the relationship between the coming particle energy and generated signal to be linear.

Many of the calorimeters are linear or nearly linear for one type of particle but not for all types of particles. Therefore, a calorimeter can have a different output for different particle types.

In order to study energy linearity and resolution, we have several criteria such as requiring single hits, rejecting unwanted particles (muon, hadron or electron) which contaminate the beam and taking into account the non-uniformity conditions if non-uniformity is present. More detailed information about cuts can be found in chapter 3.2.2.1 and 3.2.2.2.

3.3.3.1. Energy Resolution and Linearity with Pions

In order to study the linearity and the relative energy resolution of the CASTOR prototype response as a function of energy, pion beams which focused on the semi octant of the Saleve side with, 20, 30, 50, 80, 100, 120, 150, 300 GeV energy were used. In addition to the criteria, defined in section 3.2.2.2, a three mm radius cut was applied around the beam center and the events, hitting within the radius cut, were collected. For this cut, WCC information was used. The profile of the beam can be seen in figure 3.17.

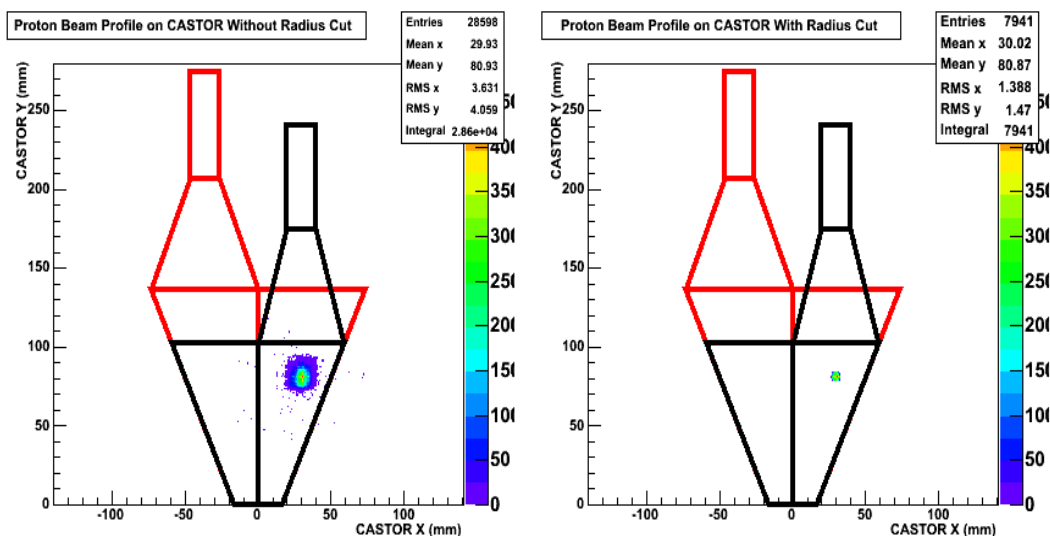


Figure 3.17. Three mm radius cut was applied around the run center, WCC information was used, the left plot doesn't have radius cuts and the right one has radius cut for the same pion run.

The left plot doesn't have radius cut and the right one have radius cut for the same run. For pion runs, full length (14 RUs) was used. Not only Saleve side response but also Jura side response were added per event. With this method, all events which belong to each run were collected and plotted in figure 3.18. At the end the amplitude and width of the signals were picked up and relative resolution and the linearity were calculated.

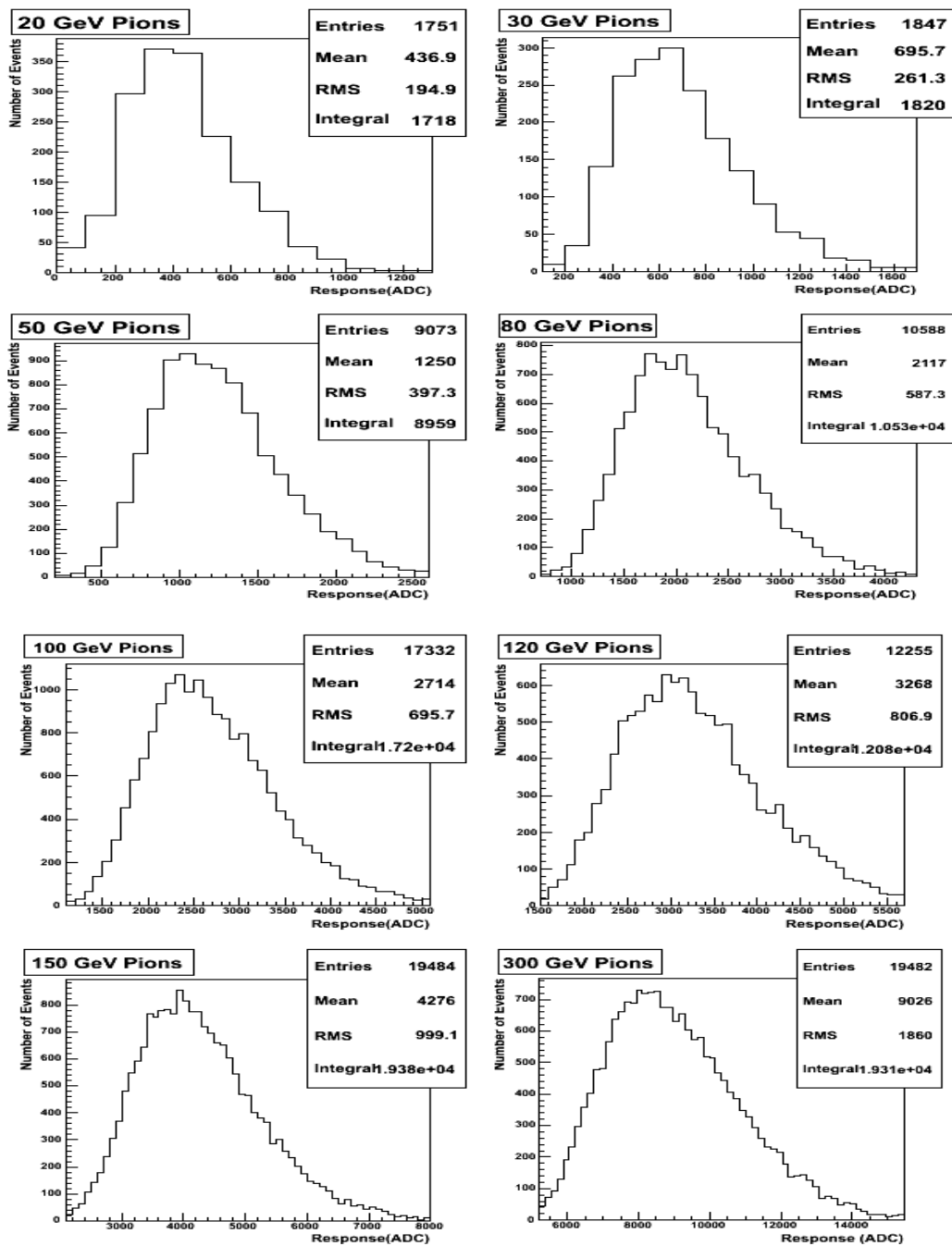


Figure 3.18. For pion runs (20, 30, 50, 80, 100, 120, 150, 300 GeV), full length (14 RUs) Saleve+Jura side response was used.

The relative energy resolution of the calorimeter has been studied by plotting, σ/E , normalized with respect to the incident pion beam energy, E and fitting the functional form shown below. The result is given in figure 3.19:

$$\frac{\sigma}{E} = p_0 + \frac{p_1}{\sqrt{E}} \quad (3.2)$$

The constant term p_0 , coming from the gain variation with changing voltage and temperature, limits the resolution at high energies.

The dominant stochastic term with p_1 is due to intrinsic shower photon statistics.

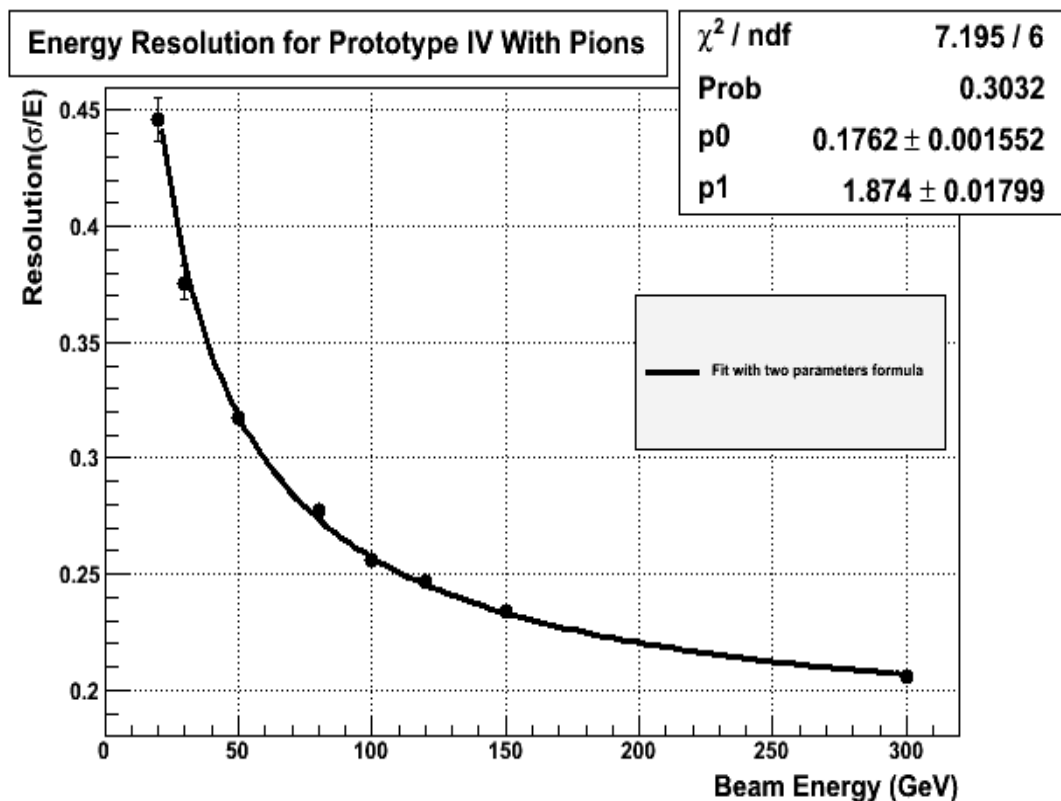


Figure 3.19. The relative energy resolution of the prototype, σ / E , with respect to the incident beam pion energy E .

According to this two parameters fit formula, energy resolution results are pretty good. Stochastic (p_1) term which characterizes the energy resolution is found to be around 187% for two parameters fit formulas for hadron (pions) beams.

The calorimeter response is found to be linear in the energy range explored. The average signal amplitude, expressed in units of ADC channels, can be satisfactorily fitted by the following formula:

$$\text{ADC} = p_0 + p_1 \times E \quad (3.3)$$

where the energy E is in GeV. The fitted values of the parameters for each configuration are shown in figure 3.20 a and b.

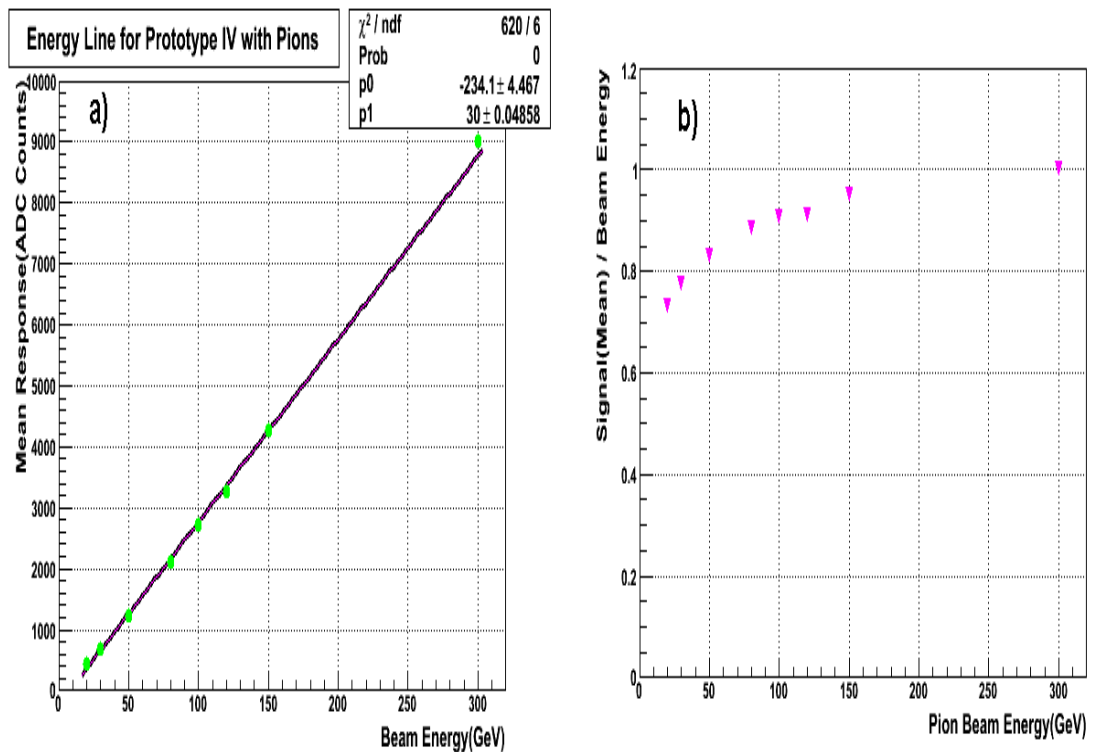


Figure 3.20. a) The signals as a function of incident beam energy b) normalized signal as a function of incident beam energy.

The full calorimeter (14 RU) shows a good energy linearity for pion showers.

3.3.3.2. Energy Resolution and Linearity with Electrons

In order to study the linearity of the prototype response and the relative energy resolution of the prototype response as a function of energy with electrons which were focused on the semi octant of the Saleve side, 10, 20, 50, 120, 150, 180 and 200 GeV

electrons were used. In addition to the criteria defined in chapter 3.2.2.2, a three mm radius cut was applied around the beam center and the events which hit within the radius cut were collected. For this cut, WCE information was used. The profile of the beam can be seen in figure 3.21. The run without radius cut on left side profile and with radius cut on right hand side profile. For electron runs, three RUs (sum of EM and HAD1) were used. With this method, all events which belong to each run were collected and plotted in figure 3.22.

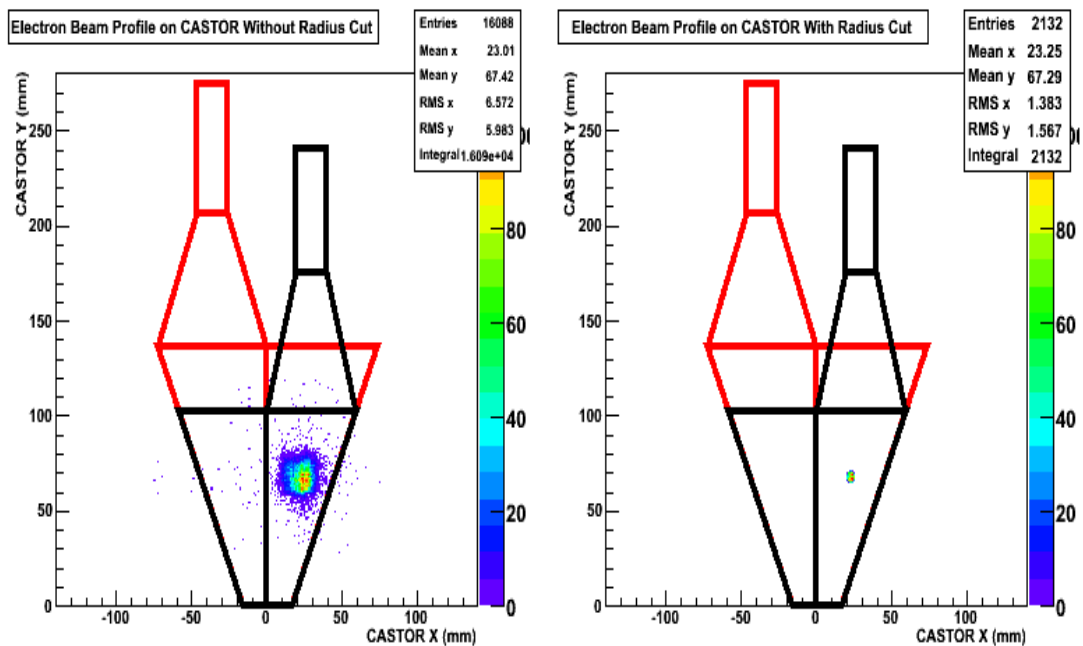


Figure 3.21. Three mm radius cut was applied around the run center, WCE information was used, the left plot doesn't have the radius cuts and the right one has the radius cuts for electron runs.

A Gaussian fit function was applied. At the end, amplitudes and width of the signals were picked up. The amplitude values were multiplied by non-uniform coefficients because of the non-uniformity of the EM section. For this purpose, 100 GeV electrons were used for x -surface scan. First of all, the center (xy) of the runs (10, 20, 50, 120, 150, 180 and 200 GeV) were found. Then, this xy information was used in x -surface scan runs and the following coefficients (1.0, 1.00312, 1.00497, 0.94808, 0.93446, 0.92304 and 1.04399) were calculated. And then, relative resolution and the linearity were calculated.

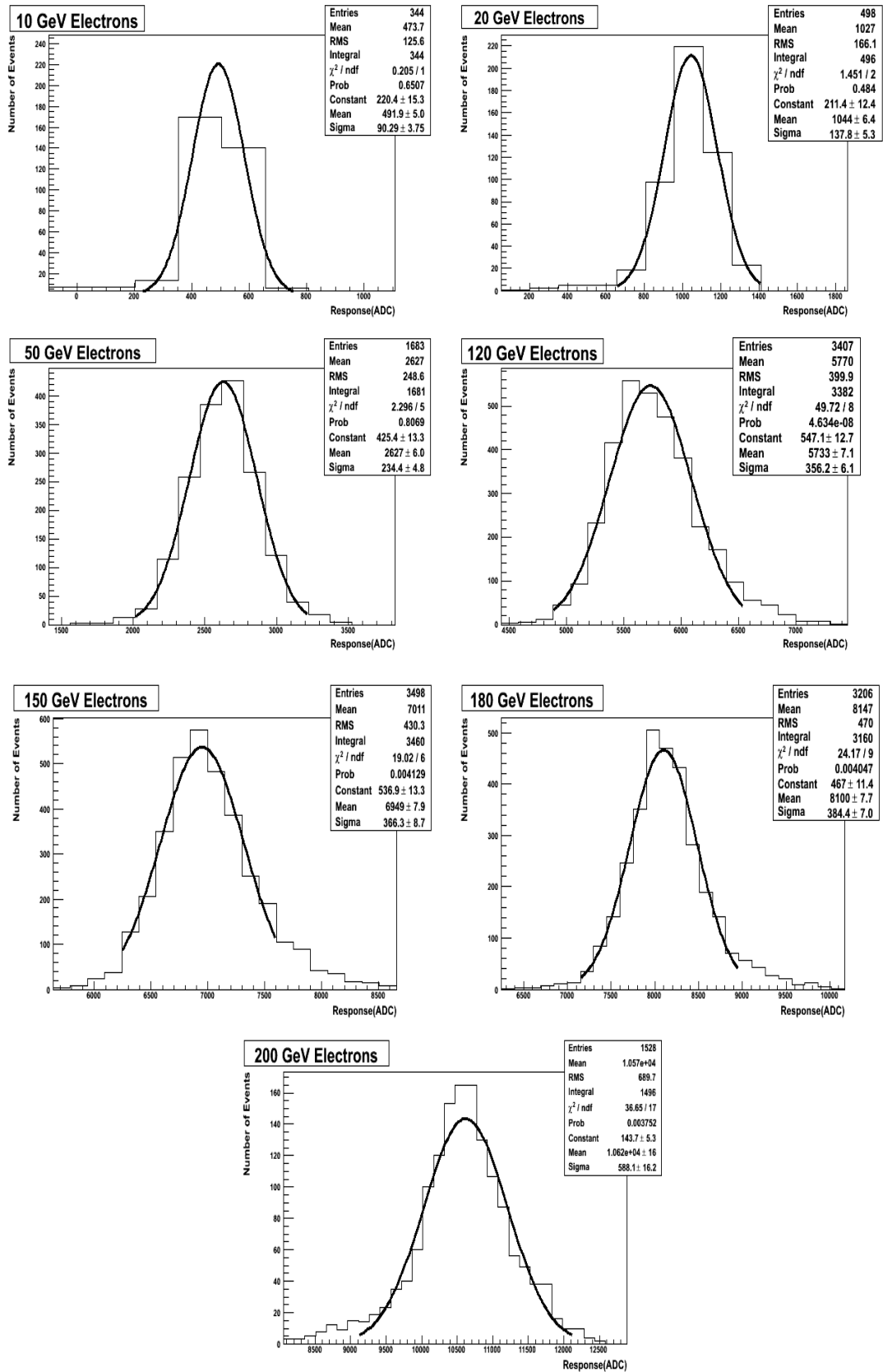


Figure 3.22. For electron runs (10, 20, 50, 120, 150, 180 and 200 GeV), three RUs Saleve side responses were used.

The relative energy resolution of the calorimeter has been studied by plotting the normalized, σ/E , with respect to the incident electron beam energy. It is shown in figure 3.23.

The calorimeter response is found to be linear in the energy range explored. The average signal amplitude, expressed in units of ADC channels, can be seen in figures 3.24.

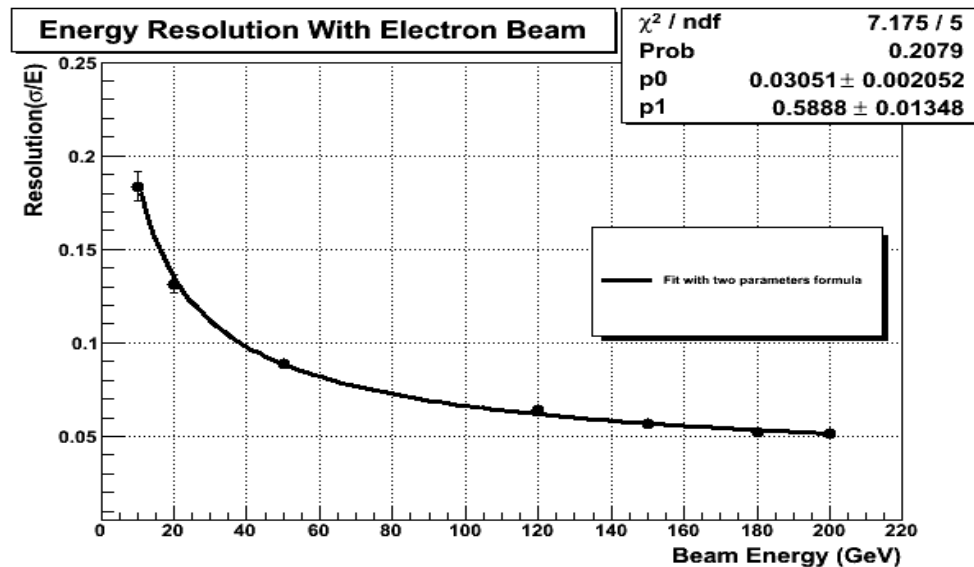


Figure 3.23. The relative energy resolution of the prototype, σ / E , with respect to the incident electron beam energy E .

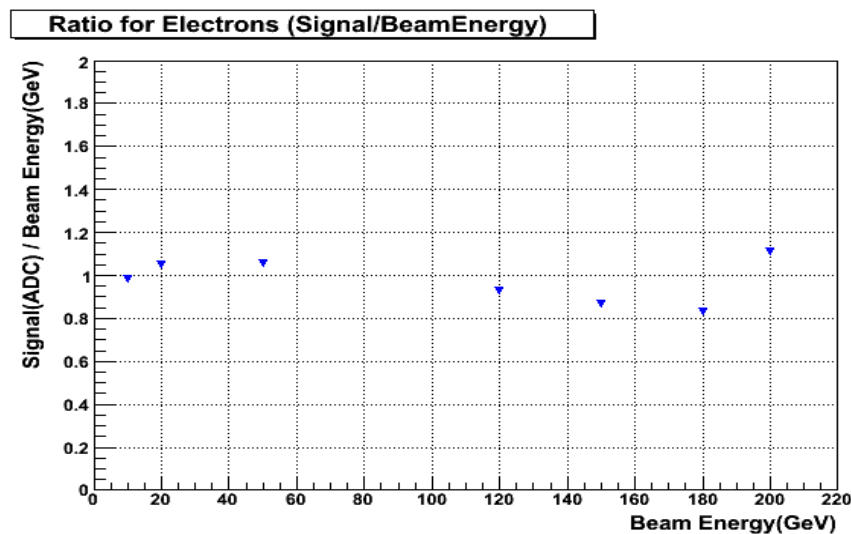


Figure 3.24. The signals (mean)/beam energy as a function of the incident electron beam energy.

The measured stochastic (p_1) term of the resolution is around 58.88% with two parameters fit formula. The result is good enough.

The EM part of the fourth prototype shows a good energy linearity for electron showers.

Table 3.4. Energy resolution parameters for different particle beams.

Type of Particle	p_0	p_1	χ^2/ndf
Pions	0.1762 ± 0.0015	1.874 ± 0.01799	7.195/6
Electrons	0.0305 ± 0.0020	0.5888 ± 0.01348	7.175/5

3.3.4. Transversal and Longitudinal Distribution of the Shower

When an energetic particle hits on the calorimeter, it creates secondary particles and causes showers. If the secondary particles are energetic enough, they create some tertiary particles and so on. Shower develops with the energy of the incoming particles. Both longitudinal and transverse distribution of the shower rise until incoming particles lose all their energies in the calorimeter. Surface scans (position scans) of x and y positions make it possible to acquire information on the transverse distribution for both electron and pion showers.

In order to study the surface scans, we have several criteria such as requiring single hit, rejecting unwanted particles (muon, hadron or electron) which contaminate the beam and taking into account the non-uniformity conditions if the non-uniformity is seen. As it was discussed in section 3.2.2.2, the EM part of the calorimeter is non-uniform so it should be taken into account in the surface scans analysis with electrons. When the full octant (EM+HAD) of the calorimeter is taken into account, it can be seen that the calorimeter is more or less uniform so this will be taken into account for the pion analysis. More detailed information about cuts can be found in chapter 3.2.2.1 and 3.2.2.2.

3.3.4.1. X-Shower Shape with Pions

In order to study the x -shower shape with pions, 80 GeV pions were used, the

pion beam was focused on the prototype face from one end to the other along x direction (Figure 3.25.a). In addition to the standard cuts, defined in chapter 3.2.2.2, position cut was also applied. To define the beam position, WCE information was used. To collect events, rectangle (cell) cut was applied where stable constant $\Delta y = 15$ mm (between 57-72 mm) is used and x is changed from -42.25 mm to $+44$ mm in 1.75 mm steps (Figure 3.25.b). Events per cell for the resulting 50 cells were considered. To find the response of each cell, signals from the full length (14 RUs) just for Saleve side were used. The signal and the x -position of the cell number of 18 can be seen in figure 3.26. The amplitude of the signals as a function of the x -position is plotted in figure 3.27. The points were fitted by a sigmoid curve (step-like) function. Because of the sigmoid shape, it is called **Sigmoid Function** and the function form is $P = 1/(1 + e^{-t})$. As it can be seen from figure 3.27, the fit with sigmoid curve was pretty good. One of the parameters (sigma1) indicates the core of the transverse shower and is found to be 5.395 mm. The other parameter (sigma2) shows the cloud of the transverse shower and is found to be 29.11 mm for the Saleve side semi octant.

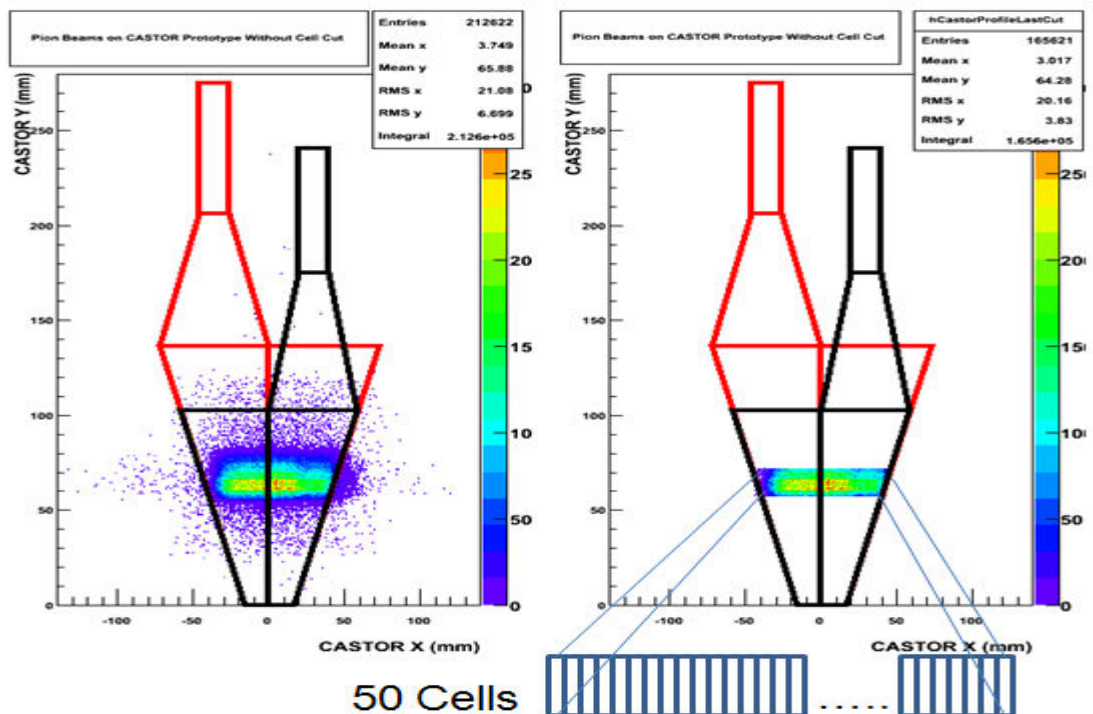


Figure 3.25. a) The pion beams (80 GeV) were focused on the prototype face from end to end in x position b) Applied rectangle (cell) cut where stable constant $\Delta y = 15$ mm (between 57-72 mm) is used and x is changed from -45 mm to $+45$ mm with 1.75 mm steps.

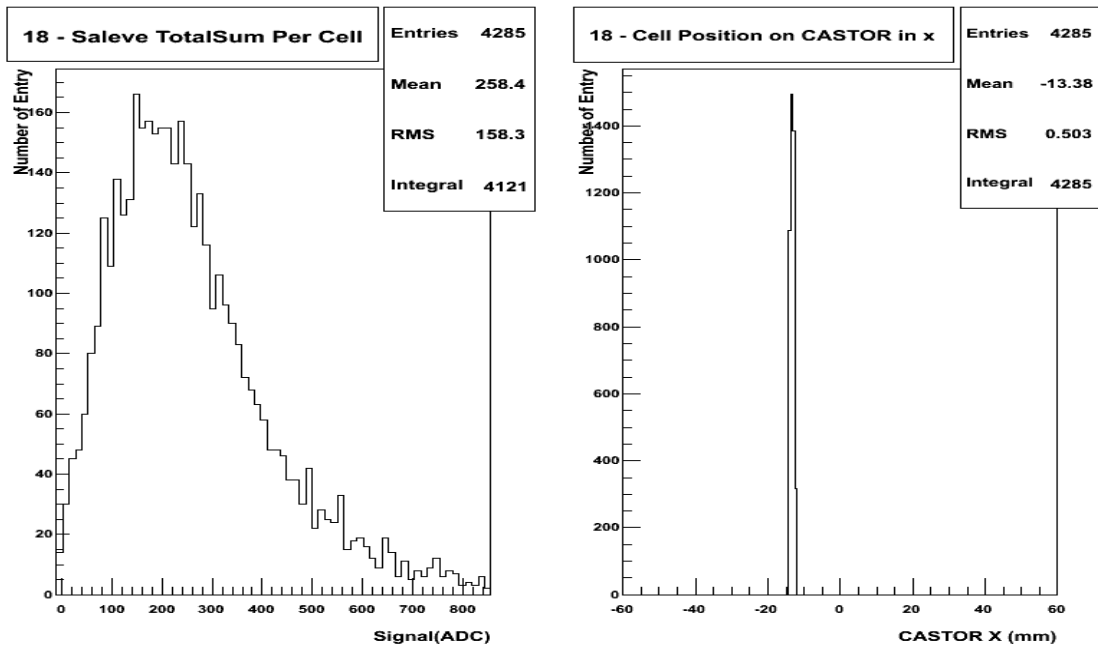


Figure 3.26. These two histograms belongs to the cell number 18, the left one is signal (response) and the right one position histogram.

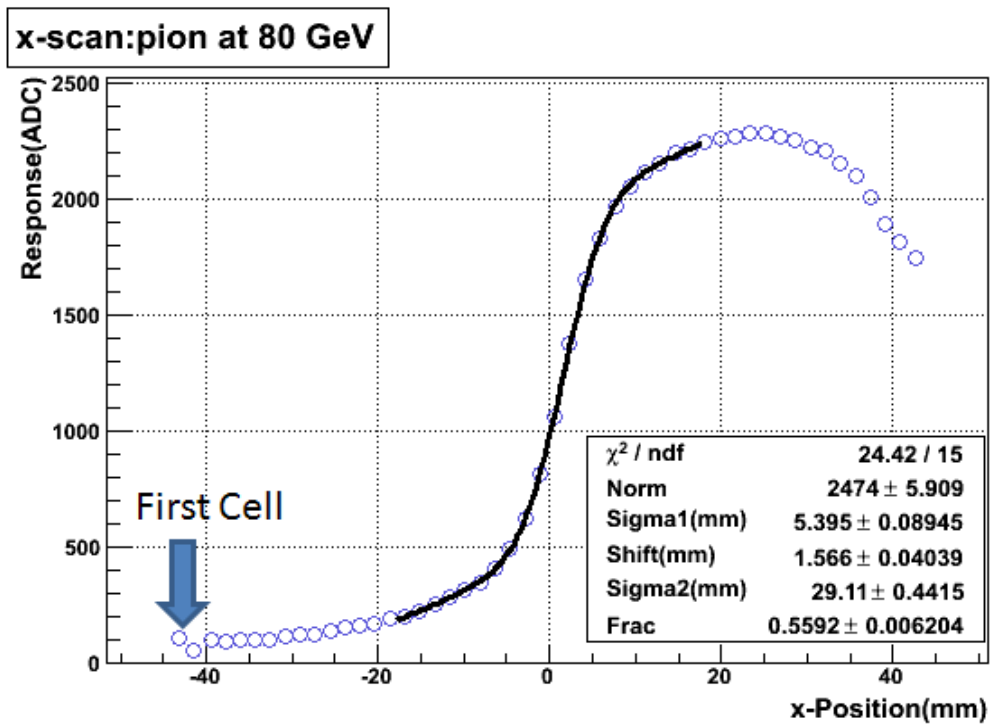


Figure 3.27. The signal mean values as a function of the x-position mean values (for all cells), the points were fitted by sigmoid curve function. The core of the shower is 5.395 mm, and the cloud of the shower is 29.11 mm, for Saleve side semi octant with pions.

3.3.4.2. X-Shower Shape with Electrons

In order to study the x -shower shape with electrons, 100 GeV electrons were used. The electron beam was illuminated on the prototype face from one end to the other along x direction (Figure 3.28.a). In addition to the standard cuts, defined in chapter 3.2.2.2, position cut which is very important for this kind of analysis was also applied. To define the beam position, WCE information was used. To collect events, rectangle (cell) cut was applied where stable constant $\Delta y = 15$ mm (between 57-72mm) is used and x from -42.25 mm to $+44$ mm in 1.75 mm steps (Figure 3.28.b). Events per cell for the resulting 50 cell were considered. To find the response of each cell, signals from the three RUs both for Saleve side and Jura side semi-octants were used. The signal and the x -position of the cell number 18 can be seen in figure 3.29. The amplitude of the signals as a function of the x -position is plotted in figure 3.30.

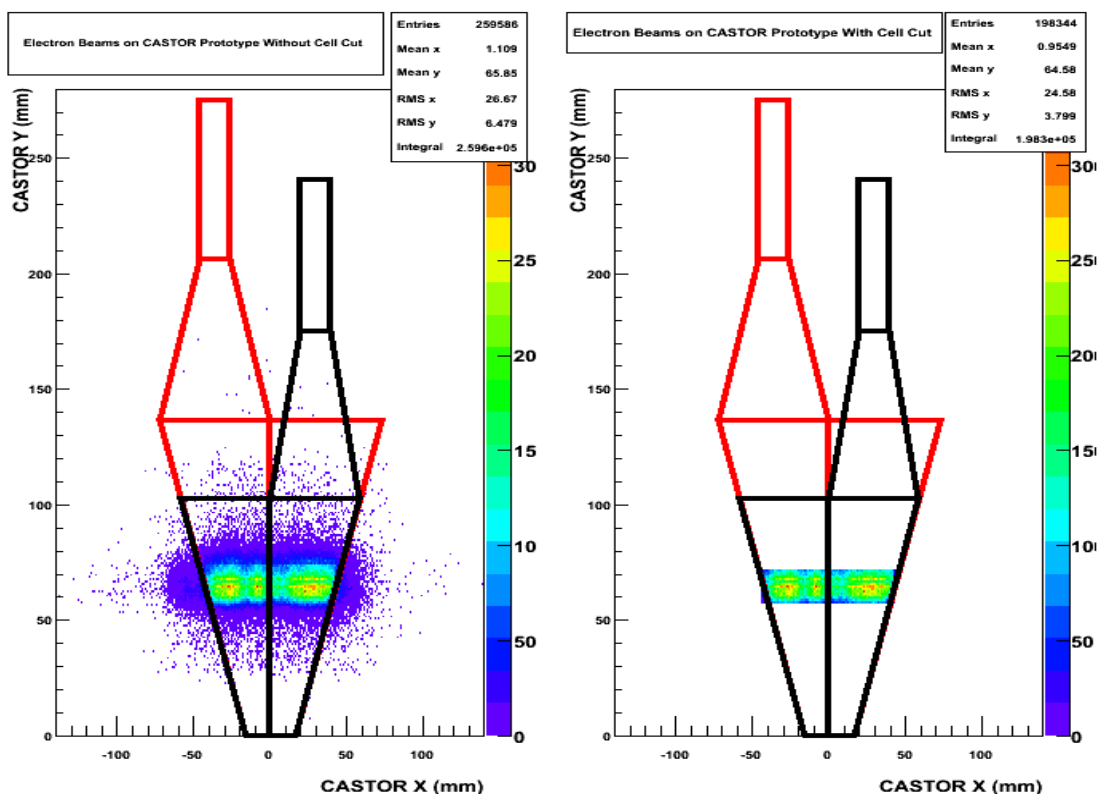


Figure 3.28. a) The electron beams (100 GeV) were focused on the prototype face from one end to the other along x direction b) Applied rectangle (cell) cut where stable constant $\Delta y = 15$ mm (between 57-72 mm) is used and x is changed from -45 mm to $+45$ mm with 1.75 mm steps.

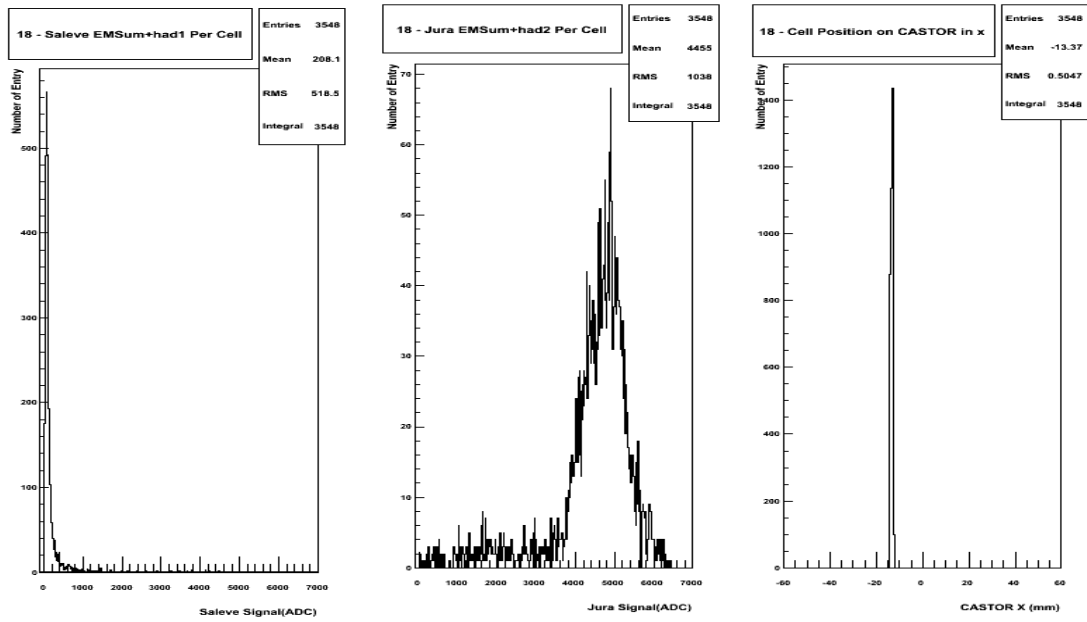


Figure 3.29. The three RUs response of the cell number 18, for both Saleve and Jura side for the electron beams.

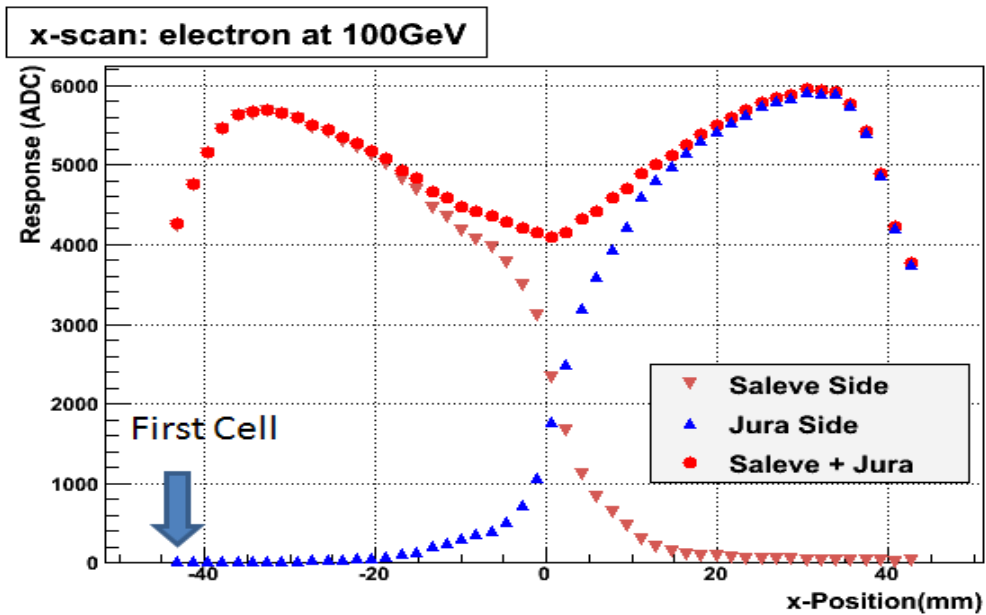


Figure 3.30. Signals mean values as a function of the x -position mean values for Saleve and Jura side semi octant with electron beams.

In order to find the Saleve side x -surface scan with electron beams, derivative method which is $d(\text{Response}) / d(x\text{-Position})$ were used and the derivative points plotted as a function of x -Position and then points were fitted by gauss fit function the

results shown in figure 3.31. According to these results the transverse of the Saleve side to be 1.288 mm measured.

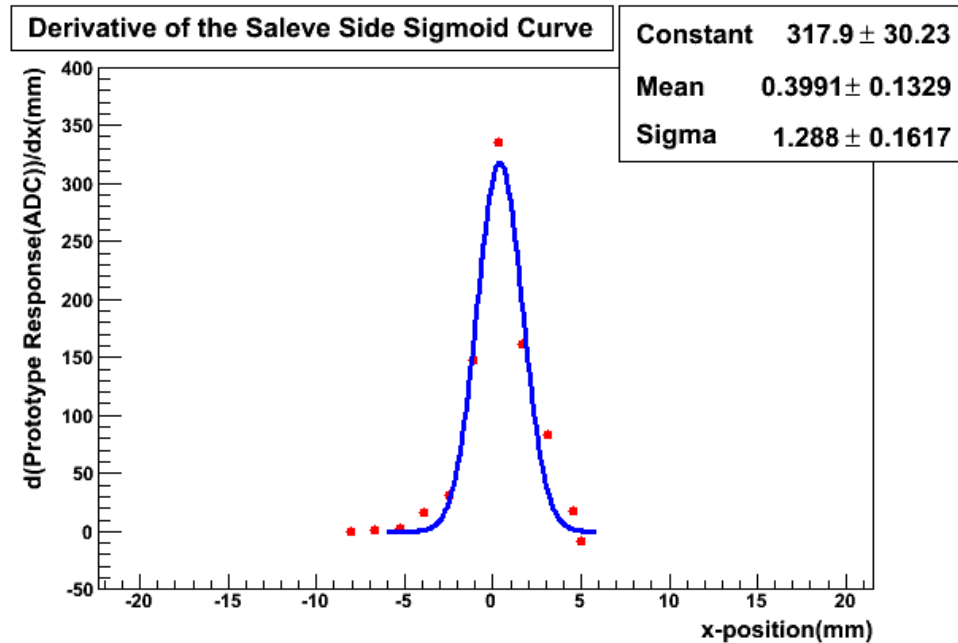


Figure 3.31. The derivative results as a function of the x -position mean values the points were fitted by gauss fit function. The core of the shower is 1.288 mm for Saleve side semi octant with electron beams.

3.3.4.3. Y-Shower Shape with Electrons

In order to study the y -shower shape with electrons, 80 GeV electrons were used. The electron beam was incident on the prototype face from around the beginning of the bottom side to the top side along y direction (figure 3.32 a). In addition to the standard cuts, defined in chapter 3.2.2.2, position cut was also applied. To define the beam position, WCC information was used. To collect events, rectangle (cell) cut was applied where stable constant $\Delta x = 6$ mm is used and y is changed from ~ 12 mm to 132 mm in 2.45 mm steps (Figure 3.32 b). Events per cell for the resulting 50 cells were considered. To find the response of each cell, signals from the three RUs both for Saleve and Jura side semi-octants were used. The signal and the y -position of the cell number 18 can be seen in figure 3.33. The signal mean values as a function of the y -position mean values were plotted in figure 3.34.

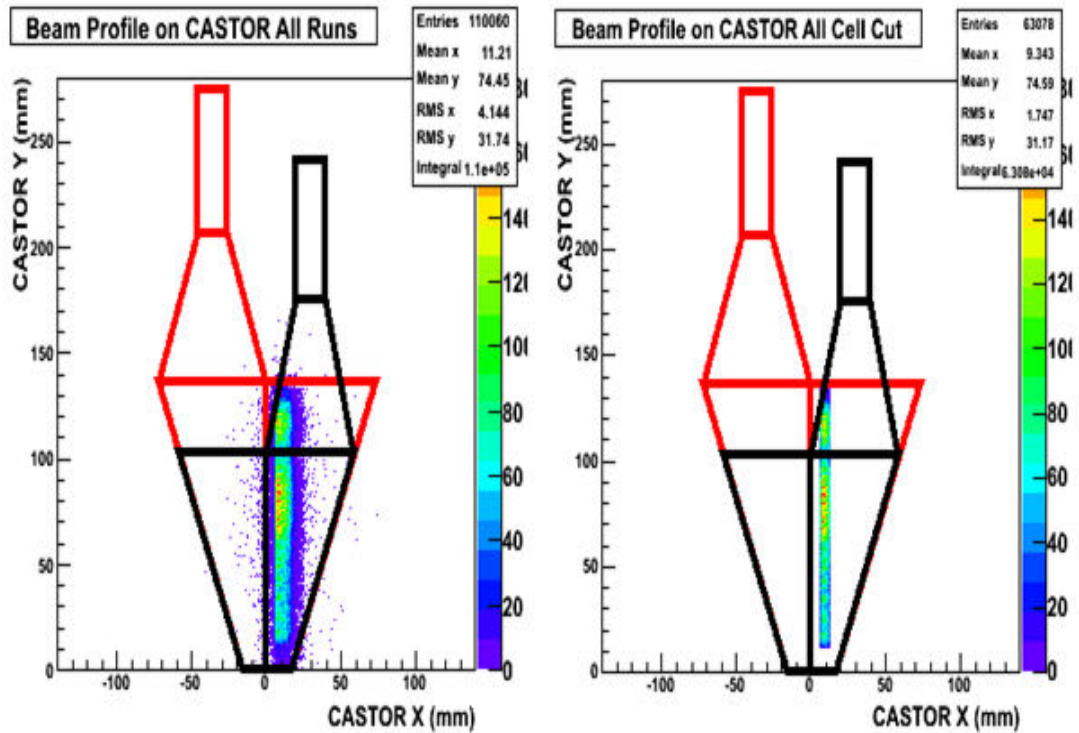


Figure 3.32. a) The electron beams (80 GeV) were focused on the prototype face from the beginning of the bottom side to the top side along y direction b) Applied rectangle (cell) cut where stable constant $\Delta x = 6$ mm and y is change from ~ 12 mm to 132 mm with 2.45 mm steps.

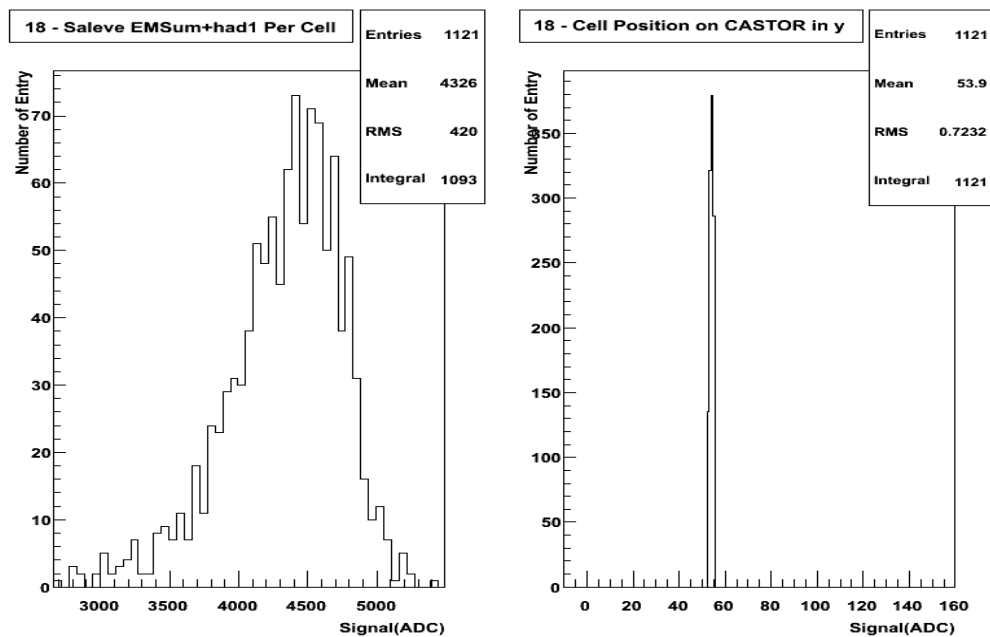


Figure 3.33. The three RUs response of the cell number 18 for Saleve side were used with electron beams.

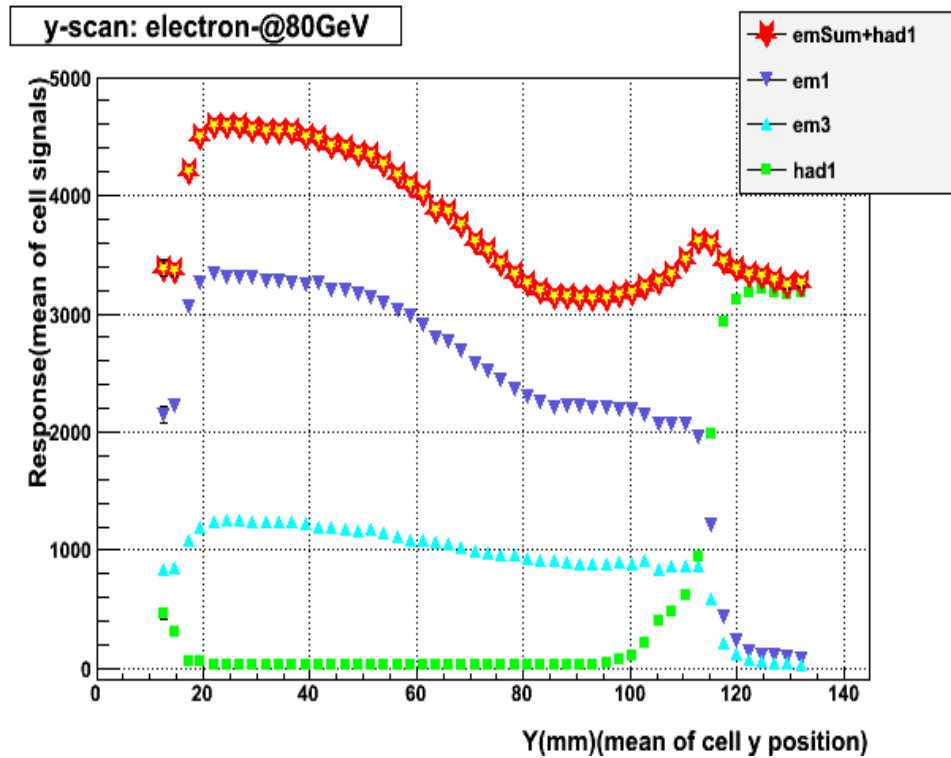


Figure 3.34. Signal mean values as a function of the y-position mean values for Saleve side semi octant with electron beams.

3.3.4.4. Longitudinal Distribution

CASTOR is a sampling calorimeter consisting of segmented active material and absorber material. Energetic particles create electromagnetic and hadronic showers, developing in both longitudinal and transversal directions. When a particle hits on the calorimeter, a response can be read from each of the RUs. If the response value is larger than the pedestal response value, it means that there is a particle from the shower in the active material. So we can read out the signal along lengthwise channels. The last channel signal value which is larger than the pedestal value tells us that the last particle is in this channel. With this information, the longitudinal distribution of the showers can be measured.

In order to study the longitudinal distribution, different particles were used with various energies. The beam was focused on the prototype (figure 3.35). With standard cuts, defined in chapter 3.2.2.2 beam was cleaned. Several criteria were applied such as requiring single hit, rejecting unwanted particles (muon, hadron or electron) which contaminate the beam.

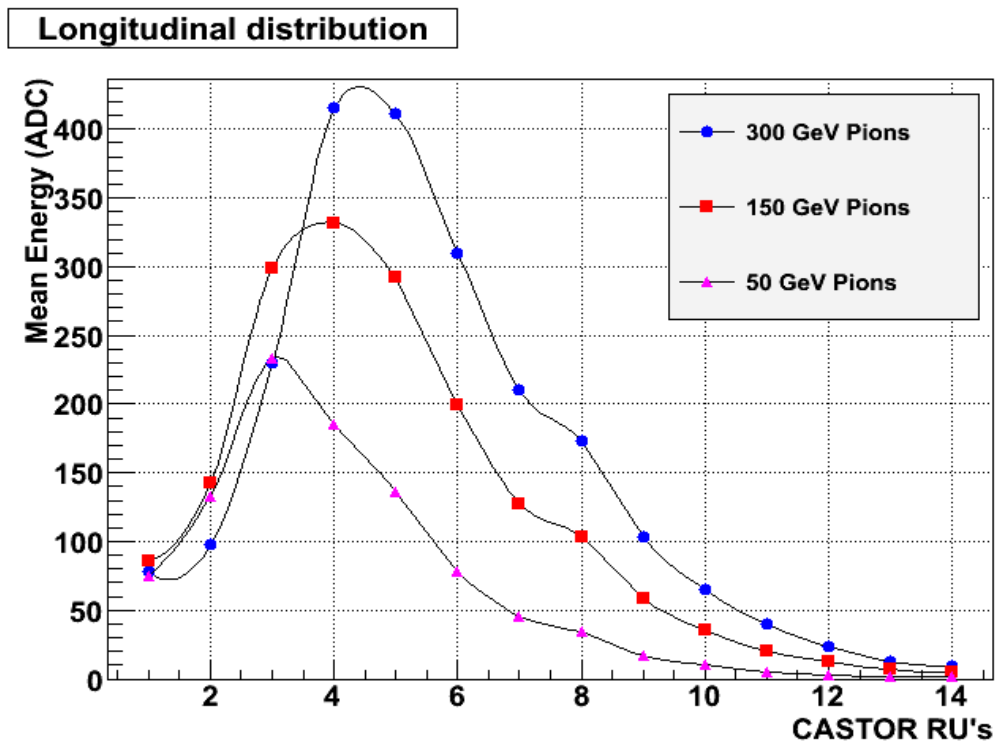


Figure 3.35. Longitudinal distribution of the response, along the depth of the CASTOR prototype.

4. INSTALLATION AND FIRST DATA FROM CASTOR IN CMS

In this chapter the installation of CASTOR calorimeter in HF platform in $-z$ direction of the CMS and very preliminary data analysis, taken with different magnetic fields, will be described.

4.1. Installation of CASTOR in CMS

As explained in previous chapters, CASTOR is located on the castor table which is in HF platform in $-z$ direction (minus z of CMS). CASTOR calorimeter which consists of two halves, both of which are fully equipped with Q/W plates, light guides, PMTs and cabling except sector 9 and 10 led fibers, was installed on the castor table at the end of June 2009. Figure 4.1 shows the two halves of CASTOR, the castor table, HF platform and beam pipe in $-z$ side. For the moment CASTOR is just placed in $-z$ direction of the CMS. After CASTOR was put on the table, the HF platform was moved to the beam line level. Then pedestal data, having high noise, was taken. In order to keep the CASTOR detector lightless, it was covered by a special sheath (Figure 4.2). Then, the pedestal data was taken and results showed that the sheath was good enough to keep the light out. The first LED run 102428 was taken.

Then CASTOR was closed and positioned next to the beam pipe in an asymmetric way. The closest distance of the rear end of the CASTOR is 7 mm away from the beam pipe. The bottom distance was smaller than the top.

On 09 July 2009 the CASTOR area was closed with the collar and rotating shielding without shims and cheese wedges. The distance between CASTOR ribs and inner surface of the rotating shielding is different for the far and near sides. On the far side, it was measured to be 35 - 40 mm and on the near side, it was greater than 70 mm.

After the collar and rotating shielding were closed, magnet was ramped up (Figure 4.3). Then, data was taken (pedestal, LED) at 0, 0.5, 1.0, 1.5 T in different HV and LED intensity settings. There was a problem in $+z$ side of the CMS. It took approximately two weeks to fix the problem. The next magnet ramping up was started in 24.07.2009. At that time, there was a problem with CASTOR cooling system, in near side of CASTOR there was water leakage, so near side was not powered up anymore. Then data was taken just from the far side of the CASTOR at 0, 1.0, 1.4, 2.0, 3.0, 3.46

4. INSTALLATION AND FIRST DATA FROM CASTOR IN CMS Bayram TALİ

and 3.8 T. Finally the magnet test was completed successfully.

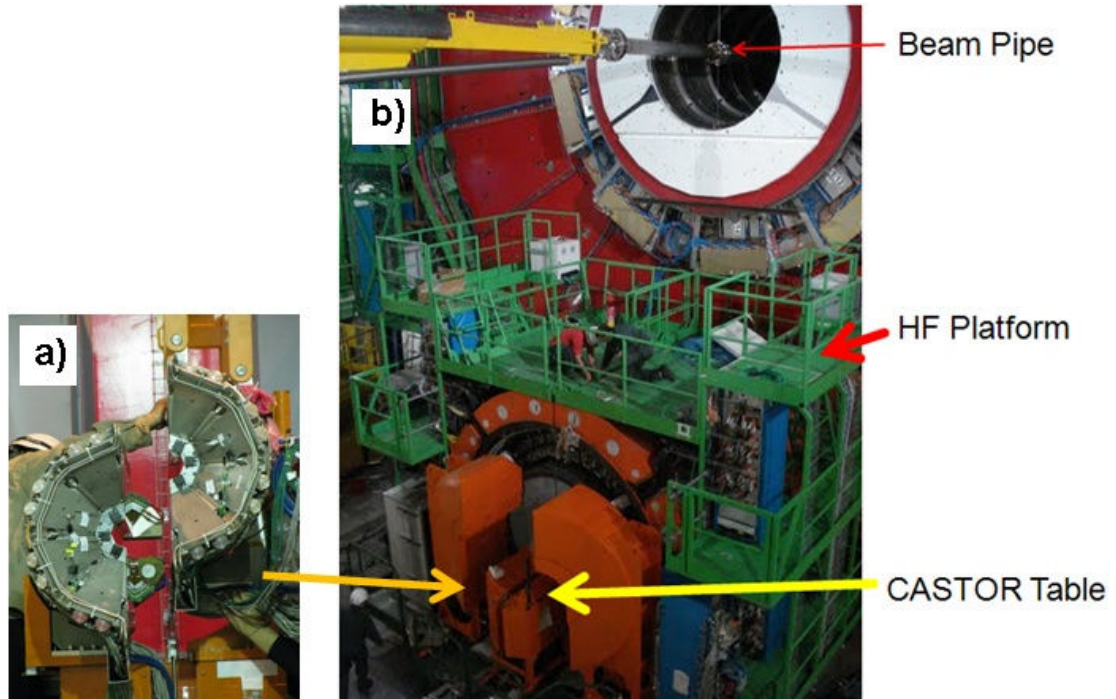


Figure 4.1. a) two halves of the CASTOR calorimeter, b) the castor table, HF platform and the beam pipe in $-z$ direction of the CMS.

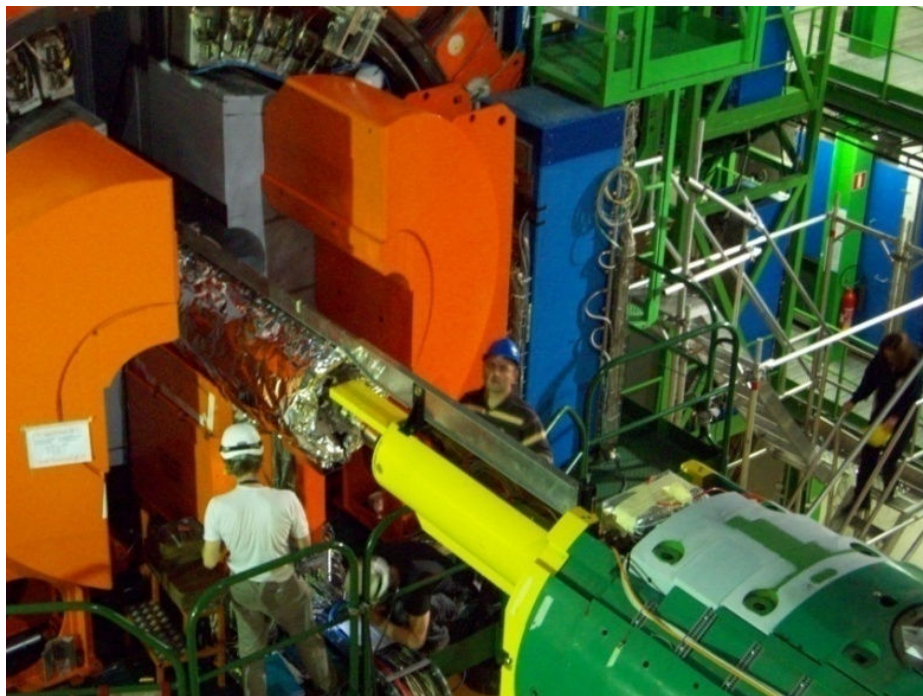


Figure 4.2. The CASTOR calorimeter was moved to the beam line level and it was covered by a special sheath.

4. INSTALLATION AND FIRST DATA FROM CASTOR IN CMS Bayram TALİ

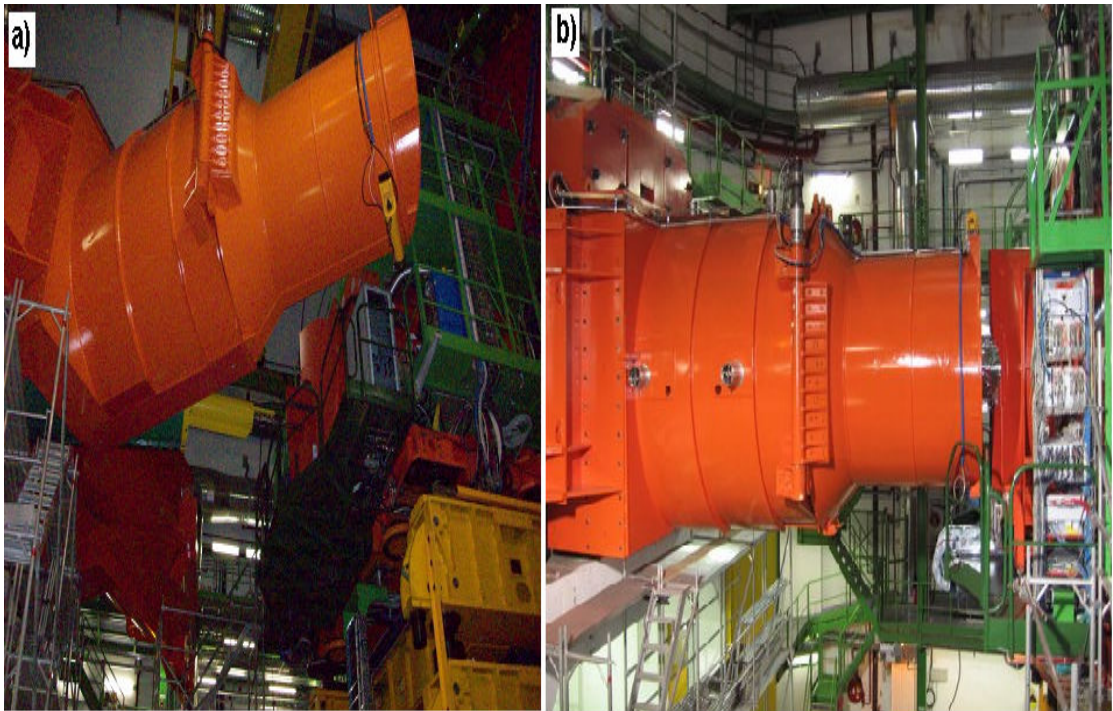


Figure 4.3. a) collar and rotating shielding, b) collar and rotating shielding without shims, and cheese wedges.

In order to measure the magnetic field on the CASTOR area, there were magnetic sensors on the front and middle of the CASTOR ribs. According to the magnetic sensors on the front the magnetic field was measured as 0.051 T and on the middle the magnetic field was measured as 0.214 T when super conducting magnet was providing 3.8 T (Figure 4.4) (Popescu, <http://indico.cern.ch/getFile.py/access?subContId=2&contribId=5&resId=0&materialId=1&confId=67564>).

As there was a magnetic field on the CASTOR area, several parameters were effected. The two most important effects on CASTOR were the PMT signal gains, discussed in chapter 4.2, and the movement of CASTOR. To learn how the castor table and the CASTOR are moving, various sensors were located in different parts of the castor table and CASTOR. The movement information which was taken from the sensors can be seen in table 4.1 and figure 4.5. According to this information, it is clear that the movement was in several directions and had different amplitudes. The movement sensor results showed that all the movements were below the required limits. So, CASTOR will be integrated into HCAL.

4. INSTALLATION AND FIRST DATA FROM CASTOR IN CMS Bayram TALİ

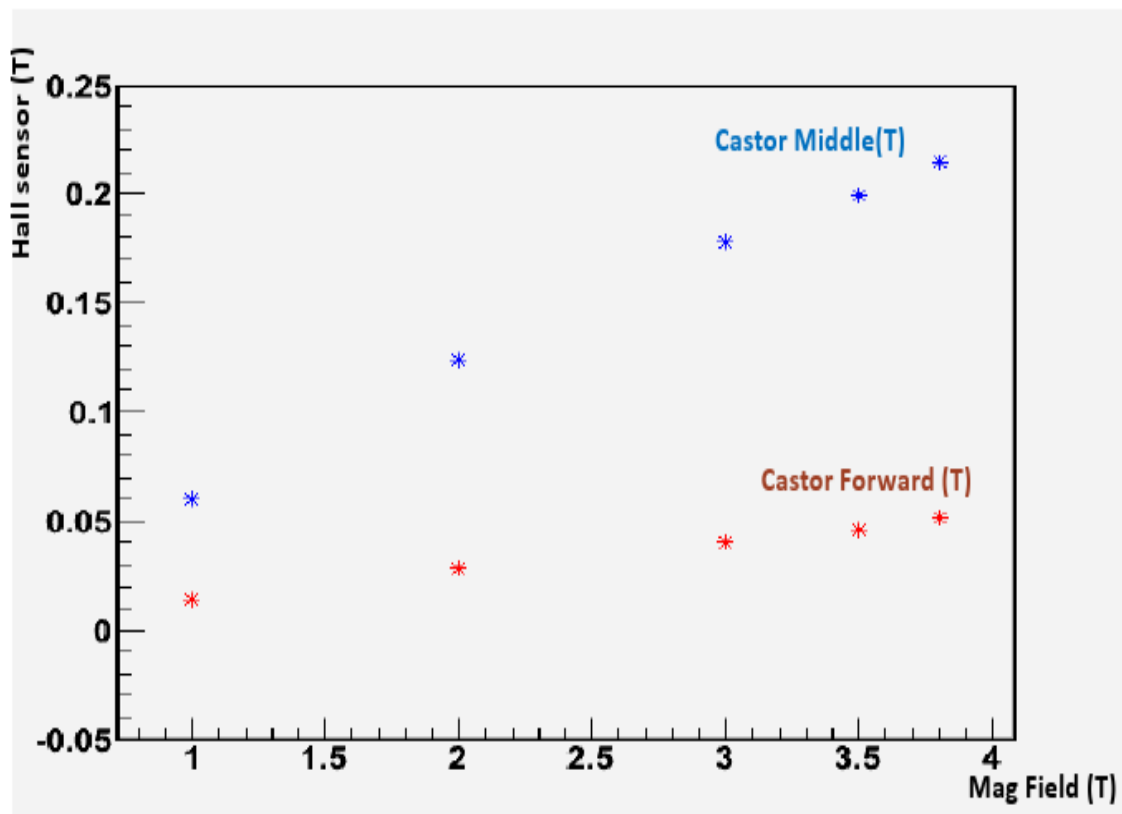


Figure 4.4. Hall sensors on the middle and the front of the CASTOR ribs and the magnetic field at the CASTOR area (<http://indico.cern.ch/getFile.py/access?subContId=2&contribId=5&resId=0&materialId=1&confId=67564>).

Table 4.1. Different parts of the castor table and the CASTOR movement information (https://twiki.cern.ch/twiki/pub/CMS/CastorInstallation2009/Joao_Fastrampdown_03082009.pdf).

Place	Position	28/07/09 at 0T (mm)	28/07/09 at 3.8T (mm)
CASTOR TABLE	IP TOP/FAR	14.16	17.3
CASTOR TABLE	IP BOTTOM/FAR	22.26	25.3
CASTOR TABLE	IP BOTTOM/NEAR	15.96	14.51
CASTOR TABLE	IP TOP/NEAR	9.55	11.28
CASTOR TABLE	NONIP TOP /FAR	18.23	21.04
CASTOR TABLE	NONIP CENTER/FAR	18.88	19.36
CASTOR TABLE	NONIP BOTTOM/FAR	12.53	6.43
CASTOR TABLE	NONIP BOTTOM/NEAR	11.87	9.32
CASTOR TABLE	NONIP CENTER/NEAR	18.8	21.37
CASTOR TABLE	NONIP TOP /NEAR	16.27	19.16
CASTOR	C/RS TOP/NEAR	100.79	100.76
CASTOR	C/RS CENTER/FAR	49.69	51.67
CASTOR	C/RS BOTTOM/FAR	25.91	29.76
CASTOR	C/RS TOP/FAR	41.41	37.85
CASTOR	C/RS BOTTOM/NEAR	45.12	47.28
CASTOR	C/RS CENTER/NEAR	132.95	132.9

4. INSTALLATION AND FIRST DATA FROM CASTOR IN CMS Bayram TALİ

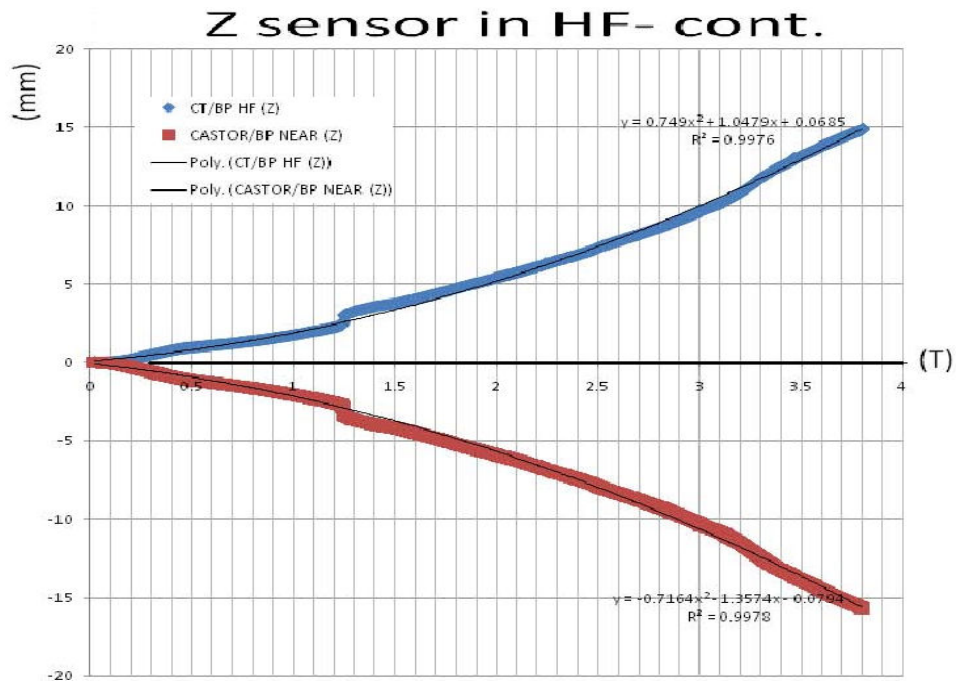


Figure 4.5. Distance sensor measurements before and during magnet ramping up (https://twiki.cern.ch/twiki/pub/CMS/CastorInstallation2009/Joao_magnetrun28072009V1.pdf).

4.2. Preliminary Data Analysis from CASTOR

The CASTOR is divided into two parts with respect to the x axis, $+x$ side is so called NEAR side and $-x$ side is so called FAR side, and it contains 16 sectors azimuthally, the first sector starts on the $+x$ side and the other sectors follow it anti clockwise, and each sector has 14 modules (RUs-channels) (Figure 4.6). Each module (PMT) is powered up by HV and signals are taken from the modules via signal cables which come to the QIE cards. In order to work the QIE cards, they need to be powered up by LV. Fiber optic cables take the signals from QIE cards to the FED (DAQ electronics). All these systems can be controlled by the CASTOR network system. Finally, the data can be taken from the CASTOR in different magnetic fields (0, 1, 1.5, 2, 2.5, 3, 3.5 and 3.8 T). From the data, each sector and every module signals can be checked whether channels are working properly or not working in different magnetic fields. In figure 4.7, it can be seen that at 0 T all channels are powered up but several of them have no signals but at 3.8 T only far side is powered up (because of cooling problems) and in several channels, signals are faint. In several channels, that are in the gap (no cheese wedges and shims), there are no signals.

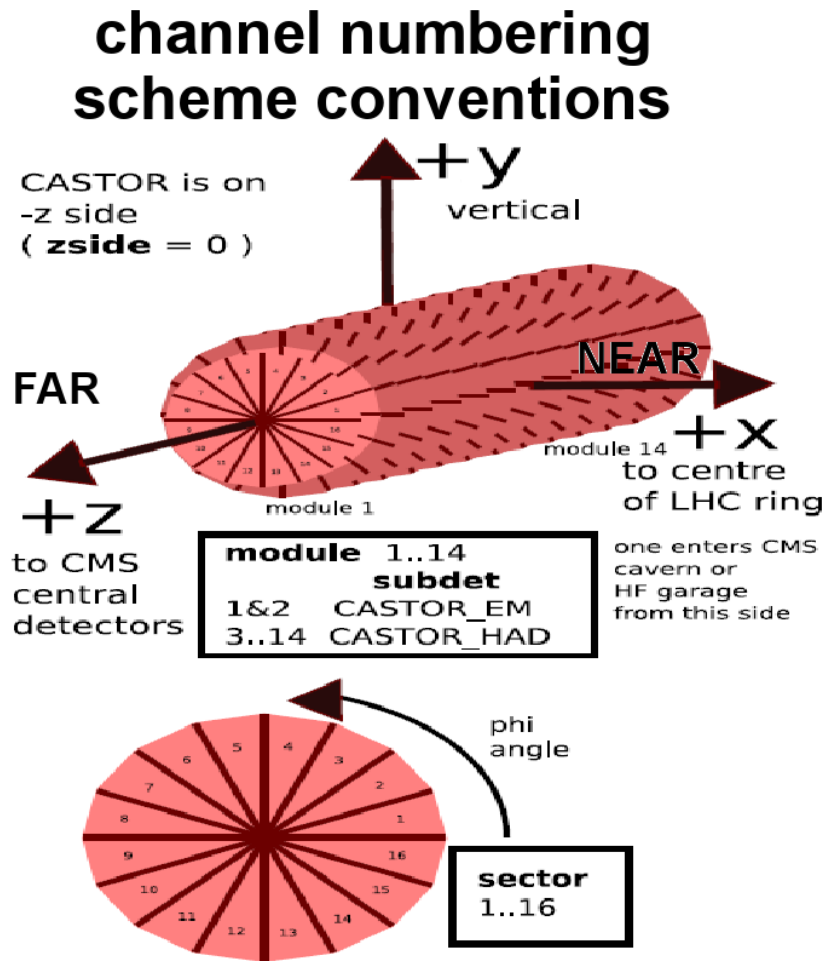


Figure 4.6. Schematic view of sectors and modules of the CASTOR (https://twiki.cern.ch/twiki/pub/CMS/CASTOR/castor_geometrical_numbering.pdf).

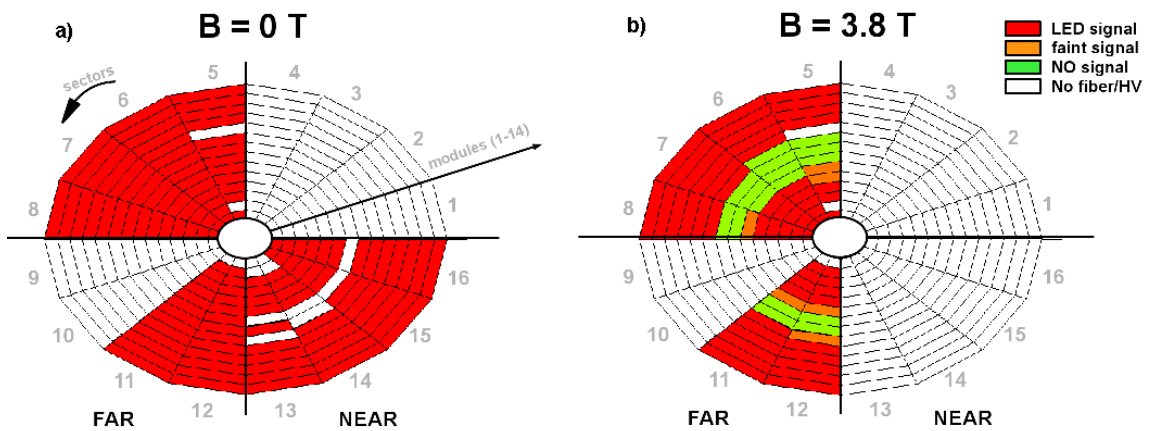


Figure 4.7. a) at 0 T all channels are powered up but several of them have no signals, b) at 3.8 T only far side is powered up in several channels, signals are faint and in various channels, which is in gap, there are no signals (http://users.uoa.gr/~pkatsas/PMTmagnetTest_040809.pdf).

4. INSTALLATION AND FIRST DATA FROM CASTOR IN CMS Bayram TALİ

Also from the data, the gain of the signals from each sector and every module can be checked for different magnetic fields or HVs. In figure 4.8, two signals can be seen; one used as reference and the other one used as signal. So, gains can be calculated (Figure 4.9). The signal gain values were found to be much below the previous values measured at the laboratory. Further study is needed to understand the reason for this.

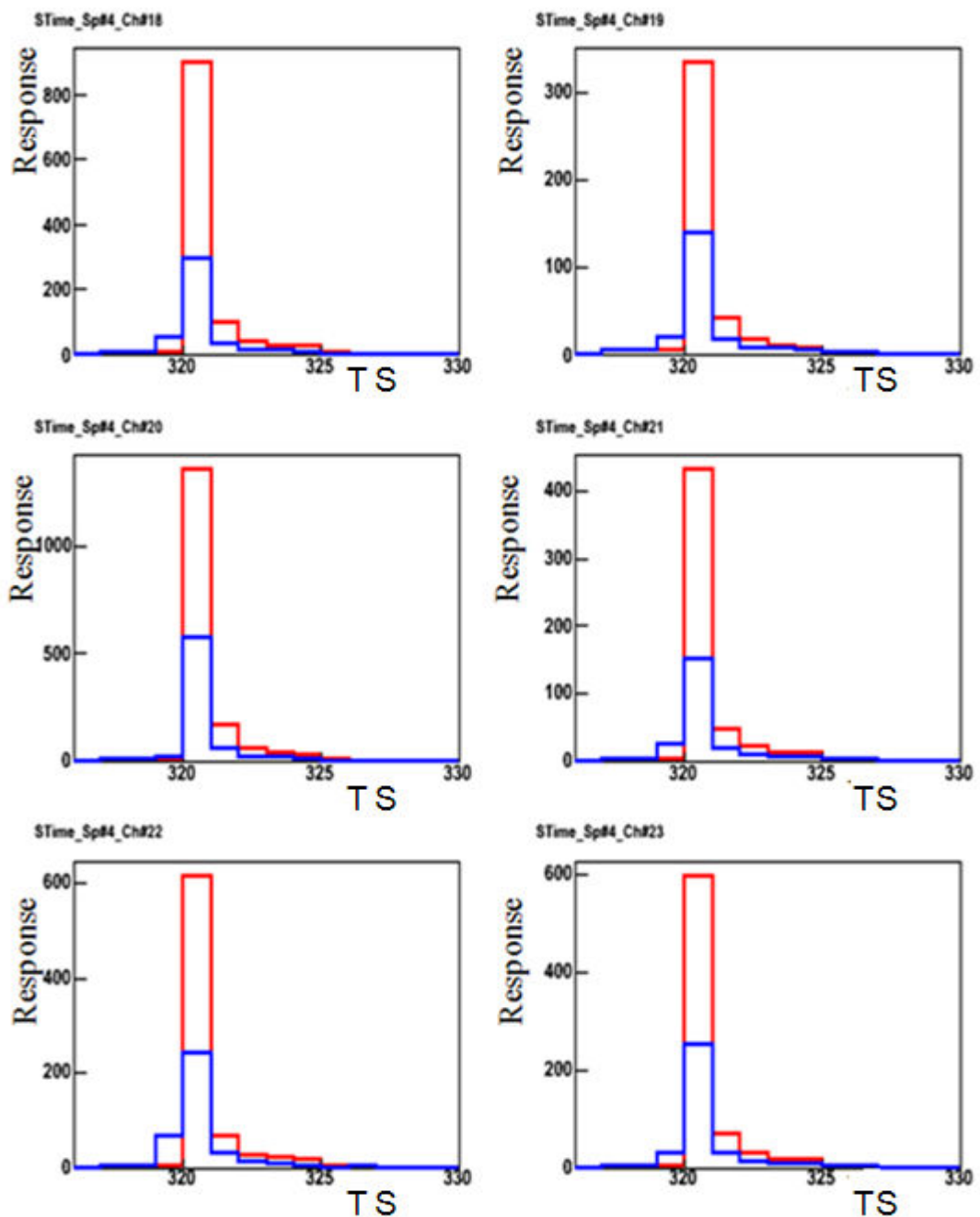


Figure 4.8. Two signals, one used as reference and the other one used as a gain signal.

4. INSTALLATION AND FIRST DATA FROM CASTOR IN CMS Bayram TALİ

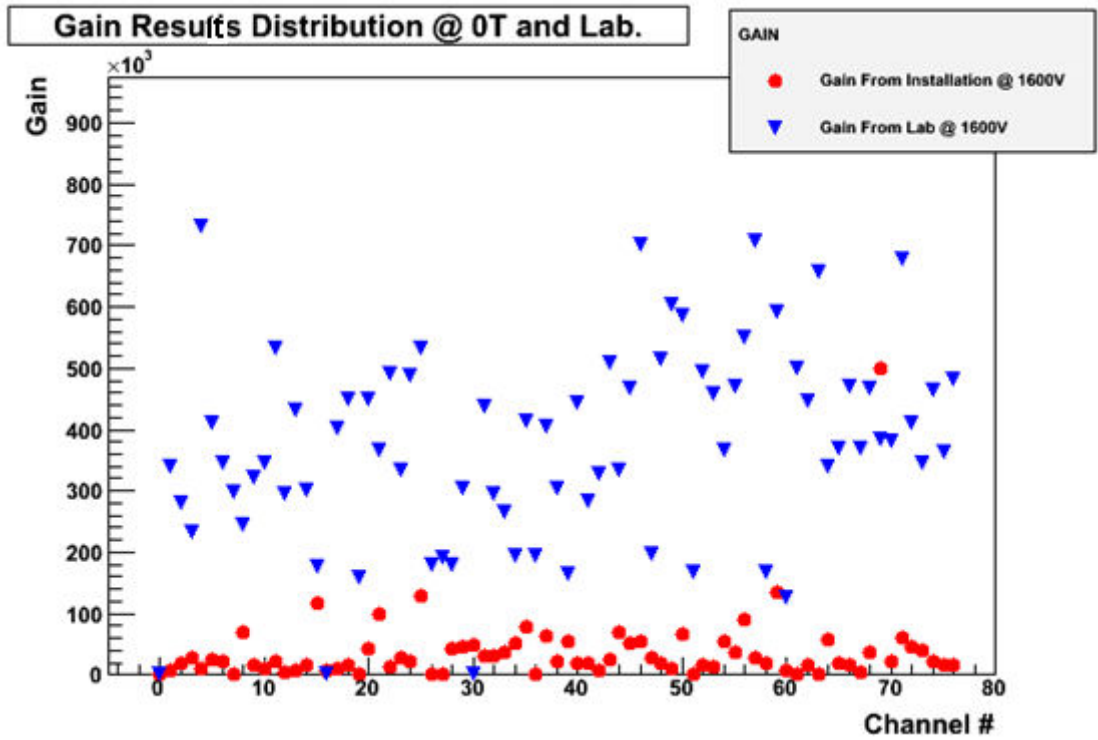


Figure 4.9. The triangle points show the gains of the PMTs which were measured in laboratory, the full points show the gain for the same PMT from the installation.

5. CONCLUSION

In this chapter the PMT gain and timing test processes results, CASTOR TB08 data analysis results and CASTOR installation will be discussed.

The PMT measurement methods at Çukurova University test station consist of some tests which are necessary to check the results of the manufacturer. The purpose of these tests was to determine whether the PMTs suggested by the manufacturer were to satisfy the operational requirements listed in table 2.1 or not.

The tests were performed on two groups of Hamamatsu R7378A PMTs: First group were 75 PMTs. The first step was to check all PMTs physically whether there were any scratches on the window, any breaks anywhere of the PMT and any problems on the pins. The next step was to measure the anode dark current, anode current, cathode current, gain, linearity, collection efficiency, rise time, pulse width and transit time.

There were 50 PMTs in the second group: When PMTs were checked physically, the edge of one of the PMTs was broken so we eliminated it and the other 49 PMTs' were found to be suitable enough for the tests. Then, we measured the anode dark current, anode current, cathode current, gain, linearity, collection efficiency, rise time, pulse width and transit time. The results given as the average values at 1 kV can be seen in table 5.1.

Table 5.1. Measurement results, average values at 1 kV.

Parameter	Value	Unit
Anode dark current	1.23×10^{-9}	A
Anode current	1.27×10^{-5}	A
Cathode current	64.89×10^{-9}	A
Gain	1.949×10^6	
Rise time	2.48	ns
Pulse width	6.008	ns
Transit time	13.72	ns
Detection time	19.728	ns

The highest anode dark current which was measured to be 3.240 nA at 1 kV belongs to the PMT numbered BA0979. All other PMTs have values less than this one. These measurement results were within the required limits.

The highest gain was measured to be 5.28×10^6 at 1 kV and belongs to the PMT numbered BA0918. The lowest gain which was measured to be 4.54×10^5 at 1 kV belongs to PMT numbered BA0900. The average value of the gain at 1 kV was found to be approximately 1.949×10^6 for all the PMTs. The result is very close to the value given by the manufacturer.

The highest detection time which was measured as 22.232 ns at 1 kV belongs to the PMT numbered BA0975. All other PMTs have values less than this. So we can declare that Hamamatsu R7378A type PMTs are suitable for the CASTOR calorimeter.

The last CASTOR prototype performance study used the data which were collected during the test beam of 2008 at the CERN/SPS/H2 beam line.

The H2 beam line is described shortly and the detectors which are in the H2 in front of and in back of the prototype allow us to learn several characteristics of the beam. According to the information of these detectors, several cuts were applied to make clean beams not containing unwanted particles. After the beams were cleaned (pions and electrons), the presented results in this study focus on both the full length (EM+HAD sections) and the first three (sumEM + HAD1) channels of the Saleve and Jura sides of the prototype, and include studies for the energy response, surface scan and longitudinal distributions of the showers.

The prototype is shown to have good energy linearity and energy resolution for both EM and HAD sections.

According to this analysis, HAD section has been found to have good energy linearity and good energy resolution. For studying energy linearity and resolution of HAD section, pion beams (20, 30, 50, 80, 100, 120, 150, 300 GeV) were used and stochastic (p_1) term was found to be around 187%.

And also, x -surface scan (shower shape) study was conducted with 80 GeV pion beams. The core of the shower was found to be 5.395 mm, and the cloud of the shower was found as 29.11 mm for the Saleve side.

According to this analysis, EM section has good energy linearity and good energy resolution. For studying energy linearity and resolution of the EM section,

electron beams (10, 20, 50, 120, 150, 180 and 200 GeV) were used and stochastic (p_1) term was found to be around 58.88%. Energy linearity and resolution for EM section were analyzed.

Also, x -surface scan (shower shape) was studied with 100 GeV electron beams and the transverse (x) of the EM section to be found 1.288 mm for the Saleve side.

Moreover, y surface scans were done. 80 GeV electron beams were used for the y -surface scan study. In this analysis, longitudinal distribution was also studied.

CASTOR detector was installed into HF platform in CMS. In this study, the general information about the installation of the CASTOR detector was given.

The magnitude of the magnetic field around CASTOR area was measured as 0.051 T on the front and 0.214 T on the middle side of the calorimeter at 3.8 T.

The movement sensor results showed that all the movements were below the required limits.

The signal gain values were found to be much below the previous values measured at the laboratory. Further study is needed to understand the reason for this.

REFERENCES

- ABDULLIN, S. et al., 2008, “Design, performance, and calibration of CMS forward calorimeter wedges”, *Eur. Phys. J. C*, 53, 139
- , S. et al., 2008, “The CMS Barrel Calorimeter Response to Particle Beams from 2 to 350 GeV/c”,
- ADLOFF, C. and et al.: 2001, [H1 Collab.], *Phys. Lett. B* 520, 183
- AFFOLDER, T., et al., for the CDF collaboration, 2002, "Charged jet evolution and the underlying event in proton-antiproton collisions at 1.8 TeV", *Phys. Rev. D*, Vol. 65, 09-2002
- AKCHURIN N. and WIGMANS R., 2002, “Review of Scientific Instruments”, Vol74, No6
- AKGUN, U. et al., 2002, “Timing, Gain, and Dark Current Measurements of PMTs from Three Different Manufacturers for HF Calorimeter”, CMS Internal Note: IN 2002/032
- , U. et al., 2002, “Single and Double Pulse Linearity Studies Performed on Candidate PMTs for HF Calorimeter”, CMS Internal Note: IN 2002/030
- , U., 2003, “CMS HF Calorimeter PMTs and Ξ_c^+ Lifetime Measurement, Iowa University”, USA (Ph.D. thesis)
- , U. et al., 2004, “Complete Tests of 2000 Hamamatsu R7525HA Phototubes for the CMS-HF Forward Calorimeter”, CMS Internal Note: IN 2004/019
- , U. et al., 2005, “Complete Tests of 2000 Hamamatsu R7525HA Phototubes for the CMS-HF Forward Calorimeter”, *Nuclear Instruments and Methods in Physics Research A*
- ALICE TDR, 2001, CERN /LHCC 2001-021
- ALTARELLI, G. and Parisi, G.: 1977, *Nucl. Phys. B*126, 298.
- ANGELIS, A.L.S. and PANAGIOTOU, A.D., 1997, “CASTOR: A dedicated detector for the detection of centauros and strangelets at the LHC”, *J. Phys. G: Nucl. Part. Phys.* 23 (1997) 2069–2080.
- , A.L.S. et al, 2003, “Model of Centauro and strangelet production in heavy ion collisions”, arXiv:nucl-th/0301003v1.
- ARNEDO, M. and DIEHL, M., 2005, arXiv:hep-ph/0511047 (2005)
- ASLANOGLU, X. et al., 2006, “First performance studies of a prototype for the

CASTOR forward calorimeter at the CMS experiment”, arXiv:0706.2576v3.

-----, X. et al., 2007b, “Performance studies of prototype II for the CASTOR forward calorimeter at the CMS experiment”, Eur. Phys. J. C 52, 495506.

-----, X. et al., 2008, “Performance studies of the final prototype for the CASTOR forward calorimeter at the CMS experiment”, CMS NOTE-2008/022.

-----, X. et al., 2008, “First performance studies of a prototype for the CASTOR forward calorimeter at the CMS experiment”, Acta Physica Polonica B

ATLAS TDR, 1999, “Volume I”, CERN/LHCC 99-14

AYDIN, S. et al., 2007, “Test Results from Quality Control Measurements of Phototubes for the CMS-CASTOR Calorimeter”, CMS CR 2007/000

BASEGMEZ, S., 2008, “CMS-CASTOR Forward Detector and 2007 Test Beam Data Analysis”, Master Thesis

BORRAS, K., 2007, “Status of Forward Physics Projects at CMS”, Proceeds. DIS’07.

CASTOR EDR, 2007.

CMS TDR, 2006, “Volume I”, CERN/LHCC 2006-001

CMS TDR, 2007, “High Density QCD With Heavy Ion”, CMS TDR 8.2-Add1

CMS Collaboration, 2008, “The CMS experiment at the CERN LHC”, IOP Publishing Ltd and SISSA

DALPHIN, M., 2006, “CERN metallurgical examinations”, Report Geneva

D’ENTERRIA, D., 2007, “CMS Physics Technical Design Report: Addendum on High Density QCD with Heavy Ions”, J. Phys. G: Nucl. Part. Phys. 34, 2307–2455

-----, D., 2008, Forward physics at the LHC: QCD, electroweak & Higgs, QCD- School Les Houches talk, March 25th - Apr. 4th, 2008

DOKSHITZER, Yu.L.: 1977, Sov. Phys. JETP. 73, 1216.

HAMAMATSU PHOTONICS K.K., 1999, “Photomultiplier Tubes, Basics and Applications”, Editorial Committee, Japan

HAMAMATSU PHOTONICS K.K., 2005, “Photomultiplier Tubes and Assemblies For Scintillation Counter and High Energy Physics”, Japan

HAMAMATSU PHOTONICS, 2005, “Photomultiplier Tubes and Assemblies”, Japan

HAMAMATSU PHOTONICS, 2006, “Photomultiplier Tubes Basics and Application Third Edition”, Japan

HALZEN, F. and Martin, A., 1984, “Quarks and Leptons: An Introductory Course in

Modern Particle Physics”

http://particleadventure.org/standard_model.html

http://en.wikipedia.org/wiki/Elementary_particle

<http://lhc-machine-outreach.web.cern.ch/lhc-machine-outreach/>

http://www.lhc-closer.es/pages/det_1.html

http://www.uslhc.us/LHC_Science/Experiments/TOTEM

<http://cmsdoc.cern.ch/cms/castor/html/>

<http://en.wikipedia.org/wiki/Photomultiplier>

<http://elchem.kaist.ac.kr/vt/chem-ed/optics/detector/pmt.htm>

http://en.wikipedia.org/wiki/Super_Proton_Synchrotron

<http://ab-div-atb-ea.web.cern.ch/ab-div-atb-ea/BeamsAndAreas/h2/H2manual.html>

<http://nahandbook.web.cern.ch/nahandbook/default/common/software/Beatch.htm>

<http://sl.web.cern.ch/SL/eagroup/Page-1.html>

https://twiki.cern.ch/twiki/bin/view/ABATBEA/SPSPPrimaryTargets#T2_%20ble

<http://indico.cern.ch/getFile.py/access?subContId=2&contribId=5&resId=0&materialId=1&confId=67564>

https://twiki.cern.ch/twiki/pub/CMS/CastorInstallation2009/Joao_Fastrampdown_03082009.pdf

https://twiki.cern.ch/twiki/pub/CMS/CastorInstallation2009/Joao_magnetrun28072009V1.pdf

https://twiki.cern.ch/twiki/pub/CMS/CASTOR/castor_geometrical_numbering.pdf

http://users.uoa.gr/~pkatsas/PMTmagnetTest_040809.pdf

KURAEV, E.A., Lipatov, L.N. and Fadin, V.S: 1977, Sov. Phys. JETP 45, 199.

PERKINS, D.H. and Wesley, A., 1987, “Introduction to High Energy Physics”

LEO, W.R., 1993, “Techniques for Nuclear and Particle Physics Experiments”, NewYork

LHCb TDR, 2005, CERN /LHCC 2005-019

LIPATOV, L.N.: 1976, Sov. J. Nucl. Phys. 23, 338.

GLADYSZ-DZIADUS, E., 2001, “Are Centauros exotic signals of the QGP?”, arXiv:hep-ph/0111163v1

-----, E., 2006, “CASTOR: Centauro And Strange Object Research Exotic Aspects of Forward Physics”, Acta Physica Polonica B

GRIFFITHS, D. et al.: 1987, “Introduction to Elementary Particles”,

GRIBOV, V.N. and Lipatov, L.N.: 1972, Sov. J. Nucl. Phys. 15, 78.
 -----, 1983, Ryskin, Phys. Rept. 100 (1983) 1;
 GUMUS K.Z., 2008, “Search for New Physics in the CMS”, CERN-THESIS-2008-066
 MUELLER A.H. and NAVALET, H., 1987, Nucl. Phys. B 282 (1987) 727
 NORBECK, E. et al., 2006, “Physics at Very Small Angles with CASTOR at CMS”,
 22nd Winter Workshop on Nuclear Dynamics
 -----, E. et al., 2007, “Exotic Physics at the LHC with CASTOR in CMS”, CMS
 Conference Report
 PHILIPS PHOTONICS, 1994, “Photomultiplier Tubes, Principles and Applications”,
 France
 PHOTONICS, 2007, “Photomultiplier Tubes, Principles and Applications”, France
 SCHMIDT, R., 2006, “The LHC Collider: Status and Outlook to Operation”, CERN,
 Switzerland, Geneva
 TOTEM TDR, 2004, CERN-LHCC-2004-002
 VIRDEE, T.S., 1998, Calorimetry. CMS Collaboration, CERN, Geneva, CMS
 Conference Report, CMS-CR, 1998/026
 YAZGAN, E., 2007, “Search for a Standard Model Higgs Boson in CMS Via Vector
 Bosons Fusion in The $H \rightarrow WW \rightarrow l\nu l\nu$ Channel and Optimization of Energy
 Reconstruction in CMS Using Test Beam 2006 Data”, Ankara (PhD Thesis)

CURRICULUM VITAE

I was born in 1974, in Kiğı. I completed my primary school education in Güzgülü village and secondary school education in Kiğı. After that, I enrolled to Sefa Köy high school in İstanbul. I graduated, with the highest degree, from the Physics Department of Süleyman Demirel University in 1997. I got my MSc degree from the Physics Department of Cukurova University in 2001. I have started my PhD degree at the Physics Department of Cukurova University in 2005.

For my researches I spend one of my year in Greece and some other times in Switzerland.

I have been working as a Primary School Teacher in Education Ministry in Adana since 1998. I am married and don't have child.